

# Airborne Observations Constrain Heterogeneous Nitrogen and Halogen Chemistry on Tropospheric and Stratospheric Biomass Burning Aerosol

Zachary C. J. Decker<sup>1</sup>, Gordon Novak<sup>2</sup>, Kenneth C. Aikin<sup>3</sup>, Patrick Veres<sup>4</sup>, J. Andrew Neuman<sup>5</sup>, Illan Bourgeois<sup>6</sup>, T. Paul Bui<sup>7</sup>, Pedro Campuzano-Jost<sup>8</sup>, Matthew Mitchell Coggon<sup>3</sup>, Doug A. Day<sup>9</sup>, Joshua Paul DiGangi<sup>10</sup>, Glenn S. Diskin<sup>10</sup>, Maximilian Dollner<sup>11</sup>, Ale Franchin<sup>12</sup>, Carley D Fredrickson<sup>13</sup>, Karl Froyd<sup>14</sup>, Georgios I. Gkatzelis<sup>15</sup>, Hongyu Guo<sup>16</sup>, Samuel R Hall<sup>4</sup>, Hannah Selene Halliday<sup>17</sup>, Katherine L Hayden<sup>18</sup>, Christopher D. Holmes<sup>19</sup>, Jose Luis Jimenez<sup>8</sup>, Agnieszka Kupc<sup>11</sup>, Jakob Lindaas<sup>20</sup>, Ann Middlebrook<sup>3</sup>, Richard H Moore<sup>10</sup>, Benjamin A Nault<sup>21</sup>, John B. Nowak<sup>10</sup>, Demetrios Pagonis<sup>14</sup>, Brett B Palm<sup>12</sup>, Felix Piel<sup>22</sup>, Jeff Peischl<sup>3</sup>, Pamela Rickly<sup>23</sup>, Michael Robinson<sup>24</sup>, Andrew W. Rollins<sup>25</sup>, Thomas B. Ryerson<sup>26</sup>, Gregory P. Schill<sup>27</sup>, Kanako Sekimoto<sup>28</sup>, Chelsea Thompson<sup>8</sup>, Kenneth L Thornhill<sup>10</sup>, Joel A Thornton<sup>13</sup>, Kirk Ullmann<sup>4</sup>, Carsten Warneke<sup>3</sup>, Rebecca Ann Washenfelder<sup>29</sup>, Bernadett Weinzierl<sup>11</sup>, Elizabeth Brooke Wiggins<sup>30</sup>, Christina Williamson<sup>5</sup>, Edward L Winstead<sup>10</sup>, Armin Wisthaler<sup>22</sup>, Caroline Womack<sup>31</sup>, and Steven S. S Brown<sup>25</sup>

<sup>1</sup>Paul Scherrer Institute

<sup>2</sup>NOAA Chemical Sciences Lab

<sup>3</sup>National Oceanic and Atmospheric Administration (NOAA)

<sup>4</sup>National Center for Atmospheric Research (UCAR)

<sup>5</sup>Cooperative Institute for Research in Environmental Sciences

<sup>6</sup>University Savoie Mont Blan

<sup>7</sup>NASA Ames Research Center

<sup>8</sup>University of Colorado Boulder

<sup>9</sup>CIRES, Univsersity of CO

<sup>10</sup>NASA Langley Research Center

<sup>11</sup>University of Vienna

<sup>12</sup>National Center for Atmospheric Research

<sup>13</sup>University of Washington

<sup>14</sup>University of Colorado

<sup>15</sup>Forschungszentrum Jülich GmbH

<sup>16</sup>Univ. of Colorado Boulder

<sup>17</sup>EPA

<sup>18</sup>Environment Canada

<sup>19</sup>Florida State University

<sup>20</sup>Department of Atmospheric Science, Colorado State University

<sup>21</sup>Aerodyne Research Inc

<sup>22</sup>University of Innsbruck

<sup>23</sup>CDPHE

<sup>24</sup>National Oceanic and Atmospheric Administration

<sup>25</sup>NOAA Earth System Research Laboratory

<sup>26</sup>Scientific Aviation

<sup>27</sup>Earth System Research Laboratory

<sup>28</sup>Yokoama City University

<sup>29</sup>NOAA

<sup>30</sup>NASA Langley

<sup>31</sup>NOAA Earth System Research Lab

November 24, 2023

## Abstract

Heterogeneous chemical cycles of pyrogenic nitrogen and halides influence tropospheric ozone and affect the stratosphere during extreme pyrocumulonimbus (PyroCB) events. We report field-derived N<sub>2</sub>O<sub>5</sub> uptake coefficients,  $\gamma(N_2O_5)$ , and ClNO<sub>2</sub> yields,  $\varphi(ClNO_2)$ , from two aircraft campaigns observing fresh smoke in the lower and mid troposphere and processed/aged smoke in the upper troposphere and lower stratosphere (UTLS). Derived  $\varphi(ClNO_2)$  varied across the full 0–1 range but was typically < 0.5 and smallest in a PyroCB (< 0.05). Derived  $\gamma(N_2O_5)$  was low in agricultural smoke ( $0.2\text{--}3.6 \times 10^{-3}$ ), extremely low in mid-tropospheric wildfire smoke ( $0.1 \times 10^{-3}$ ), but larger in PyroCB processed smoke ( $0.7\text{--}5.0 \times 10^{-3}$ ). Aged BB aerosol in the UTLS had a higher median  $\gamma(N_2O_5)$  of  $17 \times 10^{-3}$  that increased with sulfate and liquid water, but that was nevertheless 1–2 orders of magnitude lower than values for aqueous sulfuric aerosol used in stratospheric models.

1 **Airborne Observations Constrain Heterogeneous Nitrogen and Halogen Chemistry  
2 on Tropospheric and Stratospheric Biomass Burning Aerosol**

3

4 **Zachary C.J. Decker<sup>1,2,3,a</sup>, Gordon A. Novak<sup>1,2</sup>, Kenneth Aikin<sup>1,2</sup>, Patrick R. Veres<sup>1,b</sup>, J.  
5 Andrew Neuman<sup>1,2</sup>, Ilann Bourgeois<sup>1,2,c</sup>, T. Paul Bui<sup>4</sup>, Pedro Campuzano-Jost<sup>2,3</sup>, Matthew M.  
6 Coggon<sup>1,2</sup>, Douglas A. Day<sup>2,3</sup>, Joshua P. DiGangi<sup>5</sup>, Glenn S. Diskin<sup>5</sup>, Maximilian Dollner<sup>6</sup>,  
7 Alessandro Franchin<sup>1,2,7</sup>, Carley D. Fredrickson<sup>8</sup>, Karl D. Froyd<sup>1,2</sup>, Georgios I. Gkatzelis<sup>1,2,d</sup>,  
8 Hongyu Guo<sup>2,3</sup>, Samuel R. Hall<sup>7</sup>, Hannah Halliday<sup>5</sup>, Katherine Hayden<sup>9</sup>, Christopher D.  
9 Holmes<sup>9</sup>, Jose L. Jimenez<sup>2,3</sup>, Agnieszka Kupc<sup>1,2,6</sup>, Jakob Lindaas<sup>11</sup>, Ann M. Middlebrook<sup>1</sup>,  
10 Richard H. Moore<sup>5</sup>, Benjamin A. Nault<sup>12</sup>, John B. Nowak<sup>5</sup>, Demetrios Pagonis<sup>2,3,e</sup>, Brett B.  
11 Palm<sup>8,b</sup>, Jeff Peischl<sup>1,2</sup>, Felix M. Piel<sup>13,14</sup>, Pamela S. Rickly<sup>1,2,f</sup>, Michael A. Robinson<sup>1,2,3</sup>,  
12 Andrew W. Rollins<sup>1</sup>, Thomas B. Ryerson<sup>1</sup>, Gregory P. Schill<sup>1</sup>, Kanako Sekimoto<sup>15</sup>, Chelsea R.  
13 Thompson<sup>1</sup>, Kenneth L. Thornhill<sup>5,16</sup>, Joel A. Thornton<sup>8</sup>, Kirk Ullmann<sup>7</sup>, Carsten Warneke<sup>1</sup>,  
14 Rebecca A. Washenfelder<sup>1,g</sup>, Bernadett Weinzierl<sup>6</sup>, Elizabeth B. Wiggins<sup>5</sup>, Christina J.  
15 Williamson<sup>1,2,h,i</sup>, Edward L. Winstead<sup>5,16</sup>, Armin Wisthaler<sup>13,14</sup>, Caroline C. Womack<sup>1,2</sup>, Steven  
16 S. Brown<sup>1,3</sup>**

17 <sup>1</sup>NOAA Chemical Sciences Laboratory (CSL), Boulder, CO, USA

18 <sup>2</sup>Cooperative Institute for Research in Environmental Sciences, University of Colorado Boulder,  
19 Boulder, CO, USA

20 <sup>3</sup>Department of Chemistry, University of Colorado Boulder, Boulder, CO, USA

21 <sup>4</sup>NASA Ames Research Center, Moffett Field, CA, USA

22 <sup>5</sup>NASA Langley Research Center, MS 483, Hampton, VA, USA

23 <sup>6</sup>Faculty of Physics, Aerosol Physics and Environmental Physics, University of Vienna, Vienna,  
24 Austria

25 <sup>7</sup>Atmospheric Chemistry Observations and Modeling Laboratory, National Center for  
26 Atmospheric Research, Boulder, CO, USA

27 <sup>8</sup>Department of Atmospheric Sciences, University of Washington, Seattle, WA, United States

28 <sup>9</sup>Air Quality Research Division (AQRD), Environment and Climate Change Canada, Toronto  
29 M3H 5T4, Ontario, Canada

30 <sup>10</sup>Department of Earth, Ocean, and Atmospheric Science, Florida State University, Tallahassee,  
31 FL, USA

32 <sup>11</sup>Department of Atmospheric Science, Colorado State University, Fort Collins, CO, USA

33 <sup>12</sup>Center for Aerosol and Cloud Chemistry, Aerodyne Research, Inc., Billerica, MA, USA

34 <sup>13</sup>Institute for Ion Physics and Applied Physics, University of Innsbruck, 6020 Innsbruck, Austria

35 <sup>14</sup>Department of Chemistry, University of Oslo, 0315 Oslo, Norway

36   <sup>15</sup>Graduate School of Nanobioscience, Yokohama City University, Yokohama, Kanagawa, 236-  
37   0027, Japan

38   <sup>16</sup>Science Systems and Applications, Inc. (SSAI), Hampton, VA, USA

39   <sup>a</sup>Now at Laboratory of Atmospheric Chemistry, Paul Scherrer Institute (PSI), 5232 Villigen,  
40   Switzerland

41   <sup>b</sup>now at National Center for Atmospheric Research, Boulder, CO, USA

42   <sup>c</sup>now at Université Savoie Mont Blanc, INRAE, CARRTEL, 74200 Thonon-les-Bains, France

43   <sup>d</sup>Now at Institute of Energy and Climate Research, IEK-8: Troposphere, Forschungszentrum  
44   Jülich GmbH, Jülich, Germany

45   <sup>e</sup>now at Department of Chemistry and Biochemistry, Weber State University, Ogden, UT, USA

46   <sup>f</sup>now at Colorado Department of Public Health and Environment, 4300 Cherry Creek S Dr,  
47   Denver, CO, USA

48   <sup>g</sup>now at Cooperative Institute for Research in Environmental Sciences, University of Colorado  
49   Boulder, CO, USA

50   <sup>h</sup>now at Finnish Meteorological Institute, Erik Palmenin Aukio 1, 00560 Helsinki, Finland

51   <sup>i</sup>now at Institute for Atmospheric and Earth System Research/Physics, Faculty of Science,  
52   University of Helsinki, P.O. Box 64, 00014 Helsinki, Finland

53

54   Corresponding authors: Steven Brown ([steven.s.brown@noaa.gov](mailto:steven.s.brown@noaa.gov)) and Zachary Decker  
55   ([ZacharyCJDecker@gmail.com](mailto:ZacharyCJDecker@gmail.com))

56   **Key Points:**

- 57   • N<sub>2</sub>O<sub>5</sub> uptake coefficients are low on young biomass burning smoke and increase with  
58   transport through a PyroCB and UTLS aging
- 59   • ClNO<sub>2</sub> formation is active on biomass burning particles, but decreases with transport to  
60   the UTLS
- 61   • N<sub>2</sub>O<sub>5</sub> uptake coefficients on aged biomass burning particles in the UTLS are significantly  
62   lower than those used in model parameterizations

64 **Abstract**

65 Heterogeneous chemical cycles of pyrogenic nitrogen and halides influence tropospheric ozone  
 66 and affect the stratosphere during extreme pyrocumulonimbus (PyroCB) events. We report field-  
 67 derived  $\text{N}_2\text{O}_5$  uptake coefficients,  $\gamma(\text{N}_2\text{O}_5)$ , and  $\text{ClNO}_2$  yields,  $\varphi(\text{ClNO}_2)$ , from two aircraft  
 68 campaigns observing fresh smoke in the lower and mid troposphere and processed/aged smoke  
 69 in the upper troposphere and lower stratosphere (UTLS). Derived  $\varphi(\text{ClNO}_2)$  varied across the  
 70 full 0–1 range but was typically  $< 0.5$  and smallest in a PyroCB ( $< 0.05$ ). Derived  $\gamma(\text{N}_2\text{O}_5)$  was  
 71 low in agricultural smoke ( $0.2\text{--}3.6 \times 10^{-3}$ ), extremely low in mid-tropospheric wildfire smoke  
 72 ( $0.1 \times 10^{-3}$ ), but larger in PyroCB processed smoke ( $0.7\text{--}5.0 \times 10^{-3}$ ). Aged BB aerosol in the  
 73 UTLS had a higher median  $\gamma(\text{N}_2\text{O}_5)$  of  $17 \times 10^{-3}$  that increased with sulfate and liquid water, but  
 74 that was nevertheless 1–2 orders of magnitude lower than values for aqueous sulfuric aerosol  
 75 used in stratospheric models.

76 **Plain Language Summary**

77 The injection of reactive material into Earth's atmosphere from fires affects atmospheric  
 78 composition at regional and hemispheric scales. Reported stratospheric ozone depletion during  
 79 extreme events, such as the 2020 Australian wildfires, illustrates one example of fire impacts and  
 80 the role of heterogeneous (gas-particle) processes. We report field quantification of rates and  
 81 product yields from airborne observations of smoke. Extremely slow heterogeneous reaction  
 82 rates on young smoke increase with transport and aging, but upper atmospheric values are still a  
 83 factor of 10 slower than parameterizations used in stratospheric models. Heterogeneous  
 84 production of  $\text{ClNO}_2$ , a major lower atmospheric chlorine activation pathway, may be active on  
 85 biomass burning aerosol in the upper atmosphere.

86 **1 Introduction**

87 Biomass burning (BB) impacts global atmospheric chemical processes and is increasing  
 88 regionally due to climate-change-induced trends in fire weather [Jones *et al.*, 2022]. Fires emit  
 89 nitrogen oxides ( $\text{NO} + \text{NO}_2 = \text{NO}_x$ ), volatile organic compounds (VOCs) and aerosol that affect  
 90 tropospheric oxidants [Koss *et al.*, 2018]. Roughly 10% of global inorganic chloride enters the  
 91 atmosphere by BB [Wang *et al.*, 2019], and a small fraction may be subsequently activated to  
 92 inorganic chlorine radicals. The co-emission of  $\text{NO}_x$  and VOCs enhances tropospheric  $\text{O}_3$   
 93 globally on a scale comparable to, or greater than, urban pollution [Bourgeois *et al.*, 2021; Xu *et*  
 94 *al.*, 2021].

95 Large wildfires can form pyrocumulonimbus (PyroCB) towers [Peterson *et al.*, 2021;  
 96 Peterson *et al.*, 2022] that loft pyrogenic emissions to the upper troposphere / lower stratosphere  
 97 (UTLS). Aerosol injection from the 2019–2020 Australian New Year fires altered the  
 98 partitioning of total reactive chlorine ( $\text{Cl}_y$ ) and nitrogen ( $\text{NO}_y$ ) species and led to stratospheric  $\text{O}_3$   
 99 loss through heterogeneous reactions [Bernath *et al.*, 2022; Solomon *et al.*, 2022; Solomon *et al.*,  
 100 2023; Strahan *et al.*, 2022]. One of the major heterogeneous reactions is uptake of  $\text{N}_2\text{O}_5$ , which  
 101 in stratospheric models produces exclusively nitric acid,  $\text{HNO}_3$  [Küll *et al.*, 2002; Zambri *et al.*,  
 102 2019].

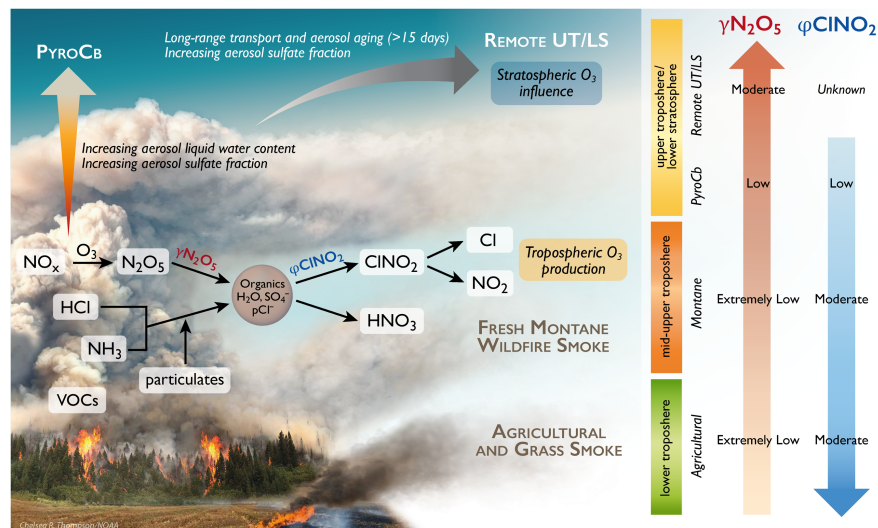


104 Here,  $\gamma$  is the reactive uptake coefficient [Ravishankara, 1997]. Reaction (1) influences  
 105  $\text{NO}_x$  and  $\text{O}_3$  in both the stratosphere and troposphere by altering the partitioning of reactive  
 106 nitrogen and the availability of  $\text{NO}_x$  [Dentener and Crutzen, 1993; Solomon, 1999].

107 Tropospheric observations have shown substantial yields of nitryl chloride,  $\text{ClNO}_2$ , from  
 108 chloride-containing aerosol [McDuffie *et al.*, 2018a], represented below as reaction with HCl.



110 Photolysis of  $\text{ClNO}_2$  produces Cl. The yield,  $\phi$ , for R2 is the molar ratio of  $\text{ClNO}_2$   
 111 produced per  $\text{N}_2\text{O}_5$  reacted. Due in part to the lack of chloride partitioning to highly-acidic  
 112 stratospheric aerosol, R2 has been considered an unimportant contribution to stratospheric  
 113 halogen activation [Solomon, 1999] despite its prevalence in the troposphere. Figure 1 illustrates  
 114 biomass burning emissions to and heterogeneous chemistry in different regions of the  
 115 atmosphere.



116 **Figure 1.** Biomass burning emission to different altitudes and heterogeneous chemistry of  $\text{N}_2\text{O}_5$   
 117 and  $\text{ClNO}_2$ . Arrows on the right-hand side illustrate trends in heterogeneous parameters,  $\gamma(\text{N}_2\text{O}_5)$   
 118 and  $\phi(\text{ClNO}_2)$ , determined from aircraft observations in this work.

119 Rates and yields of  $\text{N}_2\text{O}_5$  heterogeneous chemistry on BB particles are uncertain,  
 120 especially in the UTLS [Solomon *et al.*, 2022; Strahan *et al.*, 2022; Yu *et al.*, 2021]. Models  
 121 assume similarity between BB and volcanic particles but are unable to reproduce remote sensing  
 122 observations of  $\text{Cl}_y$  and  $\text{NO}_y$ , suggesting substantial differences in heterogeneous chemistry.  
 123 There exist limited BB laboratory studies on  $\gamma(\text{N}_2\text{O}_5)$  or  $\phi(\text{ClNO}_2)$  [Ahern *et al.*, 2018;  
 124 Goldberger *et al.*, 2019; Jahl *et al.*, 2021] and, to our knowledge, there are no field-derived  
 125 values. Tropospheric and stratospheric models of BB impacts are poorly constrained for  $\gamma(\text{N}_2\text{O}_5)$   
 126 and have not considered  $\phi(\text{ClNO}_2)$ .

127 We present aircraft observations of  $\text{N}_2\text{O}_5$ ,  $\text{ClNO}_2$  and field-derived values for  $\gamma(\text{N}_2\text{O}_5)$   
 128 and  $\phi(\text{ClNO}_2)$  in smoke. The analysis utilizes aircraft observations from the 2019 Fire Influence  
 129 on Regional to Global Environments and Air Quality (FIREX-AQ) campaign [Warneke *et al.*,  
 130 2023] and the 2017–2018 Atmospheric Tomography mission (ATom) [Thompson *et al.*, 2022].  
 131 We derive  $\gamma(\text{N}_2\text{O}_5)$  and  $\phi(\text{ClNO}_2)$  for montane and agricultural smoke in the troposphere and a

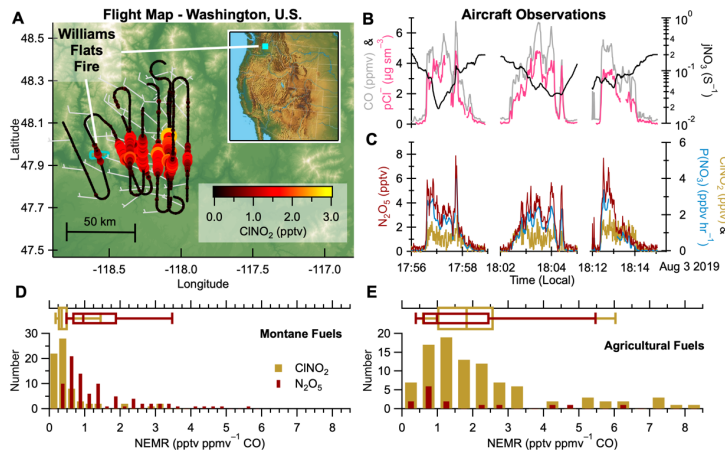
133 PyroCB injection of smoke to the upper troposphere from FIREX-AQ. We derive  $\gamma(\text{N}_2\text{O}_5)$  for  
 134 stratospheric BB-influenced aerosol from ATom. Derived  $\text{N}_2\text{O}_5$  uptake coefficients are  
 135 considerably lower than current model parameterizations. Halogen activation through  $\text{ClNO}_2$   
 136 from  $\text{NO}_x$  and particulate chloride ( $\text{pCl}^-$ ) is prevalent in low altitudes and possible, yet  
 137 unquantified, at high altitude.

## 138 2 Results and Discussion

### 139 2.1 $\text{ClNO}_2$ and $\text{N}_2\text{O}_5$ Observations

140 Figure 2A shows the flight track of the NASA DC-8 aircraft sampling the Williams Flats  
 141 fire during FIREX-AQ on 3 Aug 2019 colored and sized by observed  $\text{ClNO}_2$ . Both  $\text{N}_2\text{O}_5$  and  
 142  $\text{ClNO}_2$  exhibit clear enhancements despite significant photolysis rates of  $\text{NO}_3$  ( $j\text{NO}_3$ ) (Figure 2B-  
 143 C). These enhancements are associated with CO, a smoke tracer, and rapid ( $>1 \text{ ppbv hr}^{-1}$ )  $\text{NO}_3$   
 144 production,  $P(\text{NO}_3) = k[\text{NO}_2][\text{O}_3]$ , where  $k$  is the bimolecular rate coefficient for reaction of  $\text{NO}_2$   
 145 with  $\text{O}_3$ .

146 Median  $j\text{NO}_3$  at the center of wildfire and agriculture plume transects ( $0.14 \text{ s}^{-1}$  and  $0.19 \text{ s}^{-1}$   
 147 respectively) were 15–30% lower than values outside of plumes ( $0.16$  and  $0.20 \text{ s}^{-1}$   
 148 respectively). In large wildfire plumes  $j\text{NO}_3$  attenuation was a factor of ten or more (Figure 2B  
 149 and C), but small agricultural plumes exhibited no attenuation (Figure S1). Previous analyses of  
 150 FIREX-AQ plumes found that  $\text{NO}_3$  photolysis and reaction with NO are not major  $\text{NO}_3$  loss  
 151 pathways regardless of time of day [Decker *et al.*, 2021a; Decker *et al.*, 2021b]. Rapid  $P(\text{NO}_3)$   
 152 together with large concentrations of highly reactive VOCs and aerosol surface area control  $\text{NO}_3$   
 153 and  $\text{N}_2\text{O}_5$  chemistry. Plumes with measurable daytime  $\text{N}_2\text{O}_5$  provide measures of  $\text{NO}_3$  reactivity  
 154 and  $\text{N}_2\text{O}_5$  heterogeneous uptake for these species that are otherwise important only at night in  
 155 non-fire environments.



157 **Figure 2.** **A.** NASA DC-8 flight tracks colored and sized by  $\text{ClNO}_2$  mixing ratio for the Williams  
 158 Flats fire plume on Aug 3. The inset map shows the approximate location of sampling in  
 159 Washington State. **B.** Observations of  $\text{CO}$  (grey),  $\text{pCl}^-$  (pink), and  $j\text{NO}_3$  (black) and **C.**  $\text{N}_2\text{O}_5$   
 160 (red),  $\text{ClNO}_2$  (yellow) and  $\text{P}(\text{NO}_3)$  (blue) for a subset of crosswind plume transects. **D & E.**  
 161 Histogram of  $\text{N}_2\text{O}_5$  and  $\text{ClNO}_2$  NEMRs from all montane (D) and agricultural (E) fires. Box  
 162 plots show 10<sup>th</sup>, 25<sup>th</sup>, 50<sup>th</sup>, 75<sup>th</sup>, and 90<sup>th</sup> percentiles.

163        The Normalized Excess Mixing Ratio (NEMR) measures the above background  
 164        enhancements of a compound  $x$  relative to the smoke tracer CO (Table S2 and Figure S2-S4).  
 165        The median  $\text{N}_2\text{O}_5$  NEMR was 1.0 pptv  $\text{ppmv}^{-1}$  CO for both agricultural and montane fire groups  
 166        (Figure 2D and E). The  $\text{ClNO}_2$  NEMRs, by contrast, differ by a factor of  $\sim 6$  between montane  
 167        (0.3 pptv  $\text{ppmv}^{-1}$ ) and agricultural (1.8 pptv  $\text{ppmv}^{-1}$ ) fuels. Agricultural and grass burning emits  
 168        more  $\text{Cl}^-$  per kg of fuel burned (emission factor) when compared to temperate and boreal forest  
 169        burning [Akagi *et al.*, 2011; Liu *et al.*, 2016; May *et al.*, 2014]. Despite considerable variability,  
 170        the greater median  $\text{ClNO}_2$  NEMR for agricultural fires is consistent with the observed  
 171        differences in particulate chloride ( $\text{pCl}^-$ ). DC-8 and Twin Otter observations of the above  
 172        background  $\text{pCl}^-$  show that agricultural and grass smoke contains roughly  $16\times$  more  $\text{pCl}^-$  by  
 173        mass than montane smoke (Text S2 and Figure S5).

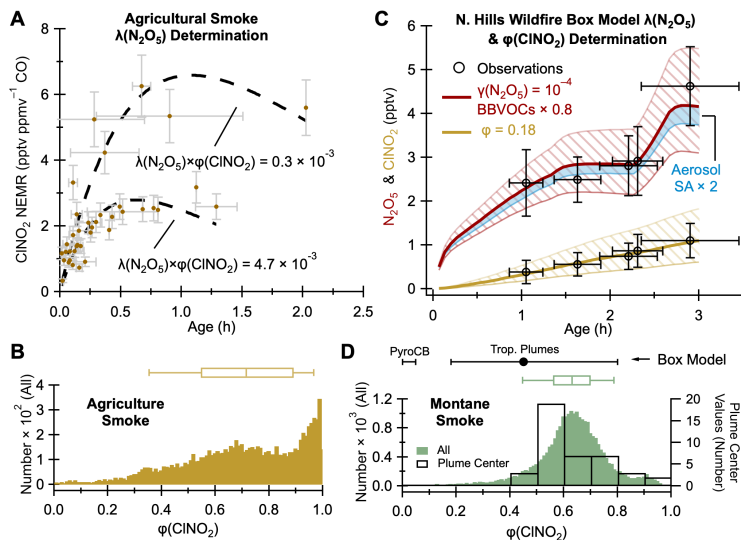
## 174        2.2 Montane and Agricultural Smoke

175        To derive  $\gamma(\text{N}_2\text{O}_5)$  from agricultural smoke, we use the calculated NEMR of  $\text{ClNO}_2$  as a  
 176        function of the physical plume age shown in Figure 3A. We combine the calculated  $\text{ClNO}_2$   
 177        NEMRs with the relationship between  $\gamma(\text{N}_2\text{O}_5)$  and  $\varphi(\text{ClNO}_2)$  below to estimate a  $\gamma(\text{N}_2\text{O}_5)$ .

$$178 \quad \gamma(\text{N}_2\text{O}_5) = 4 \times \frac{k_{\text{N}_2\text{O}_5}}{c \times SA} \quad (1)$$

$$179 \quad \varphi(\text{ClNO}_2) = \frac{k_{\text{ClNO}_2}}{k_{\text{N}_2\text{O}_5}} \quad (2)$$

180        Here  $c$  is the mean molecular speed of  $\text{N}_2\text{O}_5$  and  $SA$  is the aerosol surface area density.  
 181        Data are arbitrarily separated into low and high NEMR groups. The biexponential fit represents  
 182        first-order formation ( $k_{\text{ClNO}_2}$ ) and photolytic loss ( $j_{\text{ClNO}_2}$ ) of  $\text{ClNO}_2$ . Constraining the fit to an  
 183        observed median photolysis rate of  $j_{\text{ClNO}_2} = 3.3 \times 10^{-4} \text{ s}^{-1}$  (Figure S6A) we find  $k_{\text{ClNO}_2} = 2.0\text{--}5.8$   
 184         $\times 10^{-4} \text{ s}^{-1}$ . Aerosol surface area can vary widely across a plume transect and therefore we chose a  
 185        range ( $2\text{--}11 \times 10^3 \mu\text{m}^2 \text{ cm}^{-3}$ ) of observed  $SA$  representative of most observations in Figure 3A  
 186        (Figure S6B) and present a sensitivity analysis to this choice in Figure S6C. Finally, we use a  
 187        median observed temperature of 296 K to find  $\gamma(\text{N}_2\text{O}_5) \times \varphi(\text{ClNO}_2) = 0.3\text{--}4.7 \times 10^{-3}$ .



189 **Figure 3. A.** Agricultural fire ClNO<sub>2</sub> NEMRs vs. plume age. Dashed lines show biexponential  
 190 fits (see text). **B.** Parametrized  $\phi(ClNO_2)$  of agricultural smoke. **C.** Box model results (lines)  
 191 compared to observations (markers) of N<sub>2</sub>O<sub>5</sub> and ClNO<sub>2</sub> from the July 29 North Hills smoke  
 192 plume with  $\gamma(N_2O_5) = 10^{-4}$ . The hashed area shows changes to VOCs (N<sub>2</sub>O<sub>5</sub>) or yield (ClNO<sub>2</sub>)  
 193 that encompass observational uncertainty. Transparent blue area shows sensitivity to a factor of 2  
 194 increase in aerosol surface area. The apparent discontinuity of N<sub>2</sub>O<sub>5</sub> in the model is due to a  
 195 reduction in the photolysis rate at sunset (2.5 h of age). **D.** Parameterized  $\phi(ClNO_2)$  for montane  
 196 smoke (filled bars) and transect center observations used in the box model (empty bars). Box  
 197 model derived  $\phi(ClNO_2)$  is shown as horizontal ranges in black. The black marker indicates the  
 198 average of the five modeled plumes sampled in the lower troposphere. The range on the model-  
 199 derived  $\phi(ClNO_2)$  shows the range of the five modeled plumes. Note that within observation  
 200 uncertainty the full range is 0-1

201 To estimate  $\phi(ClNO_2)$  we use a laboratory-based parameterization based on observed  
 202 pCl<sup>-</sup> and calculated liquid water content (LWC), hereafter referred to as parameterized  $\phi(ClNO_2)$   
 203 (section 2.2, S1.4). Figure 3B shows parameterized  $\phi(ClNO_2)$  for all 1 Hz agriculture smoke  
 204 observations, with median  $\phi(ClNO_2)$  of 0.72. When considering only observations in Figure 2A,  
 205 used to determine  $\gamma(N_2O_5)$ , the median is 0.77. Previous field comparisons have shown that  
 206 parameterized  $\phi(ClNO_2)$  is likely an upper limit [McDuffie *et al.*, 2018b], and therefore the  
 207 derived  $\gamma(N_2O_5)$  is a lower limit range of  $0.2\text{--}3.6 \times 10^{-3}$ .

208 Montane smoke plumes included several cross-wind transects downwind, which allows  
 209 for  $\gamma(N_2O_5)$  and  $\phi(ClNO_2)$  determination in individual plumes using a constrained 0-D chemical  
 210 box model [Decker *et al.*, 2021a]. Model input values of  $\gamma(N_2O_5)$  were varied between  $10^{-4}$  and  
 211  $10^{-1}$  to minimize the difference between the model and observations of N<sub>2</sub>O<sub>5</sub>. The modeled N<sub>2</sub>O<sub>5</sub>  
 212 is sensitive to NO<sub>3</sub> loss to reactions with VOCs. The model uses VOC emissions from laboratory  
 213 burn emissions inventories, and these are also varied to improve the agreement between modeled  
 214 and observed N<sub>2</sub>O<sub>5</sub>. A comparison of modeled and observed VOCs shows that the majority of  
 215 the observation-model comparisons remain within the observation uncertainty. Lastly,  $\phi(ClNO_2)$   
 216 is varied between 0 and 1. Figures S7-S12 show complete model and observation comparisons.

217 Figure 3C shows a representative model to observation comparison for N<sub>2</sub>O<sub>5</sub> and ClNO<sub>2</sub>.  
 218 In all model runs, a  $\gamma(N_2O_5)$  of  $10^{-4}$  (one order of magnitude precision, see Figure S7) best  
 219 reproduces N<sub>2</sub>O<sub>5</sub> observations. In these five cases, values of  $\gamma(N_2O_5) \geq 10^{-3}$  cannot recreate the  
 220 N<sub>2</sub>O<sub>5</sub> observations without near or complete removal of VOCs, and values of  $\gamma(N_2O_5) < 10^{-4}$   
 221 require  $\phi(ClNO_2) > 1$  to reproduce ClNO<sub>2</sub>.

222 The box model derived  $\phi(ClNO_2)$  ranges from 0.18–0.80 but spans the entire 0-1 range  
 223 when considering the ClNO<sub>2</sub> observational uncertainty (Figure S13). The average model-derived  
 224  $\phi(ClNO_2)$  is 0.45 (Figure 3D, black marker). The average of transect-center-parameterized  
 225  $\phi(ClNO_2)$  is 0.65, similar to the average of all parameterized  $\phi(ClNO_2)$  of 0.62. Parameterized  
 226  $\phi(ClNO_2)$  exceeds the box model, similar to previous field derivations [McDuffie *et al.*, 2018b],  
 227 although >90% of parameterized  $\phi(ClNO_2)$  lies within the box model derived range (Figure 3D).  
 228 Lastly, the derived  $\phi(ClNO_2)$  of agricultural smoke is generally greater than montane smoke,  
 229 consistent with the greater pCl<sup>-</sup> in the former.

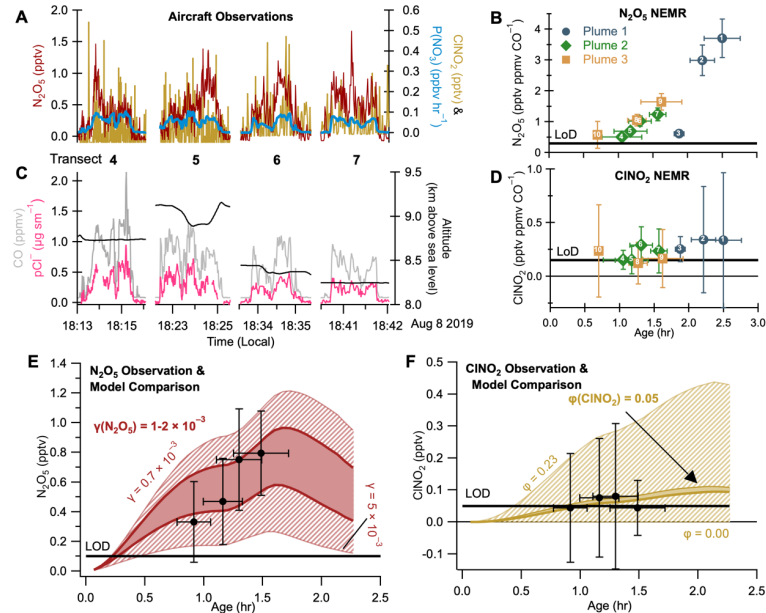
230 Values of  $\gamma(N_2O_5)$  derived here are smaller than values determined in urban air ( $\gamma(N_2O_5)$   
 231  $10^{-3}\text{--}10^{-1}$  [Brown and Stutz, 2012; McDuffie *et al.*, 2018a] and comparable to or lower than a  
 232 limited number of laboratory studies. A chamber study of pyrogenic aerosol for a wire grass fuel

(2.8–6 ± 0.6 × 10<sup>-3</sup>) and a long leaf pine needle fuel (2.5–3.2 ± 0.4 × 10<sup>-3</sup>) [Goldberger *et al.*, 2019] are similar to our agricultural fuels result. A flow-tube study of pyrogenic aerosol identified an increase of  $\gamma(\text{N}_2\text{O}_5)$  for high-chloride-containing BB fuels at relative humidity (RH) >80% [Jahrl *et al.*, 2021]. This is similar to the average RH (70%) for the agricultural smoke plumes here (Figure S14) and consistent with the observation of greater pCl<sup>-</sup> (Figure S5) and larger  $\gamma(\text{N}_2\text{O}_5)$  values (Figure 3) compared to montane smoke.

### 239 2.3 PyroCB Processed Smoke

The DC-8 sampled a PyroCB event from the Williams Flats fire on August 8 that reached 6–10 km above sea level, or 5.6 to 1.6 km below the mean tropopause height. We separate our analysis by plume number and transect number as defined by [Peterson *et al.*, 2022].

Observed P(NO<sub>3</sub>) and N<sub>2</sub>O<sub>5</sub> (Figure 4A) demonstrate the potential for heterogeneous chemistry in the PyroCB injection to the upper atmosphere. Calculated N<sub>2</sub>O<sub>5</sub> NEMR increases with calculated physical plume age when separated by plume number (Figure 4B). Enhancement of pCl<sup>-</sup> (Figure 4C) demonstrates the potential for ClNO<sub>2</sub> production. However, observations of ClNO<sub>2</sub> remained at or below the 1Hz I<sup>-</sup>-CIMS detection limit of 0.05 pptv in Figure 4A and D, limiting the ability to quantify its production. Figure S15 shows that the ClNO<sub>2</sub> signal within all PyroCB smoke observations (average ± 1- $\sigma$  of 0.03 ± 0.10 pptv) is statistically significantly greater ( $p<0.001$ ) than signal outside of the plume (average ± 1- $\sigma$  of 0.02 ± 0.06 pptv), but the data do not allow quantification of the amount of ClNO<sub>2</sub> within the PyroCB.



252

**Figure 4.** NASA DC-8 observations in a PyroCB. Panels A and B show plume 2 observations only (transects 4–7). **A & C.** Observations of N<sub>2</sub>O<sub>5</sub> (red), ClNO<sub>2</sub> (yellow) and P(NO<sub>3</sub>) (blue), CO (grey), pCl<sup>-</sup> (pink), and jNO<sub>3</sub> (black). **B & D.** NEMRs of N<sub>2</sub>O<sub>5</sub> and ClNO<sub>2</sub>. Markers and colors indicate the plume number, and white numbers indicate the transect number. The thick black line indicates the limit of detection (LoD). **E.** Transect center observations of N<sub>2</sub>O<sub>5</sub> (black) for plume 2 compared to the model N<sub>2</sub>O<sub>5</sub> for a range ( $7 \times 10^{-4}$ – $5 \times 10^{-3}$ ) of  $\gamma(\text{N}_2\text{O}_5)$ . **F.** Transect center observations of ClNO<sub>2</sub> (black) for plume 2 compared to the model-derived ClNO<sub>2</sub>. Solid color is

260 the result of a  $\phi(\text{ClNO}_2) = 0.05$  and a  $\gamma(\text{N}_2\text{O}_5) = 1\text{--}2 \times 10^{-3}$  and the hashed area shows a range of  
261 possible  $\phi(\text{ClNO}_2)$ .

262 Aerosol data are unavailable for plume 3, and plume 1 did not have sufficient semi-  
263 Lagrangian crosswind transects required to constrain the model. Therefore, the box model is  
264 used to derive  $\gamma(\text{N}_2\text{O}_5)$  and to place an upper limit on  $\phi(\text{ClNO}_2)$  for plume 2 only. The model  
265 derived  $\gamma(\text{N}_2\text{O}_5) = 0.7\text{--}5.0 \times 10^{-3}$  (Figure 4E), which is a factor of  $7\text{--}50 \times$  greater than the  
266  $\gamma(\text{N}_2\text{O}_5)$  values from plumes produced by the same fire but sampled in the lower troposphere.

267 The model predicts  $\phi(\text{ClNO}_2) < 0.05$  to match observations at or below the detection  
268 limit (or 0.05 at the LoD), although  $\phi(\text{ClNO}_2)$  may be up to 0.23 within the  $1-\sigma$  determined  
269  $\text{ClNO}_2$  measurement uncertainty ( $15\% + 0.05$  pptv). The average parameterized  $\phi(\text{ClNO}_2)$  (0.53)  
270 is also lower than tropospheric smoke from the same fire (Figure S16) as a result of increased  
271 calculated liquid water fraction (LWF, Figure S17) in the PyroCB. The presence of sufficient  
272  $\text{pCl}^-$  for average parameterized  $\phi(\text{ClNO}_2) > 0.5$  suggests that  $\text{ClNO}_2$  production may occur in  
273 PyroCB transported smoke, even if it was observed only at the detection limit in this daytime  
274 flight.

## 275 2.4 Aged UTLS pyrogenic aerosol

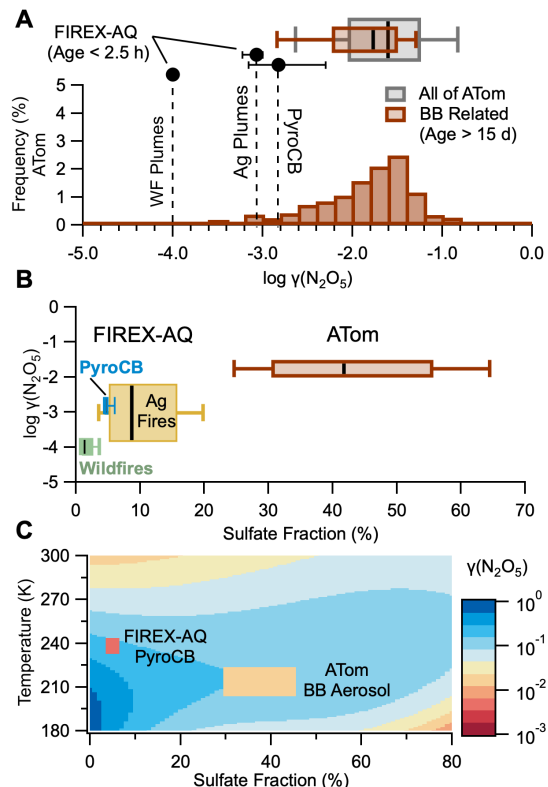
276 Observations from the ATom campaign provide  $\text{N}_2\text{O}_5$  observations in the UTLS. We  
277 separate our analysis into background and pyrogenic-influenced (defined as  $>75\%$  of aerosol  
278 number concentration containing pyrogenic markers, see SI). The pyrogenic aerosol is estimated  
279 to have a physical age of  $>15$  days. A diel model built on the framework of previous model  
280 determinations of  $\gamma(\text{N}_2\text{O}_5)$  in the lower troposphere [McDuffie *et al.*, 2018a] is constrained to  
281 chemical observations (see SI).

282 The diel model predicts the median  $\gamma(\text{N}_2\text{O}_5)$  from all background UTLS samples  
283 ( $N=3483$ ) is  $2.9 \times 10^{-2}$  as shown in Figure 5A (grey box and whiskers). The pyrogenic-  
284 influenced aerosol has a median  $\gamma(\text{N}_2\text{O}_5)$  of  $1.7 \times 10^{-2}$  (Figure 4A, brown) which is significantly  
285 different ( $p < 0.001$ ) than the background aerosol. We also consider a smaller subset of  
286 pyrogenic influenced aerosol from ATom previously identified by [Katich *et al.*, 2023] to have  
287 originated from PyroCB influence. The resulting  $\gamma(\text{N}_2\text{O}_5)$  of  $2.5 \times 10^{-2}$  is significantly ( $p = 0.01$ )  
288 less than background UTLS aerosol, and greater than our selection of pyrogenic influenced  
289 aerosol (Figure S18). Overall, the model predicts that pyrogenic aerosol has a lower rate of  $\text{N}_2\text{O}_5$   
290 uptake than background UTLS aerosol, yet substantially greater than pyrogenic aerosol in young  
291 tropospheric plumes.

292 The differences in  $\gamma(\text{N}_2\text{O}_5)$  across agricultural, montane, PyroCb, and UTLS data are  
293 associated with increased aerosol sulfate fraction. Figure 5B shows a positive trend in  
294  $\log(\gamma(\text{N}_2\text{O}_5))$  as a function of aerosol sulfate fraction distribution. The median sulfate fraction  
295 was 1, 5, 9 and 42% in recently-emitted montane, PyroCB, agricultural and aged stratospheric  
296 BB aerosol, respectively. Laboratory studies suggest organic coatings inhibit  $\text{N}_2\text{O}_5$  uptake, which  
297 is generally dependent on the organic layer composition and relative humidity [Gaston *et al.*,  
298 2014]. Conversely, increasing sulfate fraction is associated with increasing  $\gamma(\text{N}_2\text{O}_5)$  [McDuffie *et*  
299 *al.*, 2018a]. Sulfate in tropospheric BB plumes arises from oxidation of pyrogenic  $\text{SO}_2$  [Rickly *et*  
300 *al.*, 2022], whereas pyrogenic-influenced aerosol in the UTLS takes up sulfate during aging.

301 Current stratospheric models of BB impacts on stratospheric processes [Strahan *et al.*,  
302 2022; Yu *et al.*, 2021] use a  $\gamma(\text{N}_2\text{O}_5)$  based on aqueous sulfate aerosol. Figure 5C shows  $\gamma(\text{N}_2\text{O}_5)$

values from BB influenced aerosol are a factor of 10–100 lower than pure aqueous sulfate particles [Burkholder *et al.*, 2020]. BB particles are expected to condense organics from low-volatility VOC oxidation products [Palm *et al.*, 2020], forming organic layers that may reduce  $\gamma(N_2O_5)$ . Evidence of organic markers on stratospheric aerosol was found in some studies of stratospheric BB aerosol [Bernath *et al.*, 2022; Katich *et al.*, 2023], and BB aerosol markers are used here, by definition, to separate BB aerosol from background aerosol.



309 **Figure 5. A.** Comparison of the model-derived  $\gamma(N_2O_5)$  from FIREX-AQ and ATom. Markers show FIREX-AQ results, and the histograms show ATom BB-related  $\gamma(N_2O_5)$ . The box and whisker plots show the ATom BB-related (brown) and all of the ATom (grey) results from the UTLS. **B.** Log  $\gamma(N_2O_5)$  vs aerosol sulfate fraction for FIREX-AQ and ATom. **C.**  $\gamma(N_2O_5)$  parametrization from [Burkholder *et al.*, 2020] for aqueous sulfate particles used in stratospheric models compared to results from this work. Marker size represents the interquartile range of temperature and sulfate fraction in this work.

310 These results indicate  $\gamma(N_2O_5)$  values increase for BB particles transported from the  
 311 troposphere into the UTLS, but never reach values used in stratospheric models. Injection of the  
 312 chloride-containing aerosol observed in montane smoke or repartitioning of gas phase HCl to  
 313 particulate organics or reduced nitrogen [Solomon *et al.*, 2023] may result in a non-zero  $ClNO_2$   
 314 yield, thus introducing chlorine activation pathways currently not considered. Observations  
 315 presented here cannot quantify  $ClNO_2$  production on BB particles transported through a PyroCB  
 316 but demonstrate potential for this process. Observations of diffuse BB influenced particles in the  
 317 UTLS from ATom do not have reliable  $ClNO_2$  measurements, such that we are unable to assess  
 318  $ClNO_2$  production on aged, dilute UTLS BB influenced particles. Concentrated BB plumes  
 319 transported to the stratosphere through PyroCB events, such as the 2020 Australian fires, should  
 320

327 have heterogeneous chemistry similar to that observed here. Recent analysis of high-altitude  
328 aircraft data suggests a ubiquitous influence of such events on stratospheric aerosol composition  
329 [Katich *et al.*, 2023].

### 330 **3 Conclusions**

331 Uptake coefficients for N<sub>2</sub>O<sub>5</sub> determined from in situ observations are lower on BB  
332 aerosol than current model parameterizations. Figure 1 illustrates the observed trends in uptake  
333 coefficients from the lower to the upper atmosphere. The  $\gamma(N_2O_5)$  on dilute smoke-impacted  
334 particles derived in this study is already lower than model parameterizations but likely represents  
335 an upper limit for more concentrated smoke such as the 2020 Australian wildfires. We therefore  
336 suggest that models of the smoke impact to the UTLS will require revised parameterizations with  
337 reduced uptake coefficients.

338 Second [Solomon *et al.*, 2023] show that chloride uptake by the organic phase of smoke  
339 aerosol increases heterogeneous reaction rates of halogen-containing species, thereby activating  
340 chlorine radicals that participate in ozone destruction cycles. Our results demonstrate that N<sub>2</sub>O<sub>5</sub>  
341 uptake on chloride-containing smoke particles produces ClNO<sub>2</sub> in the lower atmosphere and has  
342 the potential to do so in the upper atmosphere, particularly with increased chloride partitioning to  
343 the aerosol phase. We suggest that ClNO<sub>2</sub> formation from N<sub>2</sub>O<sub>5</sub> uptake on smoke particles  
344 injected into the stratosphere during large PyroCB events may be a component of smoke-induced  
345 halogen activation cycles that influence stratospheric ozone.

### 346 **Acknowledgments**

347 We thank Charles A. Brock for particle sizing data from ATom. We thank William H.  
348 Brune and Alexander B. Thamess for OH/HO<sub>2</sub> data from ATom. We thank Daniel M. Murphy for  
349 PALMS particle type data from ATom. ZCJD, GAN, KA, IB, PCJ, MMC, DAD, AF, JLJ, DP,  
350 JP, PR, MAR, CRT, CW, and CCW, were supported by the NOAA cooperative agreement  
351 NA17OAR4320101. PCJ, HG, BAN, DP, DAD, and JLJ acknowledge support from NASA  
352 Earth Sciences Division (grant nos. NNX15AH33A, 80NSSC18K0630 and 80NSSC21K1451).  
353 C.D.F., B.B.P., and J.A.T. acknowledge support from the NOAA OAR Climate Program Office  
354 (grant no. NA17OAR4310012) CDF acknowledges support from the Future Investigators in  
355 NASA Earth and Space Science and Technology (FINESST) Grant Number 80NSSC20K1612.  
356 SRH and KU acknowledge support from NASA Earth Sciences Division (grant nos.  
357 80NSSC18K0638 and NNX15AG71A). Participation in ATom Mission flights by G.P.S.,  
358 K.D.F., and D.M.M. was supported by NOAA climate funding (no. NNH15AB12I).

### 359 **Data Availability Statement**

360 The aircraft data used in the study are publicly available at [https://www-](https://www-air.larc.nasa.gov/missions/firex-aq/)  
361 [air.larc.nasa.gov/missions/firex-aq/](https://www-air.larc.nasa.gov/missions/firex-aq/).

363

364

365 **References**

- 366 Ahern, A. T., L. Goldberger, L. Jahl, J. Thornton, and R. C. Sullivan (2018), Production of N<sub>2</sub>O<sub>5</sub>  
 367 and ClNO<sub>2</sub> through Nocturnal Processing of Biomass-Burning Aerosol, *Environmental*  
 368 *Science & Technology*, 52(2), 550-559, 10.1021/acs.est.7b04386.
- 369 Akagi, S. K., R. J. Yokelson, C. Wiedinmyer, M. J. Alvarado, J. S. Reid, T. Karl, J. D. Crounse,  
 370 and P. O. Wennberg (2011), Emission factors for open and domestic biomass burning for  
 371 use in atmospheric models, *Atmos. Chem. Phys.*, 11(9), 4039-4072, 10.5194/acp-11-  
 372 4039-2011.
- 373 Bernath, P., C. Boone, and J. Crouse (2022), Wildfire smoke destroys stratospheric ozone,  
 374 *Science*, 375(6586), 1292-1295, 10.1126/science.abm5611.
- 375 Bourgeois, I., J. Peischl, J. A. Neuman, S. S. Brown, C. R. Thompson, K. C. Aikin, H. M. Allen,  
 376 H. Angot, E. C. Apel, C. B. Baublitz, J. F. Brewer, P. Campuzano-Jost, R. Commane, J.  
 377 D. Crounse, B. C. Daube, J. P. DiGangi, G. S. Diskin, L. K. Emmons, A. M. Fiore, G. I.  
 378 Gkatzelis, A. Hills, R. S. Hornbrook, L. G. Huey, J. L. Jimenez, M. Kim, F. Lacey, K.  
 379 McKain, L. T. Murray, B. A. Nault, D. D. Parrish, E. Ray, C. Sweeney, D. Tanner, S. C.  
 380 Wofsy, and T. B. Ryerson (2021), Large contribution of biomass burning emissions to  
 381 ozone throughout the global remote troposphere, *Proceedings of the National Academy of*  
 382 *Sciences*, 118(52), e2109628118, 10.1073/pnas.2109628118.
- 383 Brown, S. S., and J. Stutz (2012), Nighttime Radical Observations and Chemistry, *Chem. Soc.*  
 384 *Reviews*, 41, 6405-6447, DOI: 10.1039/c2cs35181a.
- 385 Burkholder, J. B., J. P. D. Abbatt, C. Cappa, T. S. Dibble, C. E. Kolb, V. L. Orkin, D. M.  
 386 Wilmouth, S. P. Sander, J. R. Barker, J. D. Crounse, R. E. Huie, M. J. Kurylo, C. J.  
 387 Percival, and P. H. Wine (2020), *Chemical Kinetics and Photochemical Data for Use in*  
 388 *Atmospheric Studies*, JPL Publication 19-5, Pasadena, CA.
- 389 Decker, Z. C. J., M. A. Robinson, K. C. Barsanti, I. Bourgeois, M. M. Coggon, J. P. DiGangi, G.  
 390 S. Diskin, F. M. Flocke, A. Franchin, C. D. Fredrickson, G. I. Gkatzelis, S. R. Hall, H.  
 391 Halliday, C. D. Holmes, L. G. Huey, Y. R. Lee, J. Lindaas, A. M. Middlebrook, D. D.  
 392 Montzka, R. Moore, J. A. Neuman, J. B. Nowak, B. B. Palm, J. Peischl, F. Piel, P. S.  
 393 Rickly, A. W. Rollins, T. B. Ryerson, R. H. Schwantes, K. Sekimoto, L. Thornhill, J. A.  
 394 Thornton, G. S. Tyndall, K. Ullmann, P. Van Rooy, P. R. Veres, C. Warneke, R. A.  
 395 Washenfelder, A. J. Weinheimer, E. Wiggins, E. Winstead, A. Wisthaler, C. Womack,  
 396 and S. S. Brown (2021a), Nighttime and daytime dark oxidation chemistry in wildfire  
 397 plumes: an observation and model analysis of FIREX-AQ aircraft data, *Atmos. Chem.*  
 398 *Phys.*, 21(21), 16293-16317, 10.5194/acp-21-16293-2021.
- 399 Decker, Z. C. J., S. Wang, I. Bourgeois, P. Campuzano Jost, M. M. Coggon, J. P. DiGangi, G. S.  
 400 S. Diskin, F. M. Flocke, A. Franchin, C. D. Fredrickson, G. I. Gkatzelis, S. R. Hall, H.  
 401 Halliday, K. Hayden, C. D. Holmes, L. G. Huey, J. L. Jimenez, Y. R. Lee, J. Lindaas, A.  
 402 M. Middlebrook, D. D. Montzka, J. A. Neuman, J. B. Nowak, D. Pagonis, B. B. Palm, J.  
 403 Peischl, F. Piel, P. S. Rickly, M. A. Robinson, A. W. Rollins, T. B. Ryerson, K.  
 404 Sekimoto, J. A. Thornton, G. S. Tyndall, K. Ullmann, P. R. Veres, C. Warneke, R. A.  
 405 Washenfelder, A. J. Weinheimer, A. Wisthaler, C. Womack, and S. S. Brown (2021b),  
 406 Novel Analysis to Quantify Plume Crosswind Heterogeneity Applied to Biomass Burning  
 407 Smoke, *Environmental Science & Technology*, 55(23), 15646-15657,  
 408 10.1021/acs.est.1c03803.

- 409 Dentener, F. J., and P. J. Crutzen (1993), Reaction of N<sub>2</sub>O<sub>5</sub> on Tropospheric Aerosols: Impact on  
410 the Global Distributions of NO<sub>x</sub>, O<sub>3</sub>, and OH, *J. Geophys. Res.*, 98(D4), 7149-7163.
- 411 Gaston, C. J., J. A. Thornton, and N. L. Ng (2014), Reactive uptake of N<sub>2</sub>O<sub>5</sub> to internally mixed  
412 inorganic and organic particles: the role of organic carbon oxidation state and inferred  
413 organic phase separations, *Atmos. Chem. Phys.*, 14(11), 5693-5707, 10.5194/acp-14-  
414 5693-2014.
- 415 Goldberger, L. A., L. G. Jahl, J. A. Thornton, and R. C. Sullivan (2019), N<sub>2</sub>O<sub>5</sub> reactive uptake  
416 kinetics and chlorine activation on authentic biomass-burning aerosol, *Environmental  
417 Science: Processes & Impacts*, 21(10), 1684-1698, 10.1039/C9EM00330D.
- 418 Jahl, L. G., B. B. Bowers, L. G. Jahn, J. A. Thornton, and R. C. Sullivan (2021), Response of the  
419 Reaction Probability of N<sub>2</sub>O<sub>5</sub> with Authentic Biomass-Burning Aerosol to High Relative  
420 Humidity, *ACS Earth and Space Chemistry*, 5(10), 2587-2598,  
421 10.1021/acsearthspacechem.1c00227.
- 422 Jones, M. W., J. T. Abatzoglou, S. Veraverbeke, N. Andela, G. Lasslop, M. Forkel, A. J. P.  
423 Smith, C. Burton, R. A. Betts, G. R. van der Werf, S. Sitch, J. G. Canadell, C. Santín, C.  
424 Kolden, S. H. Doerr, and C. Le Quéré (2022), Global and Regional Trends and Drivers of  
425 Fire Under Climate Change, *Reviews of Geophysics*, 60(3), e2020RG000726,  
426 <https://doi.org/10.1029/2020RG000726>.
- 427 Katich, J. M., E. C. Apel, I. Bourgeois, C. A. Brock, T. P. Bui, P. Campuzano-Jost, R.  
428 Commane, B. Daube, M. Dollner, M. Fromm, K. D. Froyd, A. J. Hills, R. S. Hornbrook,  
429 J. L. Jimenez, A. Kupc, K. D. Lamb, K. McKain, F. Moore, D. M. Murphy, B. A. Nault,  
430 J. Peischl, A. E. Perring, D. A. Peterson, E. A. Ray, K. H. Rosenlof, T. Ryerson, G. P.  
431 Schill, J. C. Schroder, B. Weinzierl, C. Thompson, C. J. Williamson, S. C. Wofsy, P. Yu,  
432 and J. P. Schwarz (2023), Pyrocumulonimbus affect average stratospheric aerosol  
433 composition, *Science*, 379(6634), 815-820, 10.1126/science.add3101.
- 434 Koss, A. R., K. Sekimoto, J. B. Gilman, V. Selimovic, M. M. Coggon, K. J. Zarzana, B. Yuan,  
435 B. M. Lerner, S. S. Brown, J. L. Jimenez, J. Krechmer, J. M. Roberts, C. Warneke, R. J.  
436 Yokelson, and J. de Gouw (2018), Non-methane organic gas emissions from biomass  
437 burning: identification, quantification, and emission factors from PTR-ToF during the  
438 FIREX 2016 laboratory experiment, *Atmos. Chem. Phys.*, 18(5), 3299-3319,  
439 10.5194/acp-18-3299-2018.
- 440 Küll, V., M. Riese, X. Tie, T. Wiemert, G. Eidmann, D. Offermann, and G. P. Brasseur (2002),  
441 NO<sub>y</sub> partitioning and aerosol influences in the stratosphere, *J. Geophys. Res.*, 107(D23),  
442 8183, 10.1029/2001jd001246.
- 443 Liu, X., Y. Zhang, L. G. Huey, R. J. Yokelson, Y. Wang, J. L. Jimenez, P. Campuzano-Jost, A. J.  
444 Beyersdorf, D. R. Blake, Y. Choi, J. M. St. Clair, J. D. Crounse, D. A. Day, G. S. Diskin,  
445 A. Fried, S. R. Hall, T. F. Hanisco, L. E. King, S. Meinardi, T. Mikoviny, B. B. Palm, J.  
446 Peischl, A. E. Perring, I. B. Pollack, T. B. Ryerson, G. Sachse, J. P. Schwarz, I. J.  
447 Simpson, D. J. Tanner, K. L. Thornhill, K. Ullmann, R. J. Weber, P. O. Wennberg, A.  
448 Wisthaler, G. M. Wolfe, and L. D. Ziemba (2016), Agricultural fires in the southeastern  
449 U.S. during SEAC4RS: Emissions of trace gases and particles and evolution of ozone,  
450 reactive nitrogen, and organic aerosol, *Journal of Geophysical Research: Atmospheres*,  
451 121(12), 7383-7414, 10.1002/2016JD025040.
- 452 May, A. A., G. R. McMeeking, T. Lee, J. W. Taylor, J. S. Craven, I. Burling, A. P. Sullivan, S.  
453 Akagi, J. L. Collett Jr, M. Flynn, H. Coe, S. P. Urbanski, J. H. Seinfeld, R. J. Yokelson,  
454 and S. M. Kreidenweis (2014), Aerosol emissions from prescribed fires in the United

- 455 States: A synthesis of laboratory and aircraft measurements, *Journal of Geophysical*  
 456 *Research: Atmospheres*, 119(20), 11,826-811,849,  
 457 <https://doi.org/10.1002/2014JD021848>.
- 458 McDuffie, E., E., L. Fibiger Dorothy, P. Dubé William, F. Lopez-Hilfiker, H. Lee Ben, A.  
 459 Thornton Joel, V. Shah, L. Jaeglé, H. Guo, J. Weber Rodney, J. Michael Reeves, J.  
 460 Weinheimer Andrew, C. Schroder Jason, P. Campuzano-Jost, L. Jimenez Jose, E. Dibb  
 461 Jack, P. Veres, C. Ebben, L. Sparks Tamara, J. Wooldridge Paul, C. Cohen Ronald, S.  
 462 Hornbrook Rebecca, C. Apel Eric, T. Campos, R. Hall Samuel, K. Ullmann, and S. S.  
 463 Brown (2018a), Heterogeneous N<sub>2</sub>O<sub>5</sub> Uptake During Winter: Aircraft Measurements  
 464 During the 2015 WINTER Campaign and Critical Evaluation of Current  
 465 Parameterizations, *Journal of Geophysical Research: Atmospheres*, 123(8), 4345-4372,  
 466 10.1002/2018JD028336.
- 467 McDuffie, E. E., D. L. Fibiger, W. P. Dubé, F. Lopez Hilfiker, B. H. Lee, L. Jaeglé, H. Guo, R.  
 468 J. Weber, J. M. Reeves, A. J. Weinheimer, J. C. Schroder, P. Campuzano-Jost, J. L.  
 469 Jimenez, J. E. Dibb, P. Veres, C. Ebben, T. L. Sparks, P. J. Wooldridge, R. C. Cohen, T.  
 470 Campos, S. R. Hall, K. Ullmann, J. M. Roberts, J. A. Thornton, and S. S. Brown (2018b),  
 471 ClNO<sub>2</sub> Yields From Aircraft Measurements During the 2015 WINTER Campaign and  
 472 Critical Evaluation of the Current Parameterization, *Journal of Geophysical Research: Atmospheres*,  
 473 123(22), 12,994-913,015, 10.1029/2018JD029358.
- 474 Palm, B. B., Q. Peng, C. D. Fredrickson, B. H. Lee, L. A. Garofalo, M. A. Pothier, S. M.  
 475 Kreidenweis, D. K. Farmer, R. P. Pokhrel, Y. Shen, S. M. Murphy, W. Permar, L. Hu, T.  
 476 L. Campos, S. R. Hall, K. Ullmann, X. Zhang, F. Flocke, E. V. Fischer, and J. A.  
 477 Thornton (2020), Quantification of organic aerosol and brown carbon evolution in fresh  
 478 wildfire plumes, *Proceedings of the National Academy of Sciences*, 117(47), 29469,  
 479 10.1073/pnas.2012218117.
- 480 Peterson, D. A., M. D. Fromm, R. H. D. McRae, J. R. Campbell, E. J. Hyer, G. Taha, C. P.  
 481 Camacho, G. P. Kablick, C. C. Schmidt, and M. T. DeLand (2021), Australia's Black  
 482 Summer pyrocumulonimbus super outbreak reveals potential for increasingly extreme  
 483 stratospheric smoke events, *npj Climate and Atmospheric Science*, 4(1), 38,  
 484 10.1038/s41612-021-00192-9.
- 485 Peterson, D. A., L. H. Thapa, P. E. Saide, A. J. Soja, E. M. Gargulinski, E. J. Hyer, B. Weinzierl,  
 486 M. Dollner, M. Schöberl, P. P. Papin, S. Kondragunta, C. P. Camacho, C. Ichoku, R. H.  
 487 Moore, J. W. Hair, J. H. Crawford, P. E. Dennison, O. V. Kalashnikova, C. E. Bennese,  
 488 T. P. Bui, J. P. DiGangi, G. S. Diskin, M. A. Fenn, H. S. Halliday, J. Jimenez, J. B.  
 489 Nowak, C. Robinson, K. Sanchez, T. J. Shingler, L. Thornhill, E. B. Wiggins, E.  
 490 Winstead, and C. Xu (2022), Measurements from inside a Thunderstorm Driven by  
 491 Wildfire: The 2019 FIREX-AQ Field Experiment, *Bulletin of the American  
 492 Meteorological Society*, 10.1175/BAMS-D-21-0049.1.
- 493 Ravishankara, A. R. (1997), Heterogeneous and multiphase chemistry in the troposphere,  
 494 *Science*, 276, 1058-1065.
- 495 Rickly, P. S., H. Guo, P. Campuzano-Jost, J. L. Jimenez, G. M. Wolfe, R. Bennett, I. Bourgeois,  
 496 J. D. Crounse, J. E. Dibb, J. P. DiGangi, G. S. Diskin, M. Dollner, E. M. Gargulinski, S.  
 497 R. Hall, H. S. Halliday, T. F. Hanisco, R. A. Hannun, J. Liao, R. Moore, B. A. Nault, J.  
 498 B. Nowak, J. Peischl, C. E. Robinson, T. Ryerson, K. J. Sanchez, M. Schöberl, A. J. Soja,  
 499 J. M. St. Clair, K. L. Thornhill, K. Ullmann, P. O. Wennberg, B. Weinzierl, E. B.  
 500 Wiggins, E. L. Winstead, and A. W. Rollins (2022), Emission factors and evolution of

- 501 SO<sub>2</sub> measured from biomass burning in wildfires and agricultural fires, *Atmos. Chem.*  
502 *Phys.*, 22(23), 15603-15620, 10.5194/acp-22-15603-2022.
- 503 Solomon, S. (1999), Stratospheric ozone depletion: A review of concepts and history, *Reviews of*  
504 *Geophysics*, 37(3), 275-316, 10.1029/1999rg900008.
- 505 Solomon, S., K. Dube, K. Stone, P. Yu, D. Kinnison, B. Toon Owen, E. Strahan Susan, H.  
506 Rosenlof Karen, R. Portmann, S. Davis, W. Randel, P. Bernath, C. Boone, G. Bardeen  
507 Charles, A. Bourassa, D. Zawada, and D. Degenstein (2022), On the stratospheric  
508 chemistry of midlatitude wildfire smoke, *Proceedings of the National Academy of*  
509 *Sciences*, 119(10), e2117325119, 10.1073/pnas.2117325119.
- 510 Solomon, S., K. Stone, P. Yu, D. M. Murphy, D. Kinnison, A. R. Ravishankara, and P. Wang  
511 (2023), Chlorine activation and enhanced ozone depletion induced by wildfire aerosol,  
512 *Nature*, 615(7951), 259-264, 10.1038/s41586-022-05683-0.
- 513 Strahan, S. E., D. Smale, S. Solomon, G. Taha, M. R. Damon, S. D. Steenrod, N. Jones, B. Liley,  
514 R. Querel, and J. Robinson (2022), Unexpected Repartitioning of Stratospheric Inorganic  
515 Chlorine After the 2020 Australian Wildfires, *Geophysical Research Letters*, 49(14),  
516 e2022GL098290, <https://doi.org/10.1029/2022GL098290>.
- 517 Thompson, C. R., S. C. Wofsy, M. J. Prather, P. A. Newman, T. F. Hanisco, T. B. Ryerson, D.  
518 W. Fahey, E. C. Apel, C. A. Brock, W. H. Brune, K. Froyd, J. M. Katich, J. M. Nicely, J.  
519 Peischl, E. Ray, P. R. Veres, S. Wang, H. M. Allen, E. Asher, H. Bian, D. Blake, I.  
520 Bourgeois, J. Budney, T. P. Bui, A. Butler, P. Campuzano-Jost, C. Chang, M. Chin, R.  
521 Commane, G. Correa, J. D. Crounse, B. Daube, J. E. Dibb, J. P. DiGangi, G. S. Diskin,  
522 M. Dollner, J. W. Elkins, A. M. Fiore, C. M. Flynn, H. Guo, S. R. Hall, R. A. Hannun, A.  
523 Hills, E. J. Hintsas, A. Hodzic, R. S. Hornbrook, L. G. Huey, J. L. Jimenez, R. F. Keeling,  
524 M. J. Kim, A. Kupc, F. Lacey, L. R. Lait, J.-F. Lamarque, J. Liu, K. McKain, S.  
525 Meinardi, D. O. Miller, S. A. Montzka, F. L. Moore, E. J. Morgan, D. M. Murphy, L. T.  
526 Murray, B. A. Nault, J. A. Neuman, L. Nguyen, Y. Gonzalez, A. Rollins, K. Rosenlof, M.  
527 Sargent, G. Schill, J. P. Schwarz, J. M. S. Clair, S. D. Steenrod, B. B. Stephens, S. E.  
528 Strahan, S. A. Strode, C. Sweeney, A. B. Thamess, K. Ullmann, N. Wagner, R. Weber, B.  
529 Weinzierl, P. O. Wennberg, C. J. Williamson, G. M. Wolfe, and L. Zeng (2022), The  
530 NASA Atmospheric Tomography (ATom) Mission: Imaging the Chemistry of the Global  
531 Atmosphere, *Bulletin of the American Meteorological Society*, 103(3), E761-E790,  
532 10.1175/BAMS-D-20-0315.1.
- 533 Wang, X., D. J. Jacob, S. D. Eastham, M. P. Sulprizio, L. Zhu, Q. Chen, B. Alexander, T.  
534 Sherwen, M. J. Evans, B. H. Lee, J. D. Haskins, F. D. Lopez-Hilfiker, J. A. Thornton, G.  
535 L. Huey, and H. Liao (2019), The role of chlorine in global tropospheric chemistry,  
536 *Atmos. Chem. Phys.*, 19(6), 3981-4003, 10.5194/acp-19-3981-2019.
- 537 Warneke, C., J. P. Schwarz, J. Dibb, O. Kalashnikova, G. Frost, J. Al-Saad, S. S. Brown, W. A.  
538 Brewer, A. Soja, F. C. Seidel, R. A. Washenfelder, E. B. Wiggins, R. H. Moore, B. E.  
539 Anderson, C. Jordan, T. I. Yacovitch, S. C. Herndon, S. Liu, T. Kuwayama, D. Jaffe, N.  
540 Johnston, V. Selimovic, R. Yokelson, D. M. Giles, B. N. Holben, P. Goloub, I. Popovici,  
541 M. Trainer, A. Kumar, R. B. Pierce, D. Fahey, J. Roberts, E. M. Gargulinski, D. A.  
542 Peterson, X. Ye, L. H. Thapa, P. E. Saide, C. H. Fite, C. D. Holmes, S. Wang, M. M.  
543 Coggon, Z. C. J. Decker, C. E. Stockwell, L. Xu, G. Gkatzelis, K. Aikin, B. Lefer, J.  
544 Kaspari, D. Griffin, L. Zeng, R. Weber, M. Hastings, J. Chai, G. M. Wolfe, T. F.  
545 Hanisco, J. Liao, P. Campuzano Jost, H. Guo, J. L. Jimenez, J. Crawford, and F.-A. Q. S.  
546 T. The (2023), Fire Influence on Regional to Global Environments and Air Quality

- 547 (FIREX-AQ), *Journal of Geophysical Research: Atmospheres*, 128(2), e2022JD037758,  
548 <https://doi.org/10.1029/2022JD037758>.
- 549 Xu, L., D. Crounse John, T. Vasquez Krystal, H. Allen, O. Wennberg Paul, I. Bourgeois, S.  
550 Brown Steven, P. Campuzano-Jost, M. Coggon Matthew, H. Crawford James, P.  
551 DiGangi Joshua, S. Diskin Glenn, A. Fried, M. Gargulinski Emily, B. Gilman Jessica, I.  
552 Gkatzelis Georgios, H. Guo, W. Hair Johnathan, R. Hall Samuel, A. Halliday Hannah, F.  
553 Hanisco Thomas, A. Hannun Reem, D. Holmes Christopher, L. G. Huey, L. Jimenez  
554 Jose, A. Lamplugh, R. Lee Young, J. Liao, J. Lindaas, J. A. Neuman, B. Nowak John, J.  
555 Peischl, A. Peterson David, F. Piel, D. Richter, S. Rickly Pamela, A. Robinson Michael,  
556 W. Rollins Andrew, B. Ryerson Thomas, K. Sekimoto, V. Selimovic, T. Shingler, J. Soja  
557 Amber, M. St. Clair Jason, J. Tanner David, K. Ullmann, R. Veres Patrick, J. Walega, C.  
558 Warneke, A. Washenfelder Rebecca, P. Weibring, A. Wisthaler, M. Wolfe Glenn, C.  
559 Womack Caroline, and J. Yokelson Robert (2021), Ozone chemistry in western U.S.  
560 wildfire plumes, *Science Advances*, 7(50), eabl3648, 10.1126/sciadv.abl3648.
- 561 Yu, P., S. M. Davis, O. B. Toon, R. W. Portmann, C. G. Bardeen, J. E. Barnes, H. Telg, C.  
562 Maloney, and K. H. Rosenlof (2021), Persistent Stratospheric Warming Due to 2019–  
563 2020 Australian Wildfire Smoke, *Geophysical Research Letters*, 48(7), e2021GL092609,  
564 <https://doi.org/10.1029/2021GL092609>.
- 565 Zambri, B., S. Solomon, D. E. Kinnison, M. J. Mills, A. Schmidt, R. R. Neely III, A. E.  
566 Bourassa, D. A. Degenstein, and C. Z. Roth (2019), Modeled and Observed Volcanic  
567 Aerosol Control on Stratospheric NO<sub>y</sub> and Cl<sub>y</sub>, *Journal of Geophysical Research: Atmospheres*,  
568 124(17–18), 10283–10303, 10.1029/2019JD031111.
- 569

1 **Airborne Observations Constrain Heterogeneous Nitrogen and Halogen Chemistry  
2 on Tropospheric and Stratospheric Biomass Burning Aerosol**

3

4 **Zachary C.J. Decker<sup>1,2,3,a</sup>, Gordon A. Novak<sup>1,2</sup>, Kenneth Aikin<sup>1,2</sup>, Patrick R. Veres<sup>1,b</sup>, J.  
5 Andrew Neuman<sup>1,2</sup>, Ilann Bourgeois<sup>1,2,c</sup>, T. Paul Bui<sup>4</sup>, Pedro Campuzano-Jost<sup>2,3</sup>, Matthew M.  
6 Coggon<sup>1,2</sup>, Douglas A. Day<sup>2,3</sup>, Joshua P. DiGangi<sup>5</sup>, Glenn S. Diskin<sup>5</sup>, Maximilian Dollner<sup>6</sup>,  
7 Alessandro Franchin<sup>1,2,7</sup>, Carley D. Fredrickson<sup>8</sup>, Karl D. Froyd<sup>1,2</sup>, Georgios I. Gkatzelis<sup>1,2,d</sup>,  
8 Hongyu Guo<sup>2,3</sup>, Samuel R. Hall<sup>7</sup>, Hannah Halliday<sup>5</sup>, Katherine Hayden<sup>9</sup>, Christopher D.  
9 Holmes<sup>9</sup>, Jose L. Jimenez<sup>2,3</sup>, Agnieszka Kupc<sup>1,2,6</sup>, Jakob Lindaas<sup>11</sup>, Ann M. Middlebrook<sup>1</sup>,  
10 Richard H. Moore<sup>5</sup>, Benjamin A. Nault<sup>12</sup>, John B. Nowak<sup>5</sup>, Demetrios Pagonis<sup>2,3,e</sup>, Brett B.  
11 Palm<sup>8,b</sup>, Jeff Peischl<sup>1,2</sup>, Felix M. Piel<sup>13,14</sup>, Pamela S. Rickly<sup>1,2,f</sup>, Michael A. Robinson<sup>1,2,3</sup>,  
12 Andrew W. Rollins<sup>1</sup>, Thomas B. Ryerson<sup>1</sup>, Gregory P. Schill<sup>1</sup>, Kanako Sekimoto<sup>15</sup>, Chelsea R.  
13 Thompson<sup>1</sup>, Kenneth L. Thornhill<sup>5,16</sup>, Joel A. Thornton<sup>8</sup>, Kirk Ullmann<sup>7</sup>, Carsten Warneke<sup>1</sup>,  
14 Rebecca A. Washenfelder<sup>1,g</sup>, Bernadett Weinzierl<sup>6</sup>, Elizabeth B. Wiggins<sup>5</sup>, Christina J.  
15 Williamson<sup>1,2,h,i</sup>, Edward L. Winstead<sup>5,16</sup>, Armin Wisthaler<sup>13,14</sup>, Caroline C. Womack<sup>1,2</sup>, Steven  
16 S. Brown<sup>1,3</sup>**

17 <sup>1</sup>NOAA Chemical Sciences Laboratory (CSL), Boulder, CO, USA

18 <sup>2</sup>Cooperative Institute for Research in Environmental Sciences, University of Colorado Boulder,  
19 Boulder, CO, USA

20 <sup>3</sup>Department of Chemistry, University of Colorado Boulder, Boulder, CO, USA

21 <sup>4</sup>NASA Ames Research Center, Moffett Field, CA, USA

22 <sup>5</sup>NASA Langley Research Center, MS 483, Hampton, VA, USA

23 <sup>6</sup>Faculty of Physics, Aerosol Physics and Environmental Physics, University of Vienna, Vienna,  
24 Austria

25 <sup>7</sup>Atmospheric Chemistry Observations and Modeling Laboratory, National Center for  
26 Atmospheric Research, Boulder, CO, USA

27 <sup>8</sup>Department of Atmospheric Sciences, University of Washington, Seattle, WA, United States

28 <sup>9</sup>Air Quality Research Division (AQRD), Environment and Climate Change Canada, Toronto  
29 M3H 5T4, Ontario, Canada

30 <sup>10</sup>Department of Earth, Ocean, and Atmospheric Science, Florida State University, Tallahassee,  
31 FL, USA

32 <sup>11</sup>Department of Atmospheric Science, Colorado State University, Fort Collins, CO, USA

33 <sup>12</sup>Center for Aerosol and Cloud Chemistry, Aerodyne Research, Inc., Billerica, MA, USA

34 <sup>13</sup>Institute for Ion Physics and Applied Physics, University of Innsbruck, 6020 Innsbruck, Austria

35 <sup>14</sup>Department of Chemistry, University of Oslo, 0315 Oslo, Norway

36   <sup>15</sup>Graduate School of Nanobioscience, Yokohama City University, Yokohama, Kanagawa, 236-  
37   0027, Japan

38   <sup>16</sup>Science Systems and Applications, Inc. (SSAI), Hampton, VA, USA

39   <sup>a</sup>Now at Laboratory of Atmospheric Chemistry, Paul Scherrer Institute (PSI), 5232 Villigen,  
40   Switzerland

41   <sup>b</sup>now at National Center for Atmospheric Research, Boulder, CO, USA

42   <sup>c</sup>now at Université Savoie Mont Blanc, INRAE, CARRTEL, 74200 Thonon-les-Bains, France

43   <sup>d</sup>Now at Institute of Energy and Climate Research, IEK-8: Troposphere, Forschungszentrum  
44   Jülich GmbH, Jülich, Germany

45   <sup>e</sup>now at Department of Chemistry and Biochemistry, Weber State University, Ogden, UT, USA

46   <sup>f</sup>now at Colorado Department of Public Health and Environment, 4300 Cherry Creek S Dr,  
47   Denver, CO, USA

48   <sup>g</sup>now at Cooperative Institute for Research in Environmental Sciences, University of Colorado  
49   Boulder, CO, USA

50   <sup>h</sup>now at Finnish Meteorological Institute, Erik Palmenin Aukio 1, 00560 Helsinki, Finland

51   <sup>i</sup>now at Institute for Atmospheric and Earth System Research/Physics, Faculty of Science,  
52   University of Helsinki, P.O. Box 64, 00014 Helsinki, Finland

53

54   Corresponding authors: Steven Brown ([steven.s.brown@noaa.gov](mailto:steven.s.brown@noaa.gov)) and Zachary Decker  
55   ([ZacharyCJDecker@gmail.com](mailto:ZacharyCJDecker@gmail.com))

56   **Key Points:**

- 57
  - N<sub>2</sub>O<sub>5</sub> uptake coefficients are low on young biomass burning smoke and increase with  
58   transport through a PyroCB and UTLS aging
  - ClNO<sub>2</sub> formation is active on biomass burning particles, but decreases with transport to  
60   the UTLS
  - N<sub>2</sub>O<sub>5</sub> uptake coefficients on aged biomass burning particles in the UTLS are significantly  
62   lower than those used in model parameterizations

64 **Abstract**

65 Heterogeneous chemical cycles of pyrogenic nitrogen and halides influence tropospheric ozone  
 66 and affect the stratosphere during extreme pyrocumulonimbus (PyroCB) events. We report field-  
 67 derived  $\text{N}_2\text{O}_5$  uptake coefficients,  $\gamma(\text{N}_2\text{O}_5)$ , and  $\text{ClNO}_2$  yields,  $\varphi(\text{ClNO}_2)$ , from two aircraft  
 68 campaigns observing fresh smoke in the lower and mid troposphere and processed/aged smoke  
 69 in the upper troposphere and lower stratosphere (UTLS). Derived  $\varphi(\text{ClNO}_2)$  varied across the  
 70 full 0–1 range but was typically  $< 0.5$  and smallest in a PyroCB ( $< 0.05$ ). Derived  $\gamma(\text{N}_2\text{O}_5)$  was  
 71 low in agricultural smoke ( $0.2\text{--}3.6 \times 10^{-3}$ ), extremely low in mid-tropospheric wildfire smoke  
 72 ( $0.1 \times 10^{-3}$ ), but larger in PyroCB processed smoke ( $0.7\text{--}5.0 \times 10^{-3}$ ). Aged BB aerosol in the  
 73 UTLS had a higher median  $\gamma(\text{N}_2\text{O}_5)$  of  $17 \times 10^{-3}$  that increased with sulfate and liquid water, but  
 74 that was nevertheless 1–2 orders of magnitude lower than values for aqueous sulfuric aerosol  
 75 used in stratospheric models.

76 **Plain Language Summary**

77 The injection of reactive material into Earth's atmosphere from fires affects atmospheric  
 78 composition at regional and hemispheric scales. Reported stratospheric ozone depletion during  
 79 extreme events, such as the 2020 Australian wildfires, illustrates one example of fire impacts and  
 80 the role of heterogeneous (gas-particle) processes. We report field quantification of rates and  
 81 product yields from airborne observations of smoke. Extremely slow heterogeneous reaction  
 82 rates on young smoke increase with transport and aging, but upper atmospheric values are still a  
 83 factor of 10 slower than parameterizations used in stratospheric models. Heterogeneous  
 84 production of  $\text{ClNO}_2$ , a major lower atmospheric chlorine activation pathway, may be active on  
 85 biomass burning aerosol in the upper atmosphere.

86 **1 Introduction**

87 Biomass burning (BB) impacts global atmospheric chemical processes and is increasing  
 88 regionally due to climate-change-induced trends in fire weather [Jones *et al.*, 2022]. Fires emit  
 89 nitrogen oxides ( $\text{NO} + \text{NO}_2 = \text{NO}_x$ ), volatile organic compounds (VOCs) and aerosol that affect  
 90 tropospheric oxidants [Koss *et al.*, 2018]. Roughly 10% of global inorganic chloride enters the  
 91 atmosphere by BB [Wang *et al.*, 2019], and a small fraction may be subsequently activated to  
 92 inorganic chlorine radicals. The co-emission of  $\text{NO}_x$  and VOCs enhances tropospheric  $\text{O}_3$   
 93 globally on a scale comparable to, or greater than, urban pollution [Bourgeois *et al.*, 2021; Xu *et*  
 94 *al.*, 2021].

95 Large wildfires can form pyrocumulonimbus (PyroCB) towers [Peterson *et al.*, 2021;  
 96 Peterson *et al.*, 2022] that loft pyrogenic emissions to the upper troposphere / lower stratosphere  
 97 (UTLS). Aerosol injection from the 2019–2020 Australian New Year fires altered the  
 98 partitioning of total reactive chlorine ( $\text{Cl}_y$ ) and nitrogen ( $\text{NO}_y$ ) species and led to stratospheric  $\text{O}_3$   
 99 loss through heterogeneous reactions [Bernath *et al.*, 2022; Solomon *et al.*, 2022; Solomon *et al.*,  
 100 2023; Strahan *et al.*, 2022]. One of the major heterogeneous reactions is uptake of  $\text{N}_2\text{O}_5$ , which  
 101 in stratospheric models produces exclusively nitric acid,  $\text{HNO}_3$  [Küll *et al.*, 2002; Zambri *et al.*,  
 102 2019].

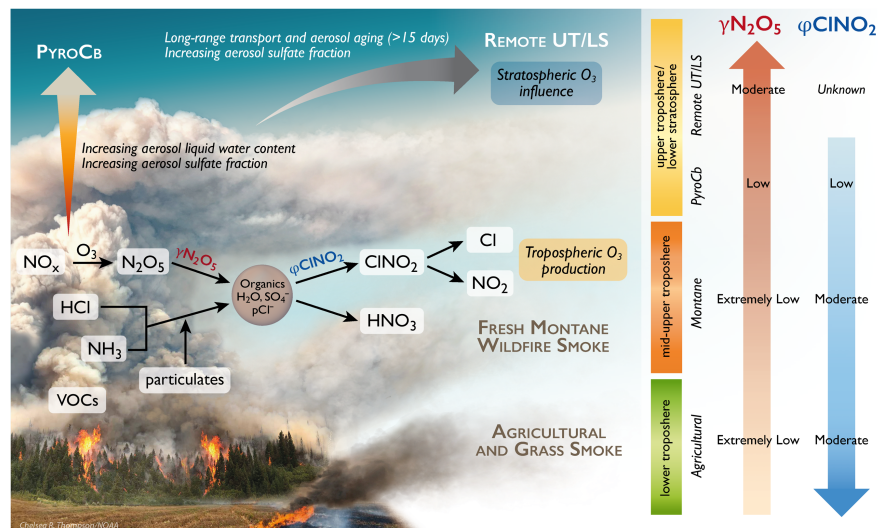


104 Here,  $\gamma$  is the reactive uptake coefficient [Ravishankara, 1997]. Reaction (1) influences  
 105  $\text{NO}_x$  and  $\text{O}_3$  in both the stratosphere and troposphere by altering the partitioning of reactive  
 106 nitrogen and the availability of  $\text{NO}_x$  [Dentener and Crutzen, 1993; Solomon, 1999].

107 Tropospheric observations have shown substantial yields of nitryl chloride,  $\text{ClNO}_2$ , from  
 108 chloride-containing aerosol [McDuffie *et al.*, 2018a], represented below as reaction with HCl.



110 Photolysis of  $\text{ClNO}_2$  produces Cl. The yield,  $\phi$ , for R2 is the molar ratio of  $\text{ClNO}_2$   
 111 produced per  $\text{N}_2\text{O}_5$  reacted. Due in part to the lack of chloride partitioning to highly-acidic  
 112 stratospheric aerosol, R2 has been considered an unimportant contribution to stratospheric  
 113 halogen activation [Solomon, 1999] despite its prevalence in the troposphere. Figure 1 illustrates  
 114 biomass burning emissions to and heterogeneous chemistry in different regions of the  
 115 atmosphere.



116 **Figure 1.** Biomass burning emission to different altitudes and heterogeneous chemistry of  $\text{N}_2\text{O}_5$   
 117 and  $\text{ClNO}_2$ . Arrows on the right-hand side illustrate trends in heterogeneous parameters,  $\gamma(\text{N}_2\text{O}_5)$   
 118 and  $\phi(\text{ClNO}_2)$ , determined from aircraft observations in this work.

119 Rates and yields of  $\text{N}_2\text{O}_5$  heterogeneous chemistry on BB particles are uncertain,  
 120 especially in the UTLS [Solomon *et al.*, 2022; Strahan *et al.*, 2022; Yu *et al.*, 2021]. Models  
 121 assume similarity between BB and volcanic particles but are unable to reproduce remote sensing  
 122 observations of  $\text{Cl}_y$  and  $\text{NO}_y$ , suggesting substantial differences in heterogeneous chemistry.  
 123 There exist limited BB laboratory studies on  $\gamma(\text{N}_2\text{O}_5)$  or  $\phi(\text{ClNO}_2)$  [Ahern *et al.*, 2018;  
 124 Goldberger *et al.*, 2019; Jahl *et al.*, 2021] and, to our knowledge, there are no field-derived  
 125 values. Tropospheric and stratospheric models of BB impacts are poorly constrained for  $\gamma(\text{N}_2\text{O}_5)$   
 126 and have not considered  $\phi(\text{ClNO}_2)$ .

127 We present aircraft observations of  $\text{N}_2\text{O}_5$ ,  $\text{ClNO}_2$  and field-derived values for  $\gamma(\text{N}_2\text{O}_5)$   
 128 and  $\phi(\text{ClNO}_2)$  in smoke. The analysis utilizes aircraft observations from the 2019 Fire Influence  
 129 on Regional to Global Environments and Air Quality (FIREX-AQ) campaign [Warneke *et al.*,  
 130 2023] and the 2017–2018 Atmospheric Tomography mission (ATom) [Thompson *et al.*, 2022].  
 131 We derive  $\gamma(\text{N}_2\text{O}_5)$  and  $\phi(\text{ClNO}_2)$  for montane and agricultural smoke in the troposphere and a

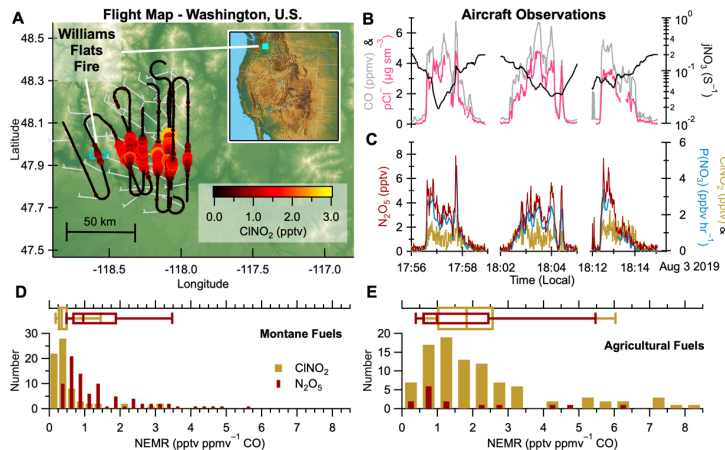
133 PyroCB injection of smoke to the upper troposphere from FIREX-AQ. We derive  $\gamma(\text{N}_2\text{O}_5)$  for  
 134 stratospheric BB-influenced aerosol from ATom. Derived  $\text{N}_2\text{O}_5$  uptake coefficients are  
 135 considerably lower than current model parameterizations. Halogen activation through  $\text{ClNO}_2$   
 136 from  $\text{NO}_x$  and particulate chloride ( $\text{pCl}^-$ ) is prevalent in low altitudes and possible, yet  
 137 unquantified, at high altitude.

## 138 2 Results and Discussion

### 139 2.1 $\text{ClNO}_2$ and $\text{N}_2\text{O}_5$ Observations

140 Figure 2A shows the flight track of the NASA DC-8 aircraft sampling the Williams Flats  
 141 fire during FIREX-AQ on 3 Aug 2019 colored and sized by observed  $\text{ClNO}_2$ . Both  $\text{N}_2\text{O}_5$  and  
 142  $\text{ClNO}_2$  exhibit clear enhancements despite significant photolysis rates of  $\text{NO}_3$  ( $j\text{NO}_3$ ) (Figure 2B-  
 143 C). These enhancements are associated with CO, a smoke tracer, and rapid ( $>1 \text{ ppbv hr}^{-1}$ )  $\text{NO}_3$   
 144 production,  $P(\text{NO}_3) = k[\text{NO}_2][\text{O}_3]$ , where  $k$  is the bimolecular rate coefficient for reaction of  $\text{NO}_2$   
 145 with  $\text{O}_3$ .

146 Median  $j\text{NO}_3$  at the center of wildfire and agriculture plume transects ( $0.14 \text{ s}^{-1}$  and  $0.19 \text{ s}^{-1}$   
 147 respectively) were 15–30% lower than values outside of plumes ( $0.16$  and  $0.20 \text{ s}^{-1}$   
 148 respectively). In large wildfire plumes  $j\text{NO}_3$  attenuation was a factor of ten or more (Figure 2B  
 149 and C), but small agricultural plumes exhibited no attenuation (Figure S1). Previous analyses of  
 150 FIREX-AQ plumes found that  $\text{NO}_3$  photolysis and reaction with NO are not major  $\text{NO}_3$  loss  
 151 pathways regardless of time of day [Decker *et al.*, 2021a; Decker *et al.*, 2021b]. Rapid  $P(\text{NO}_3)$   
 152 together with large concentrations of highly reactive VOCs and aerosol surface area control  $\text{NO}_3$   
 153 and  $\text{N}_2\text{O}_5$  chemistry. Plumes with measurable daytime  $\text{N}_2\text{O}_5$  provide measures of  $\text{NO}_3$  reactivity  
 154 and  $\text{N}_2\text{O}_5$  heterogeneous uptake for these species that are otherwise important only at night in  
 155 non-fire environments.



157 **Figure 2.** **A.** NASA DC-8 flight tracks colored and sized by  $\text{ClNO}_2$  mixing ratio for the Williams  
 158 Flats fire plume on Aug 3. The inset map shows the approximate location of sampling in  
 159 Washington State. **B.** Observations of  $\text{CO}$  (grey),  $\text{pCl}^-$  (pink), and  $j\text{NO}_3$  (black) and **C.**  $\text{N}_2\text{O}_5$   
 160 (red),  $\text{ClNO}_2$  (yellow) and  $\text{P}(\text{NO}_3)$  (blue) for a subset of crosswind plume transects. **D & E.**  
 161 Histogram of  $\text{N}_2\text{O}_5$  and  $\text{ClNO}_2$  NEMRs from all montane (D) and agricultural (E) fires. Box  
 162 plots show 10<sup>th</sup>, 25<sup>th</sup>, 50<sup>th</sup>, 75<sup>th</sup>, and 90<sup>th</sup> percentiles.

The Normalized Excess Mixing Ratio (NEMR) measures the above background enhancements of a compound  $x$  relative to the smoke tracer CO (Table S2 and Figure S2-S4). The median  $\text{N}_2\text{O}_5$  NEMR was 1.0 pptv  $\text{ppmv}^{-1}$  CO for both agricultural and montane fire groups (Figure 2D and E). The  $\text{ClNO}_2$  NEMRs, by contrast, differ by a factor of  $\sim 6$  between montane ( $0.3 \text{ pptv ppmv}^{-1}$ ) and agricultural ( $1.8 \text{ pptv ppmv}^{-1}$ ) fuels. Agricultural and grass burning emits more  $\text{Cl}^-$  per kg of fuel burned (emission factor) when compared to temperate and boreal forest burning [Akagi *et al.*, 2011; Liu *et al.*, 2016; May *et al.*, 2014]. Despite considerable variability, the greater median  $\text{ClNO}_2$  NEMR for agricultural fires is consistent with the observed differences in particulate chloride ( $\text{pCl}^-$ ). DC-8 and Twin Otter observations of the above background  $\text{pCl}^-$  show that agricultural and grass smoke contains roughly  $16\times$  more  $\text{pCl}^-$  by mass than montane smoke (Text S2 and Figure S5).

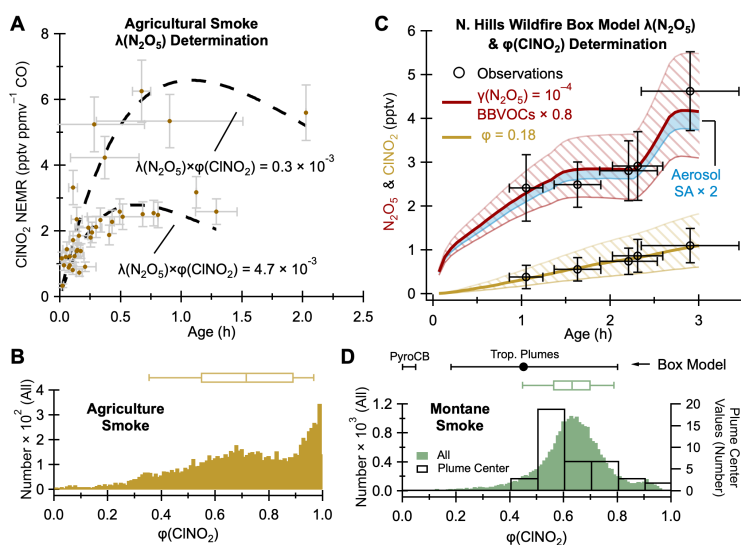
## 2.2 Montane and Agricultural Smoke

To derive  $\gamma(\text{N}_2\text{O}_5)$  from agricultural smoke, we use the calculated NEMR of  $\text{ClNO}_2$  as a function of the physical plume age shown in Figure 3A. We combine the calculated  $\text{ClNO}_2$  NEMRs with the relationship between  $\gamma(\text{N}_2\text{O}_5)$  and  $\varphi(\text{ClNO}_2)$  below to estimate a  $\gamma(\text{N}_2\text{O}_5)$ .

$$\gamma(\text{N}_2\text{O}_5) = 4 \times \frac{k_{\text{N}_2\text{O}_5}}{c \times SA} \quad (1)$$

$$\varphi(\text{ClNO}_2) = \frac{k_{\text{ClNO}_2}}{k_{\text{N}_2\text{O}_5}} \quad (2)$$

Here  $c$  is the mean molecular speed of  $\text{N}_2\text{O}_5$  and  $SA$  is the aerosol surface area density. Data are arbitrarily separated into low and high NEMR groups. The biexponential fit represents first-order formation ( $k_{\text{ClNO}_2}$ ) and photolytic loss ( $j_{\text{ClNO}_2}$ ) of  $\text{ClNO}_2$ . Constraining the fit to an observed median photolysis rate of  $j_{\text{ClNO}_2} = 3.3 \times 10^{-4} \text{ s}^{-1}$  (Figure S6A) we find  $k_{\text{ClNO}_2} = 2.0\text{--}5.8 \times 10^{-4} \text{ s}^{-1}$ . Aerosol surface area can vary widely across a plume transect and therefore we chose a range ( $2\text{--}11 \times 10^3 \mu\text{m}^2 \text{ cm}^{-3}$ ) of observed SA representative of most observations in Figure 3A (Figure S6B) and present a sensitivity analysis to this choice in Figure S6C. Finally, we use a median observed temperature of 296 K to find  $\gamma(\text{N}_2\text{O}_5) \times \varphi(\text{ClNO}_2) = 0.3\text{--}4.7 \times 10^{-3}$ .



189 **Figure 3. A.** Agricultural fire ClNO<sub>2</sub> NEMRs vs. plume age. Dashed lines show biexponential  
 190 fits (see text). **B.** Parametrized  $\phi(ClNO_2)$  of agricultural smoke. **C.** Box model results (lines)  
 191 compared to observations (markers) of N<sub>2</sub>O<sub>5</sub> and ClNO<sub>2</sub> from the July 29 North Hills smoke  
 192 plume with  $\gamma(N_2O_5) = 10^{-4}$ . The hashed area shows changes to VOCs (N<sub>2</sub>O<sub>5</sub>) or yield (ClNO<sub>2</sub>)  
 193 that encompass observational uncertainty. Transparent blue area shows sensitivity to a factor of 2  
 194 increase in aerosol surface area. The apparent discontinuity of N<sub>2</sub>O<sub>5</sub> in the model is due to a  
 195 reduction in the photolysis rate at sunset (2.5 h of age). **D.** Parameterized  $\phi(ClNO_2)$  for montane  
 196 smoke (filled bars) and transect center observations used in the box model (empty bars). Box  
 197 model derived  $\phi(ClNO_2)$  is shown as horizontal ranges in black. The black marker indicates the  
 198 average of the five modeled plumes sampled in the lower troposphere. The range on the model-  
 199 derived  $\phi(ClNO_2)$  shows the range of the five modeled plumes. Note that within observation  
 200 uncertainty the full range is 0-1

201 To estimate  $\phi(ClNO_2)$  we use a laboratory-based parameterization based on observed  
 202 pCl<sup>-</sup> and calculated liquid water content (LWC), hereafter referred to as parameterized  $\phi(ClNO_2)$   
 203 (section 2.2, S1.4). Figure 3B shows parameterized  $\phi(ClNO_2)$  for all 1 Hz agriculture smoke  
 204 observations, with median  $\phi(ClNO_2)$  of 0.72. When considering only observations in Figure 2A,  
 205 used to determine  $\gamma(N_2O_5)$ , the median is 0.77. Previous field comparisons have shown that  
 206 parameterized  $\phi(ClNO_2)$  is likely an upper limit [McDuffie *et al.*, 2018b], and therefore the  
 207 derived  $\gamma(N_2O_5)$  is a lower limit range of  $0.2\text{--}3.6 \times 10^{-3}$ .

208 Montane smoke plumes included several cross-wind transects downwind, which allows  
 209 for  $\gamma(N_2O_5)$  and  $\phi(ClNO_2)$  determination in individual plumes using a constrained 0-D chemical  
 210 box model [Decker *et al.*, 2021a]. Model input values of  $\gamma(N_2O_5)$  were varied between  $10^{-4}$  and  
 211  $10^{-1}$  to minimize the difference between the model and observations of N<sub>2</sub>O<sub>5</sub>. The modeled N<sub>2</sub>O<sub>5</sub>  
 212 is sensitive to NO<sub>3</sub> loss to reactions with VOCs. The model uses VOC emissions from laboratory  
 213 burn emissions inventories, and these are also varied to improve the agreement between modeled  
 214 and observed N<sub>2</sub>O<sub>5</sub>. A comparison of modeled and observed VOCs shows that the majority of  
 215 the observation-model comparisons remain within the observation uncertainty. Lastly,  $\phi(ClNO_2)$   
 216 is varied between 0 and 1. Figures S7-S12 show complete model and observation comparisons.

217 Figure 3C shows a representative model to observation comparison for N<sub>2</sub>O<sub>5</sub> and ClNO<sub>2</sub>.  
 218 In all model runs, a  $\gamma(N_2O_5)$  of  $10^{-4}$  (one order of magnitude precision, see Figure S7) best  
 219 reproduces N<sub>2</sub>O<sub>5</sub> observations. In these five cases, values of  $\gamma(N_2O_5) \geq 10^{-3}$  cannot recreate the  
 220 N<sub>2</sub>O<sub>5</sub> observations without near or complete removal of VOCs, and values of  $\gamma(N_2O_5) < 10^{-4}$   
 221 require  $\phi(ClNO_2) > 1$  to reproduce ClNO<sub>2</sub>.

222 The box model derived  $\phi(ClNO_2)$  ranges from 0.18–0.80 but spans the entire 0-1 range  
 223 when considering the ClNO<sub>2</sub> observational uncertainty (Figure S13). The average model-derived  
 224  $\phi(ClNO_2)$  is 0.45 (Figure 3D, black marker). The average of transect-center-parameterized  
 225  $\phi(ClNO_2)$  is 0.65, similar to the average of all parameterized  $\phi(ClNO_2)$  of 0.62. Parameterized  
 226  $\phi(ClNO_2)$  exceeds the box model, similar to previous field derivations [McDuffie *et al.*, 2018b],  
 227 although >90% of parameterized  $\phi(ClNO_2)$  lies within the box model derived range (Figure 3D).  
 228 Lastly, the derived  $\phi(ClNO_2)$  of agricultural smoke is generally greater than montane smoke,  
 229 consistent with the greater pCl<sup>-</sup> in the former.

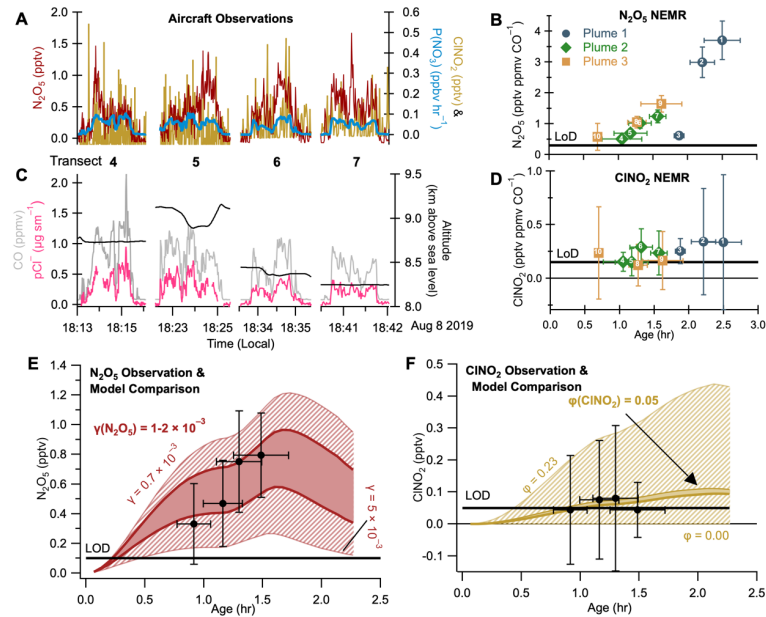
230 Values of  $\gamma(N_2O_5)$  derived here are smaller than values determined in urban air ( $\gamma(N_2O_5)$   
 231  $10^{-3}\text{--}10^{-1}$  [Brown and Stutz, 2012; McDuffie *et al.*, 2018a] and comparable to or lower than a  
 232 limited number of laboratory studies. A chamber study of pyrogenic aerosol for a wire grass fuel

(2.8–6 ± 0.6 × 10<sup>-3</sup>) and a long leaf pine needle fuel (2.5–3.2 ± 0.4 × 10<sup>-3</sup>) [Goldberger *et al.*, 2019] are similar to our agricultural fuels result. A flow-tube study of pyrogenic aerosol identified an increase of  $\gamma(\text{N}_2\text{O}_5)$  for high-chloride-containing BB fuels at relative humidity (RH) >80% [Jahrl *et al.*, 2021]. This is similar to the average RH (70%) for the agricultural smoke plumes here (Figure S14) and consistent with the observation of greater pCl<sup>-</sup> (Figure S5) and larger  $\gamma(\text{N}_2\text{O}_5)$  values (Figure 3) compared to montane smoke.

### 239 2.3 PyroCB Processed Smoke

The DC-8 sampled a PyroCB event from the Williams Flats fire on August 8 that reached 6–10 km above sea level, or 5.6 to 1.6 km below the mean tropopause height. We separate our analysis by plume number and transect number as defined by [Peterson *et al.*, 2022].

Observed P(NO<sub>3</sub>) and N<sub>2</sub>O<sub>5</sub> (Figure 4A) demonstrate the potential for heterogeneous chemistry in the PyroCB injection to the upper atmosphere. Calculated N<sub>2</sub>O<sub>5</sub> NEMR increases with calculated physical plume age when separated by plume number (Figure 4B). Enhancement of pCl<sup>-</sup> (Figure 4C) demonstrates the potential for ClNO<sub>2</sub> production. However, observations of ClNO<sub>2</sub> remained at or below the 1Hz I<sup>-</sup>-CIMS detection limit of 0.05 pptv in Figure 4A and D, limiting the ability to quantify its production. Figure S15 shows that the ClNO<sub>2</sub> signal within all PyroCB smoke observations (average ± 1- $\sigma$  of 0.03 ± 0.10 pptv) is statistically significantly greater ( $p<0.001$ ) than signal outside of the plume (average ± 1- $\sigma$  of 0.02 ± 0.06 pptv), but the data do not allow quantification of the amount of ClNO<sub>2</sub> within the PyroCB.



252

**Figure 4.** NASA DC-8 observations in a PyroCB. Panels A and B show plume 2 observations only (transects 4–7). **A & C.** Observations of N<sub>2</sub>O<sub>5</sub> (red), ClNO<sub>2</sub> (yellow) and P(NO<sub>3</sub>) (blue), CO (grey), pCl<sup>-</sup> (pink), and jNO<sub>3</sub> (black). **B & D.** NEMRs of N<sub>2</sub>O<sub>5</sub> and ClNO<sub>2</sub>. Markers and colors indicate the plume number, and white numbers indicate the transect number. The thick black line indicates the limit of detection (LoD). **E.** Transect center observations of N<sub>2</sub>O<sub>5</sub> (black) for plume 2 compared to the model N<sub>2</sub>O<sub>5</sub> for a range ( $7 \times 10^{-4}$ – $5 \times 10^{-3}$ ) of  $\gamma(\text{N}_2\text{O}_5)$ . **F.** Transect center observations of ClNO<sub>2</sub> (black) for plume 2 compared to the model-derived ClNO<sub>2</sub>. Solid color is

260 the result of a  $\phi(\text{ClNO}_2) = 0.05$  and a  $\gamma(\text{N}_2\text{O}_5) = 1\text{--}2 \times 10^{-3}$  and the hashed area shows a range of  
 261 possible  $\phi(\text{ClNO}_2)$ .

262 Aerosol data are unavailable for plume 3, and plume 1 did not have sufficient semi-  
 263 Lagrangian crosswind transects required to constrain the model. Therefore, the box model is  
 264 used to derive  $\gamma(\text{N}_2\text{O}_5)$  and to place an upper limit on  $\phi(\text{ClNO}_2)$  for plume 2 only. The model  
 265 derived  $\gamma(\text{N}_2\text{O}_5) = 0.7\text{--}5.0 \times 10^{-3}$  (Figure 4E), which is a factor of  $7\text{--}50 \times$  greater than the  
 266  $\gamma(\text{N}_2\text{O}_5)$  values from plumes produced by the same fire but sampled in the lower troposphere.

267 The model predicts  $\phi(\text{ClNO}_2) < 0.05$  to match observations at or below the detection  
 268 limit (or 0.05 at the LoD), although  $\phi(\text{ClNO}_2)$  may be up to 0.23 within the  $1\sigma$  determined  
 269  $\text{ClNO}_2$  measurement uncertainty ( $15\% + 0.05$  pptv). The average parameterized  $\phi(\text{ClNO}_2)$  (0.53)  
 270 is also lower than tropospheric smoke from the same fire (Figure S16) as a result of increased  
 271 calculated liquid water fraction (LWF, Figure S17) in the PyroCB. The presence of sufficient  
 272  $\text{pCl}^-$  for average parameterized  $\phi(\text{ClNO}_2) > 0.5$  suggests that  $\text{ClNO}_2$  production may occur in  
 273 PyroCB transported smoke, even if it was observed only at the detection limit in this daytime  
 274 flight.

## 275 2.4 Aged UTLS pyrogenic aerosol

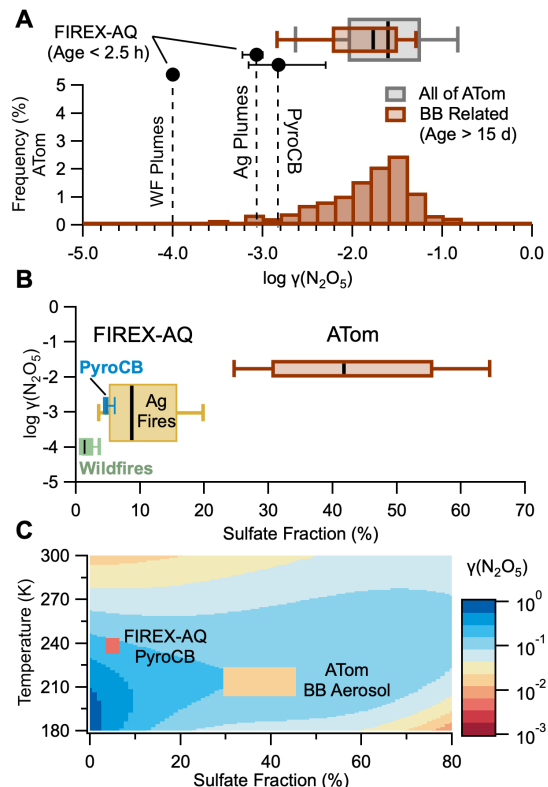
276 Observations from the ATom campaign provide  $\text{N}_2\text{O}_5$  observations in the UTLS. We  
 277 separate our analysis into background and pyrogenic-influenced (defined as  $>75\%$  of aerosol  
 278 number concentration containing pyrogenic markers, see SI). The pyrogenic aerosol is estimated  
 279 to have a physical age of  $>15$  days. A diel model built on the framework of previous model  
 280 determinations of  $\gamma(\text{N}_2\text{O}_5)$  in the lower troposphere [McDuffie *et al.*, 2018a] is constrained to  
 281 chemical observations (see SI).

282 The diel model predicts the median  $\gamma(\text{N}_2\text{O}_5)$  from all background UTLS samples  
 283 ( $N=3483$ ) is  $2.9 \times 10^{-2}$  as shown in Figure 5A (grey box and whiskers). The pyrogenic-  
 284 influenced aerosol has a median  $\gamma(\text{N}_2\text{O}_5)$  of  $1.7 \times 10^{-2}$  (Figure 4A, brown) which is significantly  
 285 different ( $p < 0.001$ ) than the background aerosol. We also consider a smaller subset of  
 286 pyrogenic influenced aerosol from ATom previously identified by [Katich *et al.*, 2023] to have  
 287 originated from PyroCB influence. The resulting  $\gamma(\text{N}_2\text{O}_5)$  of  $2.5 \times 10^{-2}$  is significantly ( $p = 0.01$ )  
 288 less than background UTLS aerosol, and greater than our selection of pyrogenic influenced  
 289 aerosol (Figure S18). Overall, the model predicts that pyrogenic aerosol has a lower rate of  $\text{N}_2\text{O}_5$   
 290 uptake than background UTLS aerosol, yet substantially greater than pyrogenic aerosol in young  
 291 tropospheric plumes.

292 The differences in  $\gamma(\text{N}_2\text{O}_5)$  across agricultural, montane, PyroCb, and UTLS data are  
 293 associated with increased aerosol sulfate fraction. Figure 5B shows a positive trend in  
 294  $\log(\gamma(\text{N}_2\text{O}_5))$  as a function of aerosol sulfate fraction distribution. The median sulfate fraction  
 295 was 1, 5, 9 and 42% in recently-emitted montane, PyroCB, agricultural and aged stratospheric  
 296 BB aerosol, respectively. Laboratory studies suggest organic coatings inhibit  $\text{N}_2\text{O}_5$  uptake, which  
 297 is generally dependent on the organic layer composition and relative humidity [Gaston *et al.*,  
 298 2014]. Conversely, increasing sulfate fraction is associated with increasing  $\gamma(\text{N}_2\text{O}_5)$  [McDuffie *et*  
 299 *al.*, 2018a]. Sulfate in tropospheric BB plumes arises from oxidation of pyrogenic  $\text{SO}_2$  [Rickly *et*  
 300 *al.*, 2022], whereas pyrogenic-influenced aerosol in the UTLS takes up sulfate during aging.

301 Current stratospheric models of BB impacts on stratospheric processes [Strahan *et al.*,  
 302 2022; Yu *et al.*, 2021] use a  $\gamma(\text{N}_2\text{O}_5)$  based on aqueous sulfate aerosol. Figure 5C shows  $\gamma(\text{N}_2\text{O}_5)$

values from BB influenced aerosol are a factor of 10–100 lower than pure aqueous sulfate particles [Burkholder *et al.*, 2020]. BB particles are expected to condense organics from low-volatility VOC oxidation products [Palm *et al.*, 2020], forming organic layers that may reduce  $\gamma(N_2O_5)$ . Evidence of organic markers on stratospheric aerosol was found in some studies of stratospheric BB aerosol [Bernath *et al.*, 2022; Katich *et al.*, 2023], and BB aerosol markers are used here, by definition, to separate BB aerosol from background aerosol.



309 **Figure 5. A.** Comparison of the model-derived  $\gamma(N_2O_5)$  from FIREX-AQ and ATom. Markers show FIREX-AQ results, and the histograms show ATom BB-related  $\gamma(N_2O_5)$ . The box and whisker plots show the ATom BB-related (brown) and all of the ATom (grey) results from the UTLS. **B.** Log  $\gamma(N_2O_5)$  vs aerosol sulfate fraction for FIREX-AQ and ATom. **C.**  $\gamma(N_2O_5)$  parametrization from [Burkholder *et al.*, 2020] for aqueous sulfate particles used in stratospheric models compared to results from this work. Marker size represents the interquartile range of temperature and sulfate fraction in this work.

310 These results indicate  $\gamma(N_2O_5)$  values increase for BB particles transported from the  
 311 troposphere into the UTLS, but never reach values used in stratospheric models. Injection of the  
 312 chloride-containing aerosol observed in montane smoke or repartitioning of gas phase HCl to  
 313 particulate organics or reduced nitrogen [Solomon *et al.*, 2023] may result in a non-zero  $ClNO_2$   
 314 yield, thus introducing chlorine activation pathways currently not considered. Observations  
 315 presented here cannot quantify  $ClNO_2$  production on BB particles transported through a PyroCB  
 316 but demonstrate potential for this process. Observations of diffuse BB influenced particles in the  
 317 UTLS from ATom do not have reliable  $ClNO_2$  measurements, such that we are unable to assess  
 318  $ClNO_2$  production on aged, dilute UTLS BB influenced particles. Concentrated BB plumes  
 319 transported to the stratosphere through PyroCB events, such as the 2020 Australian fires, should  
 320

327 have heterogeneous chemistry similar to that observed here. Recent analysis of high-altitude  
328 aircraft data suggests a ubiquitous influence of such events on stratospheric aerosol composition  
329 [Katich *et al.*, 2023].

### 330 **3 Conclusions**

331 Uptake coefficients for N<sub>2</sub>O<sub>5</sub> determined from in situ observations are lower on BB  
332 aerosol than current model parameterizations. Figure 1 illustrates the observed trends in uptake  
333 coefficients from the lower to the upper atmosphere. The  $\gamma(N_2O_5)$  on dilute smoke-impacted  
334 particles derived in this study is already lower than model parameterizations but likely represents  
335 an upper limit for more concentrated smoke such as the 2020 Australian wildfires. We therefore  
336 suggest that models of the smoke impact to the UTLS will require revised parameterizations with  
337 reduced uptake coefficients.

338 Second [Solomon *et al.*, 2023] show that chloride uptake by the organic phase of smoke  
339 aerosol increases heterogeneous reaction rates of halogen-containing species, thereby activating  
340 chlorine radicals that participate in ozone destruction cycles. Our results demonstrate that N<sub>2</sub>O<sub>5</sub>  
341 uptake on chloride-containing smoke particles produces ClNO<sub>2</sub> in the lower atmosphere and has  
342 the potential to do so in the upper atmosphere, particularly with increased chloride partitioning to  
343 the aerosol phase. We suggest that ClNO<sub>2</sub> formation from N<sub>2</sub>O<sub>5</sub> uptake on smoke particles  
344 injected into the stratosphere during large PyroCB events may be a component of smoke-induced  
345 halogen activation cycles that influence stratospheric ozone.

### 346 **Acknowledgments**

347 We thank Charles A. Brock for particle sizing data from ATom. We thank William H.  
348 Brune and Alexander B. Thamnes for OH/HO<sub>2</sub> data from ATom. We thank Daniel M. Murphy for  
349 PALMS particle type data from ATom. ZCJD, GAN, KA, IB, PCJ, MMC, DAD, AF, JLJ, DP,  
350 JP, PR, MAR, CRT, CW, and CCW, were supported by the NOAA cooperative agreement  
351 NA17OAR4320101. PCJ, HG, BAN, DP, DAD, and JLJ acknowledge support from NASA  
352 Earth Sciences Division (grant nos. NNX15AH33A, 80NSSC18K0630 and 80NSSC21K1451).  
353 C.D.F., B.B.P., and J.A.T. acknowledge support from the NOAA OAR Climate Program Office  
354 (grant no. NA17OAR4310012) CDF acknowledges support from the Future Investigators in  
355 NASA Earth and Space Science and Technology (FINESST) Grant Number 80NSSC20K1612.  
356 SRH and KU acknowledge support from NASA Earth Sciences Division (grant nos.  
357 80NSSC18K0638 and NNX15AG71A). Participation in ATom Mission flights by G.P.S.,  
358 K.D.F., and D.M.M. was supported by NOAA climate funding (no. NNH15AB12I).

### 359 **Data Availability Statement**

360 The aircraft data used in the study are publicly available at [https://www-](https://www-air.larc.nasa.gov/missions/firex-aq/)  
361 [air.larc.nasa.gov/missions/firex-aq/](https://www-air.larc.nasa.gov/missions/firex-aq/).

363

364

365 **References**

- 366 Ahern, A. T., L. Goldberger, L. Jahl, J. Thornton, and R. C. Sullivan (2018), Production of N<sub>2</sub>O<sub>5</sub>  
 367 and ClNO<sub>2</sub> through Nocturnal Processing of Biomass-Burning Aerosol, *Environmental*  
 368 *Science & Technology*, 52(2), 550-559, 10.1021/acs.est.7b04386.
- 369 Akagi, S. K., R. J. Yokelson, C. Wiedinmyer, M. J. Alvarado, J. S. Reid, T. Karl, J. D. Crounse,  
 370 and P. O. Wennberg (2011), Emission factors for open and domestic biomass burning for  
 371 use in atmospheric models, *Atmos. Chem. Phys.*, 11(9), 4039-4072, 10.5194/acp-11-  
 372 4039-2011.
- 373 Bernath, P., C. Boone, and J. Crouse (2022), Wildfire smoke destroys stratospheric ozone,  
 374 *Science*, 375(6586), 1292-1295, 10.1126/science.abm5611.
- 375 Bourgeois, I., J. Peischl, J. A. Neuman, S. S. Brown, C. R. Thompson, K. C. Aikin, H. M. Allen,  
 376 H. Angot, E. C. Apel, C. B. Baublitz, J. F. Brewer, P. Campuzano-Jost, R. Commane, J.  
 377 D. Crounse, B. C. Daube, J. P. DiGangi, G. S. Diskin, L. K. Emmons, A. M. Fiore, G. I.  
 378 Gkatzelis, A. Hills, R. S. Hornbrook, L. G. Huey, J. L. Jimenez, M. Kim, F. Lacey, K.  
 379 McKain, L. T. Murray, B. A. Nault, D. D. Parrish, E. Ray, C. Sweeney, D. Tanner, S. C.  
 380 Wofsy, and T. B. Ryerson (2021), Large contribution of biomass burning emissions to  
 381 ozone throughout the global remote troposphere, *Proceedings of the National Academy of*  
 382 *Sciences*, 118(52), e2109628118, 10.1073/pnas.2109628118.
- 383 Brown, S. S., and J. Stutz (2012), Nighttime Radical Observations and Chemistry, *Chem. Soc.*  
 384 *Reviews*, 41, 6405-6447, DOI: 10.1039/c2cs35181a.
- 385 Burkholder, J. B., J. P. D. Abbatt, C. Cappa, T. S. Dibble, C. E. Kolb, V. L. Orkin, D. M.  
 386 Wilmouth, S. P. Sander, J. R. Barker, J. D. Crounse, R. E. Huie, M. J. Kurylo, C. J.  
 387 Percival, and P. H. Wine (2020), *Chemical Kinetics and Photochemical Data for Use in*  
 388 *Atmospheric Studies*, JPL Publication 19-5, Pasadena, CA.
- 389 Decker, Z. C. J., M. A. Robinson, K. C. Barsanti, I. Bourgeois, M. M. Coggon, J. P. DiGangi, G.  
 390 S. Diskin, F. M. Flocke, A. Franchin, C. D. Fredrickson, G. I. Gkatzelis, S. R. Hall, H.  
 391 Halliday, C. D. Holmes, L. G. Huey, Y. R. Lee, J. Lindaas, A. M. Middlebrook, D. D.  
 392 Montzka, R. Moore, J. A. Neuman, J. B. Nowak, B. B. Palm, J. Peischl, F. Piel, P. S.  
 393 Rickly, A. W. Rollins, T. B. Ryerson, R. H. Schwantes, K. Sekimoto, L. Thornhill, J. A.  
 394 Thornton, G. S. Tyndall, K. Ullmann, P. Van Rooy, P. R. Veres, C. Warneke, R. A.  
 395 Washenfelder, A. J. Weinheimer, E. Wiggins, E. Winstead, A. Wisthaler, C. Womack,  
 396 and S. S. Brown (2021a), Nighttime and daytime dark oxidation chemistry in wildfire  
 397 plumes: an observation and model analysis of FIREX-AQ aircraft data, *Atmos. Chem.*  
 398 *Phys.*, 21(21), 16293-16317, 10.5194/acp-21-16293-2021.
- 399 Decker, Z. C. J., S. Wang, I. Bourgeois, P. Campuzano Jost, M. M. Coggon, J. P. DiGangi, G. S.  
 400 S. Diskin, F. M. Flocke, A. Franchin, C. D. Fredrickson, G. I. Gkatzelis, S. R. Hall, H.  
 401 Halliday, K. Hayden, C. D. Holmes, L. G. Huey, J. L. Jimenez, Y. R. Lee, J. Lindaas, A.  
 402 M. Middlebrook, D. D. Montzka, J. A. Neuman, J. B. Nowak, D. Pagonis, B. B. Palm, J.  
 403 Peischl, F. Piel, P. S. Rickly, M. A. Robinson, A. W. Rollins, T. B. Ryerson, K.  
 404 Sekimoto, J. A. Thornton, G. S. Tyndall, K. Ullmann, P. R. Veres, C. Warneke, R. A.  
 405 Washenfelder, A. J. Weinheimer, A. Wisthaler, C. Womack, and S. S. Brown (2021b),  
 406 Novel Analysis to Quantify Plume Crosswind Heterogeneity Applied to Biomass Burning  
 407 Smoke, *Environmental Science & Technology*, 55(23), 15646-15657,  
 408 10.1021/acs.est.1c03803.

- 409 Dentener, F. J., and P. J. Crutzen (1993), Reaction of N<sub>2</sub>O<sub>5</sub> on Tropospheric Aerosols: Impact on  
410 the Global Distributions of NO<sub>x</sub>, O<sub>3</sub>, and OH, *J. Geophys. Res.*, 98(D4), 7149-7163.
- 411 Gaston, C. J., J. A. Thornton, and N. L. Ng (2014), Reactive uptake of N<sub>2</sub>O<sub>5</sub> to internally mixed  
412 inorganic and organic particles: the role of organic carbon oxidation state and inferred  
413 organic phase separations, *Atmos. Chem. Phys.*, 14(11), 5693-5707, 10.5194/acp-14-  
414 5693-2014.
- 415 Goldberger, L. A., L. G. Jahl, J. A. Thornton, and R. C. Sullivan (2019), N<sub>2</sub>O<sub>5</sub> reactive uptake  
416 kinetics and chlorine activation on authentic biomass-burning aerosol, *Environmental  
417 Science: Processes & Impacts*, 21(10), 1684-1698, 10.1039/C9EM00330D.
- 418 Jahl, L. G., B. B. Bowers, L. G. Jahn, J. A. Thornton, and R. C. Sullivan (2021), Response of the  
419 Reaction Probability of N<sub>2</sub>O<sub>5</sub> with Authentic Biomass-Burning Aerosol to High Relative  
420 Humidity, *ACS Earth and Space Chemistry*, 5(10), 2587-2598,  
421 10.1021/acsearthspacechem.1c00227.
- 422 Jones, M. W., J. T. Abatzoglou, S. Veraverbeke, N. Andela, G. Lasslop, M. Forkel, A. J. P.  
423 Smith, C. Burton, R. A. Betts, G. R. van der Werf, S. Sitch, J. G. Canadell, C. Santín, C.  
424 Kolden, S. H. Doerr, and C. Le Quéré (2022), Global and Regional Trends and Drivers of  
425 Fire Under Climate Change, *Reviews of Geophysics*, 60(3), e2020RG000726,  
426 <https://doi.org/10.1029/2020RG000726>.
- 427 Katich, J. M., E. C. Apel, I. Bourgeois, C. A. Brock, T. P. Bui, P. Campuzano-Jost, R.  
428 Commane, B. Daube, M. Dollner, M. Fromm, K. D. Froyd, A. J. Hills, R. S. Hornbrook,  
429 J. L. Jimenez, A. Kupc, K. D. Lamb, K. McKain, F. Moore, D. M. Murphy, B. A. Nault,  
430 J. Peischl, A. E. Perring, D. A. Peterson, E. A. Ray, K. H. Rosenlof, T. Ryerson, G. P.  
431 Schill, J. C. Schroder, B. Weinzierl, C. Thompson, C. J. Williamson, S. C. Wofsy, P. Yu,  
432 and J. P. Schwarz (2023), Pyrocumulonimbus affect average stratospheric aerosol  
433 composition, *Science*, 379(6634), 815-820, 10.1126/science.add3101.
- 434 Koss, A. R., K. Sekimoto, J. B. Gilman, V. Selimovic, M. M. Coggon, K. J. Zarzana, B. Yuan,  
435 B. M. Lerner, S. S. Brown, J. L. Jimenez, J. Krechmer, J. M. Roberts, C. Warneke, R. J.  
436 Yokelson, and J. de Gouw (2018), Non-methane organic gas emissions from biomass  
437 burning: identification, quantification, and emission factors from PTR-ToF during the  
438 FIREX 2016 laboratory experiment, *Atmos. Chem. Phys.*, 18(5), 3299-3319,  
439 10.5194/acp-18-3299-2018.
- 440 Küll, V., M. Riese, X. Tie, T. Wiemert, G. Eidmann, D. Offermann, and G. P. Brasseur (2002),  
441 NO<sub>y</sub> partitioning and aerosol influences in the stratosphere, *J. Geophys. Res.*, 107(D23),  
442 8183, 10.1029/2001jd001246.
- 443 Liu, X., Y. Zhang, L. G. Huey, R. J. Yokelson, Y. Wang, J. L. Jimenez, P. Campuzano-Jost, A. J.  
444 Beyersdorf, D. R. Blake, Y. Choi, J. M. St. Clair, J. D. Crounse, D. A. Day, G. S. Diskin,  
445 A. Fried, S. R. Hall, T. F. Hanisco, L. E. King, S. Meinardi, T. Mikoviny, B. B. Palm, J.  
446 Peischl, A. E. Perring, I. B. Pollack, T. B. Ryerson, G. Sachse, J. P. Schwarz, I. J.  
447 Simpson, D. J. Tanner, K. L. Thornhill, K. Ullmann, R. J. Weber, P. O. Wennberg, A.  
448 Wisthaler, G. M. Wolfe, and L. D. Ziemba (2016), Agricultural fires in the southeastern  
449 U.S. during SEAC4RS: Emissions of trace gases and particles and evolution of ozone,  
450 reactive nitrogen, and organic aerosol, *Journal of Geophysical Research: Atmospheres*,  
451 121(12), 7383-7414, 10.1002/2016JD025040.
- 452 May, A. A., G. R. McMeeking, T. Lee, J. W. Taylor, J. S. Craven, I. Burling, A. P. Sullivan, S.  
453 Akagi, J. L. Collett Jr, M. Flynn, H. Coe, S. P. Urbanski, J. H. Seinfeld, R. J. Yokelson,  
454 and S. M. Kreidenweis (2014), Aerosol emissions from prescribed fires in the United

- 455 States: A synthesis of laboratory and aircraft measurements, *Journal of Geophysical*  
 456 *Research: Atmospheres*, 119(20), 11,826-811,849,  
 457 <https://doi.org/10.1002/2014JD021848>.
- 458 McDuffie, E., E., L. Fibiger Dorothy, P. Dubé William, F. Lopez-Hilfiker, H. Lee Ben, A.  
 459 Thornton Joel, V. Shah, L. Jaeglé, H. Guo, J. Weber Rodney, J. Michael Reeves, J.  
 460 Weinheimer Andrew, C. Schroder Jason, P. Campuzano-Jost, L. Jimenez Jose, E. Dibb  
 461 Jack, P. Veres, C. Ebben, L. Sparks Tamara, J. Wooldridge Paul, C. Cohen Ronald, S.  
 462 Hornbrook Rebecca, C. Apel Eric, T. Campos, R. Hall Samuel, K. Ullmann, and S. S.  
 463 Brown (2018a), Heterogeneous N<sub>2</sub>O<sub>5</sub> Uptake During Winter: Aircraft Measurements  
 464 During the 2015 WINTER Campaign and Critical Evaluation of Current  
 465 Parameterizations, *Journal of Geophysical Research: Atmospheres*, 123(8), 4345-4372,  
 466 10.1002/2018JD028336.
- 467 McDuffie, E. E., D. L. Fibiger, W. P. Dubé, F. Lopez Hilfiker, B. H. Lee, L. Jaeglé, H. Guo, R.  
 468 J. Weber, J. M. Reeves, A. J. Weinheimer, J. C. Schroder, P. Campuzano-Jost, J. L.  
 469 Jimenez, J. E. Dibb, P. Veres, C. Ebben, T. L. Sparks, P. J. Wooldridge, R. C. Cohen, T.  
 470 Campos, S. R. Hall, K. Ullmann, J. M. Roberts, J. A. Thornton, and S. S. Brown (2018b),  
 471 ClNO<sub>2</sub> Yields From Aircraft Measurements During the 2015 WINTER Campaign and  
 472 Critical Evaluation of the Current Parameterization, *Journal of Geophysical Research: Atmospheres*,  
 473 123(22), 12,994-913,015, 10.1029/2018JD029358.
- 474 Palm, B. B., Q. Peng, C. D. Fredrickson, B. H. Lee, L. A. Garofalo, M. A. Pothier, S. M.  
 475 Kreidenweis, D. K. Farmer, R. P. Pokhrel, Y. Shen, S. M. Murphy, W. Permar, L. Hu, T.  
 476 L. Campos, S. R. Hall, K. Ullmann, X. Zhang, F. Flocke, E. V. Fischer, and J. A.  
 477 Thornton (2020), Quantification of organic aerosol and brown carbon evolution in fresh  
 478 wildfire plumes, *Proceedings of the National Academy of Sciences*, 117(47), 29469,  
 479 10.1073/pnas.2012218117.
- 480 Peterson, D. A., M. D. Fromm, R. H. D. McRae, J. R. Campbell, E. J. Hyer, G. Taha, C. P.  
 481 Camacho, G. P. Kablick, C. C. Schmidt, and M. T. DeLand (2021), Australia's Black  
 482 Summer pyrocumulonimbus super outbreak reveals potential for increasingly extreme  
 483 stratospheric smoke events, *npj Climate and Atmospheric Science*, 4(1), 38,  
 484 10.1038/s41612-021-00192-9.
- 485 Peterson, D. A., L. H. Thapa, P. E. Saide, A. J. Soja, E. M. Gargulinski, E. J. Hyer, B. Weinzierl,  
 486 M. Dollner, M. Schöberl, P. P. Papin, S. Kondragunta, C. P. Camacho, C. Ichoku, R. H.  
 487 Moore, J. W. Hair, J. H. Crawford, P. E. Dennison, O. V. Kalashnikova, C. E. Bennese,  
 488 T. P. Bui, J. P. DiGangi, G. S. Diskin, M. A. Fenn, H. S. Halliday, J. Jimenez, J. B.  
 489 Nowak, C. Robinson, K. Sanchez, T. J. Shingler, L. Thornhill, E. B. Wiggins, E.  
 490 Winstead, and C. Xu (2022), Measurements from inside a Thunderstorm Driven by  
 491 Wildfire: The 2019 FIREX-AQ Field Experiment, *Bulletin of the American  
 492 Meteorological Society*, 10.1175/BAMS-D-21-0049.1.
- 493 Ravishankara, A. R. (1997), Heterogeneous and multiphase chemistry in the troposphere,  
 494 *Science*, 276, 1058-1065.
- 495 Rickly, P. S., H. Guo, P. Campuzano-Jost, J. L. Jimenez, G. M. Wolfe, R. Bennett, I. Bourgeois,  
 496 J. D. Crounse, J. E. Dibb, J. P. DiGangi, G. S. Diskin, M. Dollner, E. M. Gargulinski, S.  
 497 R. Hall, H. S. Halliday, T. F. Hanisco, R. A. Hannun, J. Liao, R. Moore, B. A. Nault, J.  
 498 B. Nowak, J. Peischl, C. E. Robinson, T. Ryerson, K. J. Sanchez, M. Schöberl, A. J. Soja,  
 499 J. M. St. Clair, K. L. Thornhill, K. Ullmann, P. O. Wennberg, B. Weinzierl, E. B.  
 500 Wiggins, E. L. Winstead, and A. W. Rollins (2022), Emission factors and evolution of

- 501 SO<sub>2</sub> measured from biomass burning in wildfires and agricultural fires, *Atmos. Chem.*  
502 *Phys.*, 22(23), 15603-15620, 10.5194/acp-22-15603-2022.
- 503 Solomon, S. (1999), Stratospheric ozone depletion: A review of concepts and history, *Reviews of*  
504 *Geophysics*, 37(3), 275-316, 10.1029/1999rg900008.
- 505 Solomon, S., K. Dube, K. Stone, P. Yu, D. Kinnison, B. Toon Owen, E. Strahan Susan, H.  
506 Rosenlof Karen, R. Portmann, S. Davis, W. Randel, P. Bernath, C. Boone, G. Bardeen  
507 Charles, A. Bourassa, D. Zawada, and D. Degenstein (2022), On the stratospheric  
508 chemistry of midlatitude wildfire smoke, *Proceedings of the National Academy of*  
509 *Sciences*, 119(10), e2117325119, 10.1073/pnas.2117325119.
- 510 Solomon, S., K. Stone, P. Yu, D. M. Murphy, D. Kinnison, A. R. Ravishankara, and P. Wang  
511 (2023), Chlorine activation and enhanced ozone depletion induced by wildfire aerosol,  
512 *Nature*, 615(7951), 259-264, 10.1038/s41586-022-05683-0.
- 513 Strahan, S. E., D. Smale, S. Solomon, G. Taha, M. R. Damon, S. D. Steenrod, N. Jones, B. Liley,  
514 R. Querel, and J. Robinson (2022), Unexpected Repartitioning of Stratospheric Inorganic  
515 Chlorine After the 2020 Australian Wildfires, *Geophysical Research Letters*, 49(14),  
516 e2022GL098290, <https://doi.org/10.1029/2022GL098290>.
- 517 Thompson, C. R., S. C. Wofsy, M. J. Prather, P. A. Newman, T. F. Hanisco, T. B. Ryerson, D.  
518 W. Fahey, E. C. Apel, C. A. Brock, W. H. Brune, K. Froyd, J. M. Katich, J. M. Nicely, J.  
519 Peischl, E. Ray, P. R. Veres, S. Wang, H. M. Allen, E. Asher, H. Bian, D. Blake, I.  
520 Bourgeois, J. Budney, T. P. Bui, A. Butler, P. Campuzano-Jost, C. Chang, M. Chin, R.  
521 Commane, G. Correa, J. D. Crounse, B. Daube, J. E. Dibb, J. P. DiGangi, G. S. Diskin,  
522 M. Dollner, J. W. Elkins, A. M. Fiore, C. M. Flynn, H. Guo, S. R. Hall, R. A. Hannun, A.  
523 Hills, E. J. Hintsas, A. Hodzic, R. S. Hornbrook, L. G. Huey, J. L. Jimenez, R. F. Keeling,  
524 M. J. Kim, A. Kupc, F. Lacey, L. R. Lait, J.-F. Lamarque, J. Liu, K. McKain, S.  
525 Meinardi, D. O. Miller, S. A. Montzka, F. L. Moore, E. J. Morgan, D. M. Murphy, L. T.  
526 Murray, B. A. Nault, J. A. Neuman, L. Nguyen, Y. Gonzalez, A. Rollins, K. Rosenlof, M.  
527 Sargent, G. Schill, J. P. Schwarz, J. M. S. Clair, S. D. Steenrod, B. B. Stephens, S. E.  
528 Strahan, S. A. Strode, C. Sweeney, A. B. Thamess, K. Ullmann, N. Wagner, R. Weber, B.  
529 Weinzierl, P. O. Wennberg, C. J. Williamson, G. M. Wolfe, and L. Zeng (2022), The  
530 NASA Atmospheric Tomography (ATom) Mission: Imaging the Chemistry of the Global  
531 Atmosphere, *Bulletin of the American Meteorological Society*, 103(3), E761-E790,  
532 10.1175/BAMS-D-20-0315.1.
- 533 Wang, X., D. J. Jacob, S. D. Eastham, M. P. Sulprizio, L. Zhu, Q. Chen, B. Alexander, T.  
534 Sherwen, M. J. Evans, B. H. Lee, J. D. Haskins, F. D. Lopez-Hilfiker, J. A. Thornton, G.  
535 L. Huey, and H. Liao (2019), The role of chlorine in global tropospheric chemistry,  
536 *Atmos. Chem. Phys.*, 19(6), 3981-4003, 10.5194/acp-19-3981-2019.
- 537 Warneke, C., J. P. Schwarz, J. Dibb, O. Kalashnikova, G. Frost, J. Al-Saad, S. S. Brown, W. A.  
538 Brewer, A. Soja, F. C. Seidel, R. A. Washenfelder, E. B. Wiggins, R. H. Moore, B. E.  
539 Anderson, C. Jordan, T. I. Yacovitch, S. C. Herndon, S. Liu, T. Kuwayama, D. Jaffe, N.  
540 Johnston, V. Selimovic, R. Yokelson, D. M. Giles, B. N. Holben, P. Goloub, I. Popovici,  
541 M. Trainer, A. Kumar, R. B. Pierce, D. Fahey, J. Roberts, E. M. Gargulinski, D. A.  
542 Peterson, X. Ye, L. H. Thapa, P. E. Saide, C. H. Fite, C. D. Holmes, S. Wang, M. M.  
543 Coggon, Z. C. J. Decker, C. E. Stockwell, L. Xu, G. Gkatzelis, K. Aikin, B. Lefer, J.  
544 Kaspari, D. Griffin, L. Zeng, R. Weber, M. Hastings, J. Chai, G. M. Wolfe, T. F.  
545 Hanisco, J. Liao, P. Campuzano Jost, H. Guo, J. L. Jimenez, J. Crawford, and F.-A. Q. S.  
546 T. The (2023), Fire Influence on Regional to Global Environments and Air Quality

- 547 (FIREX-AQ), *Journal of Geophysical Research: Atmospheres*, 128(2), e2022JD037758,  
548 <https://doi.org/10.1029/2022JD037758>.
- 549 Xu, L., D. Crounse John, T. Vasquez Krystal, H. Allen, O. Wennberg Paul, I. Bourgeois, S.  
550 Brown Steven, P. Campuzano-Jost, M. Coggon Matthew, H. Crawford James, P.  
551 DiGangi Joshua, S. Diskin Glenn, A. Fried, M. Gargulinski Emily, B. Gilman Jessica, I.  
552 Gkatzelis Georgios, H. Guo, W. Hair Johnathan, R. Hall Samuel, A. Halliday Hannah, F.  
553 Hanisco Thomas, A. Hannun Reem, D. Holmes Christopher, L. G. Huey, L. Jimenez  
554 Jose, A. Lamplugh, R. Lee Young, J. Liao, J. Lindaas, J. A. Neuman, B. Nowak John, J.  
555 Peischl, A. Peterson David, F. Piel, D. Richter, S. Rickly Pamela, A. Robinson Michael,  
556 W. Rollins Andrew, B. Ryerson Thomas, K. Sekimoto, V. Selimovic, T. Shingler, J. Soja  
557 Amber, M. St. Clair Jason, J. Tanner David, K. Ullmann, R. Veres Patrick, J. Walega, C.  
558 Warneke, A. Washenfelder Rebecca, P. Weibring, A. Wisthaler, M. Wolfe Glenn, C.  
559 Womack Caroline, and J. Yokelson Robert (2021), Ozone chemistry in western U.S.  
560 wildfire plumes, *Science Advances*, 7(50), eabl3648, 10.1126/sciadv.abl3648.
- 561 Yu, P., S. M. Davis, O. B. Toon, R. W. Portmann, C. G. Bardeen, J. E. Barnes, H. Telg, C.  
562 Maloney, and K. H. Rosenlof (2021), Persistent Stratospheric Warming Due to 2019–  
563 2020 Australian Wildfire Smoke, *Geophysical Research Letters*, 48(7), e2021GL092609,  
564 <https://doi.org/10.1029/2021GL092609>.
- 565 Zambri, B., S. Solomon, D. E. Kinnison, M. J. Mills, A. Schmidt, R. R. Neely III, A. E.  
566 Bourassa, D. A. Degenstein, and C. Z. Roth (2019), Modeled and Observed Volcanic  
567 Aerosol Control on Stratospheric NO<sub>y</sub> and Cl<sub>y</sub>, *Journal of Geophysical Research: Atmospheres*,  
568 124(17–18), 10283–10303, 10.1029/2019JD031111.
- 569

Supporting Information for

Airborne Observations Constrain Heterogeneous Nitrogen and Halogen Chemistry on  
Tropospheric and Stratospheric Biomass Burning Aerosol

*Zachary C.J. Decker<sup>1,2,3,a</sup>, Gordon A. Novak<sup>1,2</sup>, Kenneth Aikin<sup>1,2</sup>, Patrick R. Veres<sup>1,b</sup>, J. Andrew Neuman<sup>1,2</sup>, Ilann Bourgeois<sup>1,2,c</sup>, T. Paul Bui<sup>d</sup>, Pedro Campuzano-Jost<sup>2,3</sup>, Matthew M. Coggon<sup>1,2</sup>, Douglas A. Day<sup>2,3</sup>, Joshua P. DiGangi<sup>5</sup>, Glenn S. Diskin<sup>5</sup>, Maximilian Dollner<sup>6</sup>, Alessandro Franchin<sup>1,2,7</sup>, Carley D. Fredrickson<sup>8</sup>, Karl D. Froyd<sup>1,2</sup>, Georgios I. Gkatzelis<sup>1,2,d</sup>, Hongyu Guo<sup>2,3</sup>, Samuel R. Hall<sup>7</sup>, Hannah Halliday<sup>5</sup>, Katherine Hayden<sup>9</sup>, Christopher D. Holmes<sup>9</sup>, Jose L. Jimenez<sup>2,3</sup>, Agnieszka Kupc<sup>1,2,6</sup>, Jakob Lindaas<sup>11</sup>, Ann M. Middlebrook<sup>1</sup>, Richard H. Moore<sup>5</sup>, Benjamin A. Nault<sup>12</sup>, John B. Nowak<sup>5</sup>, Demetrios Pagonis<sup>2,3,e</sup>, Brett B. Palm<sup>8,b</sup>, Jeff Peischl<sup>1,2</sup>, Felix M. Piel<sup>13,14</sup>, Pamela S. Rickly<sup>1,2,f</sup>, Michael A. Robinson<sup>1,2,3</sup>, Andrew W. Rollins<sup>1</sup>, Thomas B. Ryerson<sup>1</sup>, Gregory P. Schill<sup>1</sup>, Kanako Sekimoto<sup>15</sup>, Chelsea R. Thompson<sup>1</sup>, Kenneth L. Thornhill<sup>5,16</sup>, Joel A. Thornton<sup>8</sup>, Kirk Ullmann<sup>7</sup>, Carsten Warneke<sup>1</sup>, Rebecca A. Washenfelder<sup>1,g</sup>, Bernadett Weinzierl<sup>6</sup>, Elizabeth B. Wiggins<sup>5</sup>, Christina J. Williamson<sup>1,2,h,i</sup>, Edward L. Winstead<sup>5,16</sup>, Armin Wisthaler<sup>13,14</sup>, Caroline C. Womack<sup>1,2</sup>, Steven S. Brown<sup>1,3</sup>*

<sup>1</sup>NOAA Chemical Sciences Laboratory (CSL), Boulder, Colorado 80305, USA

<sup>2</sup>Cooperative Institute for Research in Environmental Sciences, University of Colorado Boulder, Boulder, Colorado 80309, USA

<sup>3</sup>Department of Chemistry, University of Colorado Boulder, Boulder, Colorado 80309-0215, USA

<sup>4</sup>NASA Ames Research Center, Moffett Field, CA, USA

<sup>5</sup>NASA Langley Research Center, MS 483, Hampton, VA 23681, USA

<sup>6</sup>Faculty of Physics, Aerosol Physics and Environmental Physics, University of Vienna, Vienna, Austria

<sup>7</sup>Atmospheric Chemistry Observations and Modeling Laboratory, National Center for Atmospheric Research, Boulder, CO 80301, USA

<sup>8</sup>Department of Atmospheric Sciences, University of Washington, Seattle, Washington 98195, United States

<sup>9</sup>Air Quality Research Division (AQRD), Environment and Climate Change Canada, Toronto M3H 5T4, Ontario, Canada

<sup>10</sup>Department of Earth, Ocean, and Atmospheric Science, Florida State University, Tallahassee, FL 32306, USA

<sup>11</sup>Department of Atmospheric Science, Colorado State University, Fort Collins, CO 80523, USA

<sup>12</sup>Center for Aerosol and Cloud Chemistry, Aerodyne Research, Inc., Billerica, MA, USA

<sup>13</sup>Institute for Ion Physics and Applied Physics, University of Innsbruck, 6020 Innsbruck, Austria

<sup>14</sup>Department of Chemistry, University of Oslo, 0315 Oslo, Norway

<sup>15</sup>Graduate School of Nanobioscience, Yokohama City University, Yokohama, Kanagawa, 236-0027, Japan

<sup>16</sup>Science Systems and Applications, Inc. (SSAI), Hampton, VA 23666, USA

<sup>a</sup>Now at Laboratory of Atmospheric Chemistry, Paul Scherrer Institute (PSI), 5232 Villigen, Switzerland

<sup>b</sup>now at National Center for Atmospheric Research, Boulder, CO 80301, USA

<sup>c</sup>now at Université Savoie Mont Blanc, INRAE, CARRTEL, 74200 Thonon-les-Bains, France

<sup>d</sup>Now at Institute of Energy and Climate Research, IEK-8: Troposphere, Forschungszentrum Jülich GmbH, Jülich, Germany

<sup>e</sup>now at Department of Chemistry and Biochemistry, Weber State University, Ogden, UT 84408

<sup>f</sup>now at Colorado Department of Public Health and Environment, 4300 Cherry Creek S Dr, Denver, CO 80246

<sup>g</sup>now at Cooperative Institute for Research in Environmental Sciences, University of Colorado Boulder, Boulder, Co 80309, USA

<sup>h</sup>now at Finnish Meteorological Institute, Erik Palmenin Aukio 1, 00560 Helsinki, Finland

<sup>i</sup>now at Institute for Atmospheric and Earth System Research/Physics, Faculty of Science, University of Helsinki, P.O. Box 64, 00014 Helsinki, Finland

## Contents of this file

Text S1 to S2

Figures S1 to S20

Tables S1 to S3

## Introduction

The supporting information includes text describing the FIREX-AQ and ATom observations as well as additional details about analysis methods such as box models and parameterizations. It further includes a series of supporting figures and captions

## S1 Observations and Models

FIREX-AQ was a large-scale field research campaign focusing on wildfire smoke plumes in the western U.S. and prescribed agricultural burning smoke plumes in the southeastern U.S. during the summer of 2019. We use observations from the NOAA Chemistry Twin Otter and NASA DC-8 aircraft. The NASA Atmospheric Tomography (ATom) mission was a large-scale research campaign focusing on remote tropospheric, UTLS, and stratospheric air [Thompson *et al.*, 2022]. Data here are from September–October 2017 (ATom-3) and April–May 2018 (ATom-4). Table S1 lists instrumentation used in this analysis. In-situ observations from ATom and FIREX-AQ are available as a merged dataset and found in [Wofsy *et al.*, 2018] and [Warneke *et al.*, 2023], respectively. See further details in the SI.

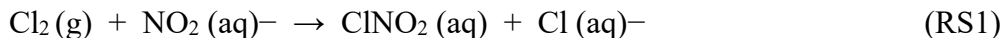
Two models are used: an iterative 0-D box model constrained to crosswind transects of wildfire plumes sampled during FIREX-AQ and an iterative diel model constrained to observations for each parcel of sampled air above an arbitrary elevation cutoff of 6 km during ATom-3 and ATom-4. Calculated  $\phi(\text{ClNO}_2)$  uses a parameterization determined from laboratory experiments [Bertram *et al.*, 2009; Roberts *et al.*, 2009]. See further details below.

### S1.1 FIREX-AQ Observations

From the Twin Otter, we use a commercial cavity ringdown spectrometer (Picarro) for measurements of CO. We also use measurements of non-refractory PM<sub>1</sub> chemical composition from an Aerosol Mass Spectrometer (AMS) [Liggio *et al.*, 2016].

From the DC-8, we use measurements of CO from a tunable diode laser spectrometer when available and from an integrated cavity output spectrometer when unavailable. Measurement of NO is by laser-induced fluorescence (LIF). Measurements of NO<sub>y</sub> and O<sub>3</sub> are provided by a NOAA chemiluminescence (CL) instrument. We use an average measurement of NO<sub>2</sub> from both the NOAA CL instrument and a NOAA cavity-enhanced spectrometer. Measurements of HONO are taken from the NOAA I<sup>-</sup> ToF CIMS. Measurements of VOCs are taken from the NOAA I<sup>-</sup> ToF CIMS [Neuman *et al.*, 2016; Veres *et al.*, 2020], NOAA Proton Transfer Reaction (PTR) MS [Koss *et al.*, 2018], and the University of Innsbruck PTR-MS [Müller *et al.*, 2014]. Aerosol surface area measurements are taken from a laser aerosol spectrometer (LAS, 1 Hz) for aerosol sizes between 0.1 μm and 5 μm. Measurements of non-refractory PM<sub>1</sub> are from the CU HR-AMS, 1-5 Hz [Guo *et al.*, 2021]. Spectrally resolved actinic flux was measured with separate upward and downward-facing actinic flux optics.

The sensitivity of the iodide CIMS to ClNO<sub>2</sub> was determined using methods similar to those described in [Lao *et al.*, 2020]. A Cl<sub>2</sub> mixture (4.167 ppm Cl<sub>2</sub> in 50% RH zero air) was passed through a NaNO<sub>2</sub>-coated PFA tube to dynamically produce ClNO<sub>2</sub>:





The source output was calibrated by a chemiluminescence  $\text{NO}_y$  instrument that measures  $\text{NO}$ ,  $\text{NO}_2$  and  $\text{ClNO}_2$  as  $\text{NO}_y$  [Thaler *et al.*, 2011]. The calibrated  $\text{ClNO}_2$  source was then used for calibration of the iodide CIMS.

An  $\text{N}_2\text{O}_5$  calibration source was produced online via the reaction of  $\text{O}_3$  with  $\text{NO}_2$  to form  $\text{N}_2\text{O}_5$  [Lee *et al.*, 2018]. The output of the calibration source was measured using a cavity ring down instrument for direct detection of  $\text{N}_2\text{O}_5$  [Wagner *et al.*, 2011]. The iodide CIMS was calibrated by comparing the observed signal at  $\text{I}^{\bullet}\text{N}_2\text{O}_5^-$  to the CRDS determined  $\text{N}_2\text{O}_5$  concentration.

$\text{ClNO}_2$  is reported with a precision of 0.1 ppt for 1s data and accuracy of  $15\% + 0.05$  ppt and  $\text{N}_2\text{O}_5$  is reported with a precision of 0.1 ppt for 1s data and accuracy of  $15\% + 2$  ppt. We report the precision as the 1 sigma limit of detection based on signal variability during instrument zeroing in flight. The accuracy of these measurements is quantified as a % based on calibration errors in addition to the error associated with variability instrument background determinations. The latter part of this quantity, 0.05 ppt for  $\text{ClNO}_2$  and 2 ppt for  $\text{N}_2\text{O}_5$ , is defined as the RMS of consecutive background determinations to quantify the error due to linear interpolation between background points. Instrument backgrounds were performed by overflowing the inlet with humidified nitrogen ( $\text{N}_2$ ) for a period of at least 30 seconds every 10 minutes.

### S1.2 ATom Observations

Aerosol sizing and composition data incorporate measurements from the CU HR-AMS [Guo *et al.*, 2021] and bulk aerosol size distributions [Brock *et al.*, 2019]. A Cloud, Aerosol, and Precipitation Spectrometer was used to reject periods of sampling within clouds. Measurements of single particle composition and particle mixing states are from a single-particle laser ionization mass spectrometer (PALMS). The amount of pyrogenic influence is a semi-empirical classification based on the relative peak areas of carbon ( $^{12}\text{C}^+$ ) and potassium ( $^{39}\text{K}^+$ ) [Schill *et al.*, 2020]. Mixing ratios of  $\text{NO}$ ,  $\text{NO}_2$ , and  $\text{O}_3$  were measured with the NOAA CL and measurements of  $\text{OH}$  and  $\text{HO}_2$  were by LIF. Mixing ratio of  $\text{N}_2\text{O}_5$  was measured by the NOAA  $\text{I}^-$ -ToF CIMS (LoD = 0.1 pptv, 1- $\sigma$ , 1Hz, Figure S19) [Veres *et al.*, 2020].

### S1.3 Box Models

The iterative 0-D box model of wildfire plumes is described in detail by Decker et al. [Decker *et al.*, 2021] and discussed briefly here. We model six smoke plumes from three fires sampled on six separate days (Williams Flats, North Hills, and Shady – see Table S3). Box modeling was performed using the Framework for 0-D Atmospheric Modeling (F0AM) [Wolfe *et al.*, 2016] and includes chemistry from the Master Chemical Mechanism (MCM, v3.3.1 via <http://mcm.york.ac.uk>, last access: 23 September 2021) [Bloss *et al.*, 2005], with additional BB mechanisms [Decker *et al.*, 2021]. The model considers only transect-center observations defined as the observations which correspond to the greatest 5% of CO enhancements.

The ATom model builds on the framework of previous model determinations of  $\gamma(\text{N}_2\text{O}_5)$  in the lower troposphere constrained by aircraft measurements [McDuffie *et al.*, 2018a], with changes for the ATom flight scheme and distinct conditions of the UTLS

described here. A run is initiated at the time of local sunset prior to the observation for each 10 s data average and run for a 24-hour diel cycle through to the local sunset after the time of each observation, with diel profiles of photolysis rates and OH concentrations constrained to observations. Mixing ratios of long-lived species, such as H<sub>2</sub>O and aerosol surface area, are held constant over the 24 h period. The model iterates the initial NO<sub>x</sub> until NO is within 20% of observations while NO<sub>2</sub> remains unconstrained. Next,  $k_{N_2O_5}$  is iterated until N<sub>2</sub>O<sub>5</sub> is within 20% of observations and  $\gamma(N_2O_5)$  is calculated from observed temperature and aerosol surface area. We select only data > 6 km that include the required observations for the model above the instrument LoD (77% of data). Of the points modeled, 48% (17,455 determinations) converge on a  $k_{N_2O_5}$  between  $1 \times 10^{-8}$  and 1.

#### S1.4 Parameterization of $\phi(ClNO_2)$

Production of ClNO<sub>2</sub> is considered to proceed by ionization of N<sub>2</sub>O<sub>5</sub> to form NO<sub>2</sub><sup>+</sup> + NO<sub>3</sub><sup>-</sup>. The formation of either HNO<sub>3</sub> or ClNO<sub>2</sub> is based on kinetic competition for the reaction of NO<sub>2</sub><sup>+</sup> with H<sub>2</sub>O or Cl<sup>-</sup>, respectively [Bertram *et al.*, 2009]. Re-formation of N<sub>2</sub>O<sub>5</sub> may also be competitive due to significant concentrations of NO<sub>3</sub><sup>-</sup> relative to Cl<sup>-</sup> (Figure S20). Therefore, this competitive reaction, derived by [McDuffie *et al.*, 2018b] is also included.

$$\Phi(ClNO_2) = \left( k_a \frac{[H_2O]}{[Cl^-]} + k_b \frac{[NO_3^-]}{[Cl^-]} + 1 \right)^{-1} \quad (S1)$$

Here  $k_a$  is taken as  $2.1 \times 10^{-3}$  and  $k_b$  as  $3.4 \times 10^{-2}$  from the work of Bertram, 2009 #31}. Both  $k_a$  and  $k_b$  are ratios of solution phase rate constants and therefore unitless.

We use observations of pCl<sup>-</sup>, particulate NO<sub>3</sub><sup>-</sup> and calculated LWC to calculate  $\phi(ClNO_2)$ . The LWC is estimated as the sum of water associated with individual aerosol species [Guo *et al.*, 2015]. The inorganic part is calculated with ISORROPIA-II thermodynamic model [Fountoukis and Nenes, 2007] in the forward mode. The inorganic aerosol composition is measured by an AMS, HNO<sub>3</sub> (from CIMS), NH<sub>3</sub> from PTR-MS, RH, and temperature. The organic part is estimated based on the organic aerosol mass concentration, density, and hygroscopicity ( $\kappa$ OA) from AMS, in which the  $\kappa$ OA is predicted via the organic aerosol oxygen-to-carbon (O/C) ratio [Rickards *et al.*, 2013].

#### S1.5 Calculation of NEMRs

The NEMRs are calculated by three different methods depending on the observation. NEMRs of pCl<sup>-</sup> are calculated by the linear fit of pCl<sup>-</sup> vs. CO while results with an  $R^2 < 0.3$  are rejected (11% rejected). NEMRs of N<sub>2</sub>O<sub>5</sub> and ClNO<sub>2</sub> in Figure 2 are calculated by integrating the analyte and CO for observations > 3-4× the LoD of the analyte based on a transect-by-transect review. Transects with N<sub>2</sub>O<sub>5</sub> and ClNO<sub>2</sub> below this threshold were rejected (33%). Transect center NEMRs in Figures 3-4 are calculated using transect center observations. The transect center CO value is the average of the top 5 % of CO observations while the transect center analyte value is the analyte observations which align with the top 5 % of CO observations. NEMRs are intended as a metric for the amount of analyte observed relative to the plume size. NEMRs are not equivalent to

emission ratios and are biased by several variables such as plume age, other plume emissions, and fuel type.

#### *Calculation of NEMR values for pCl<sup>-</sup>*

NEMR values of pCl<sup>-</sup> were calculated by linear correlation with CO. All transects for one fire plume were used in the determination of a single NEMR. We use all transects in one determination because we assume pCl<sup>-</sup> is an emission with dilution as the main loss process in the young plumes we consider. The slope of the linear fit is taken to be the NEMR. We only consider plumes whose correlation results in an R<sup>2</sup> > 0.3. For montane fueled plumes this is 14 out of 16 plumes. For grass fueled plumes this is 83 out of 93.

#### *NEMR values of N<sub>2</sub>O<sub>5</sub> and ClNO<sub>2</sub> used in Figure 2*

NEMR values of N<sub>2</sub>O<sub>5</sub> and ClNO<sub>2</sub> used for histograms are calculated by integration of individual plume transects as shown by Equation S2.

$$\frac{\int x dt - \bar{x} \times \Delta t}{\int CO dt - \bar{CO} \times \Delta t} \quad (S2)$$

Here  $x$  is the analyte within the plume,  $x_{bg}$  is the average analyte mixing ratio outside of a plume and  $\Delta t$  is the elapsed time over which the analyte and CO were integrated. The region selection criteria is described further below. The integration method is used, as opposed to a correlation method, because ClNO<sub>2</sub> and N<sub>2</sub>O<sub>5</sub> are not directly emitted. Chemical production of ClNO<sub>2</sub> and N<sub>2</sub>O<sub>5</sub> from precursors other than CO do not necessarily result in a linear correlation.

Note that NEMRs are only calculated for plume transects when measurements of the analyte and CO are present throughout the entirety of the transect and the analyte is roughly 3-4× greater than the LoD. As we demonstrate below, observations rejected for the NEMR calculation are associated with the smallest plumes sampled during FIREX-AQ and therefore the CO is near background and analyte near or at the LoD. Calculating an NEMR for measurements near or below the LoD is uninformative due to the division of small numbers which inflates or gives nonsensical NEMR values.

As shown in Table S2, roughly 39 % and 56 % of all N<sub>2</sub>O<sub>5</sub> and ClNO<sub>2</sub> transects (montane plus agricultural) were used for the NEMR calculation.

#### *NEMRs in montane- and agricultural-fueled fires from FIREX-AQ*

In a case study of N<sub>2</sub>O<sub>5</sub> NEMRs calculated for agricultural fueled-plumes, which had the greatest number of rejected transects due to near or below LoD observations, we show that the calculated median NEMR is consistent with N<sub>2</sub>O<sub>5</sub> observations in all agricultural plumes.

The limited number of available N<sub>2</sub>O<sub>5</sub> NEMR calculations for agricultural plumes is due to the smaller plume size, relative to montane smoke plumes, and larger LoD, relative to ClNO<sub>2</sub>. As shown in Figure S2 below, most of the near or at LoD observations have transect center CO mixing ratios (average of the top 5% of CO within a plume) much less than transects with detectable N<sub>2</sub>O<sub>5</sub>.

#### *Calculation of NEMR values for transect center observations:*

Transect center NEMRs are calculated according to Equation S3 below.

$$\frac{\Delta x}{\Delta CO}$$

(S3)

Here,  $\Delta$  refers to the difference of transect and background observations. Transect center observations are taken to be an average of values corresponding to the top 5% of CO values within a transect: see [Decker *et al.*, 2021]. The  $1-\sigma$  uncertainty of the average is added to measurement uncertainties in quadrature (the square root of the sum of squares) to produce the error bars presented throughout the manuscript. Data below the LoD (including negative values) are included in these calculations without modification.

*Plume transect boundary determination:*

- Smoke region:
- The smoke tracer CO is enhanced above the background ( $> 2-\sigma$ ).
- The smoke is defined (had a clear departure from and return to background levels of CO).
- The transect sampled smoke for more than five continuous seconds (five data points) which corresponds to a plume width of roughly 650 m based on average aircraft speed for the NASA DC-8.
- Background region
- A 15 second period beginning roughly 30 seconds before the transect region (or less if there is less than 30 seconds between transect samples).
- Does not overlap with a smoke region.

## S2 Chloride emissions from montane and agricultural fires

The formation of  $\text{ClNO}_2$  requires particulate chloride ( $\text{pCl}^-$ ). It is known from field and laboratory measurements that agricultural and grass burning emits more  $\text{Cl}^-$  per kg of fuel burned (emission factor) when compared to temperate and boreal forest burning [Ahern *et al.*, 2018; Liu *et al.*, 2016; May *et al.*, 2014]. As we show below, observations from the NASA DC-8 and NOAA Twin Otter aircraft (hereafter DC-8 and Twin Otter) during FIREX-AQ are consistent with these results.

Figure S5A shows a flight track of the DC-8 on 24 July when two fires were sampled in contrasting environments, which offers a case study of contrasting fuels. The Shady fire burned in a mountainous region with timber, tall grass, and logging debris fuels, while the Sheep fire burned sage grass, juniper, and sagebrush in a grassland region (Table S3). As shown in Figure S5B, the Shady and Sheep Fire plumes differ in  $\text{pCl}^-$  by roughly a factor of 10. A linear fit of  $\text{pCl}^-$  vs. CO indicates the above background enhancement of  $\text{pCl}^-$  relative to the smoke tracer CO, also called the normalized excess mixing ratio (NEMR). Observations of  $\text{pCl}^-$  were frequently linearly correlated with CO (89% of plumes had an  $R^2 > 0.3$ ) and above the reported LoD from the Aerosol Mass Spectrometer (AMS) aboard the Twin otter ( $0.09 \mu\text{g sm}^{-3}$ ) and the AMS aboard the DC-8 (median/average  $\pm \sigma$  LoD of  $0.09 / 0.13 \pm 0.09$  for montane-fueled smoke and  $0.19 / 0.19 \pm 0.08$  for agricultural fueled-smoke). Specifically, we observed  $0.6 \mu\text{g sm}^{-3} \text{ ppmv}^{-1}$  CO for the montane fire and  $6.1 \mu\text{g sm}^{-3} \text{ ppmv}^{-1}$  CO for the grass fire. The results from the July 24 case study shown here are consistent with all smoke observations from both the Twin Otter and DC-8 during FIREX-AQ. Median  $\text{pCl}^-$  NEMR for grass and agricultural

fueled smoke was  $9.9 \mu\text{g sm}^{-3}$   $\text{ppmv}^{-1}$  (or  $8.0 \text{ mg g}^{-1}$ ), which is within a factor of two of aircraft-derived NEMR from May et al.'s analysis ( $5.4 \text{ mg g}^{-1}$  for an east coast U.S. grass fire) [May et al., 2014] and within the reported variability of aircraft results by [Liu et al., 2016], but less than the range of laboratory grass burns ( $11.1 - 25.3 \text{ mg g}^{-1}$ ). These results show that agricultural and grass fuels have greater potential for  $\text{ClNO}_2$  formation and activation.

Biomass burning chloride emissions likely occur in the form of  $\text{HCl}$  in the gas phase or as potassium or other salts [May et al., 2014]. We have not carried out thermodynamic modeling of the subsequent chloride partitioning between the gas and aerosol phases. Measurement of gas phase  $\text{HCl}$  was unavailable from the aircraft during FIREX-AQ. Emission factors and NEMRs derived in this work are therefore lower limits. We note, however, that the NEMR for reduced nitrogen ( $\text{NH}_3$ ) greatly exceeds that of chloride [Akagi et al., 2011] and that chloride is soluble in organic aerosol [Solomon et al., 2023]. Therefore, we expect a large fraction of the available chloride to be present as  $\text{pCl}^-$ .

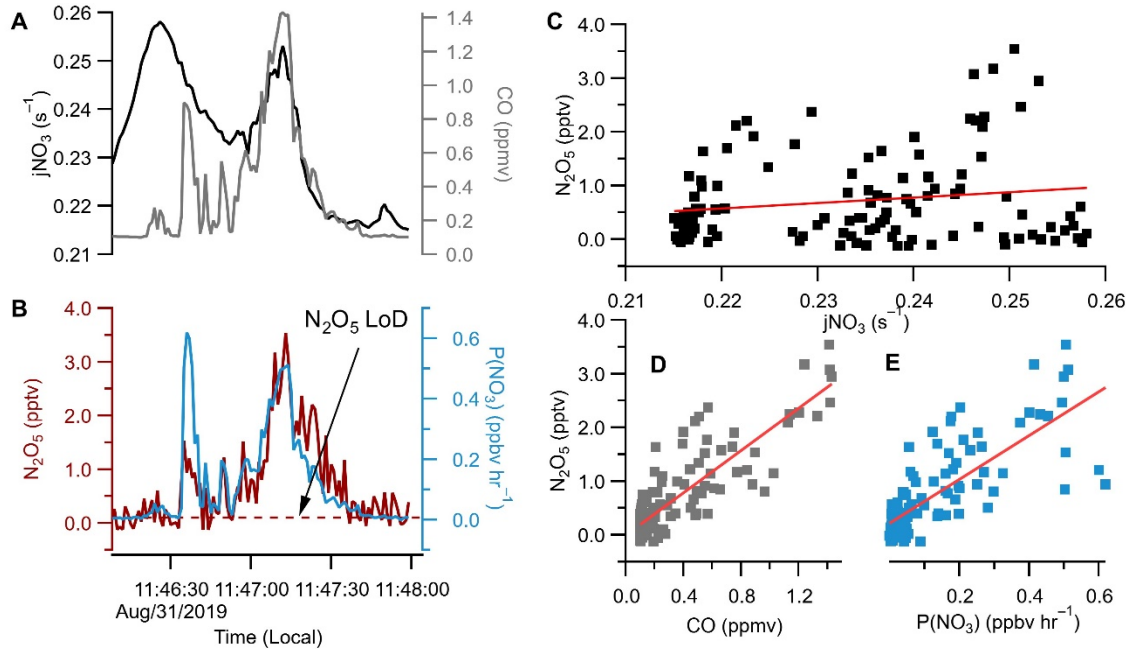


**Figure S1.** observations taken from a crosswind transect of a small agricultural fire plume at mid-day. **(A):** observations of  $j\text{NO}_3$  (left, black) and CO (right, grey). **(B):** observations of  $\text{N}_2\text{O}_5$  (left, red) and  $P(\text{NO}_3)$  (right, blue). **(C):** correlation plot of  $\text{N}_2\text{O}_5$  vs.  $j\text{NO}_3$  with an  $R^2 = 0.03$ . **(D):** correlation plot of  $\text{N}_2\text{O}_5$  vs. CO with an  $R^2 = 0.73$ . **(E):** correlation plot of  $\text{N}_2\text{O}_5$  vs.  $P(\text{NO}_3)$  with an  $R^2 = 0.60$ .

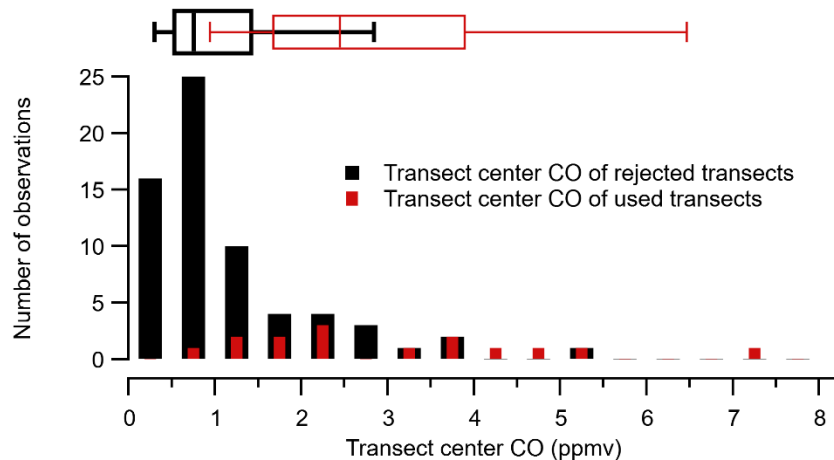


**Figure S2.** Histogram of transect center CO for transects rejected (black) or used (red) (see Table S2) for NEMR calculations. Box plots show 10<sup>th</sup>, 25<sup>th</sup>, 50<sup>th</sup>, 75<sup>th</sup>, and 90<sup>th</sup> percentiles. The median/average  $\pm \sigma$  of observations above the LoD is  $2.4 / 3.0 \pm 1.8$  and for observations below the LoD it is  $0.75 / 1.2 \pm 1.3$ . Assuming an NEMR of  $1.0 \text{ pptv ppmv}^{-1}$  CO (the median result determined in the main text) the expected  $\text{N}_2\text{O}_5$  mixing ratio shows that the majority of  $\text{N}_2\text{O}_5$  is expected to be at or below the LoD (Figure S3) and would be rejected by a 3-4 $\times$  LoD threshold.

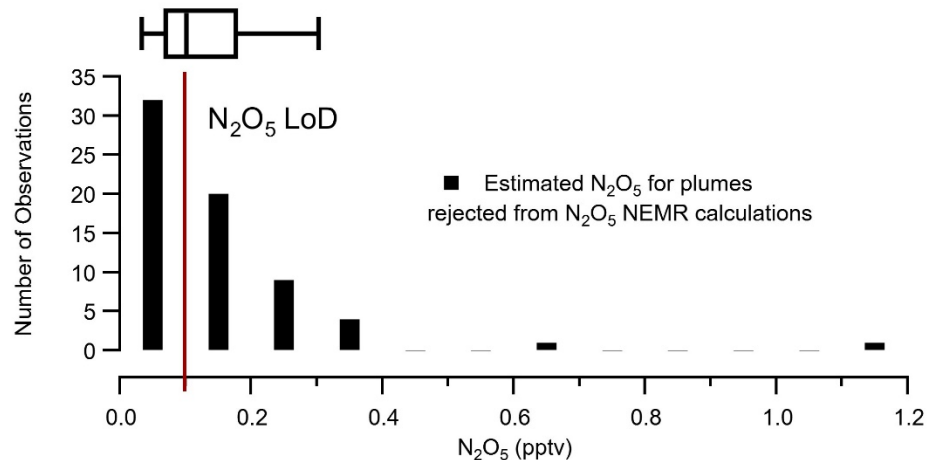


**Figure S3.** Histogram of estimated  $\text{N}_2\text{O}_5$  mixing ratio for transects rejected for NEMR calculations. The estimation is based on the observed CO and an NEMR of 1.0 pptv  $\text{ppmv}^{-1}$  CO as determined in the main text. Box plots show 10<sup>th</sup>, 25<sup>th</sup>, 50<sup>th</sup>, 75<sup>th</sup>, and 90<sup>th</sup> percentiles. The median/average  $\pm \sigma$  of estimated  $\text{N}_2\text{O}_5$  mixing ratio is 0.1 /  $0.2 \pm 0.2$

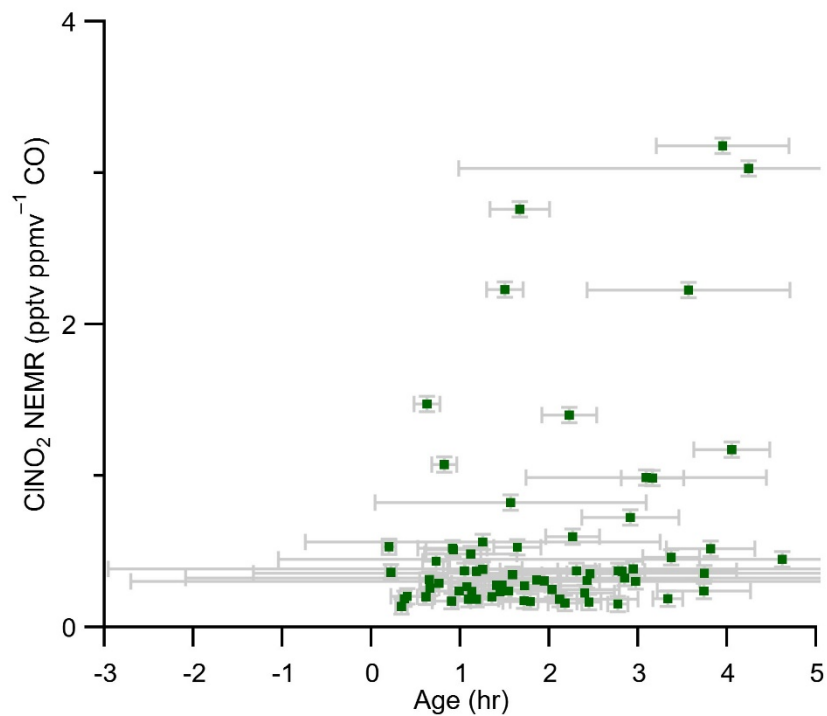


**Figure S4.** Calculated  $\text{ClNO}_2$  NEMRs from montane-fueled fires as a function of average plume age.

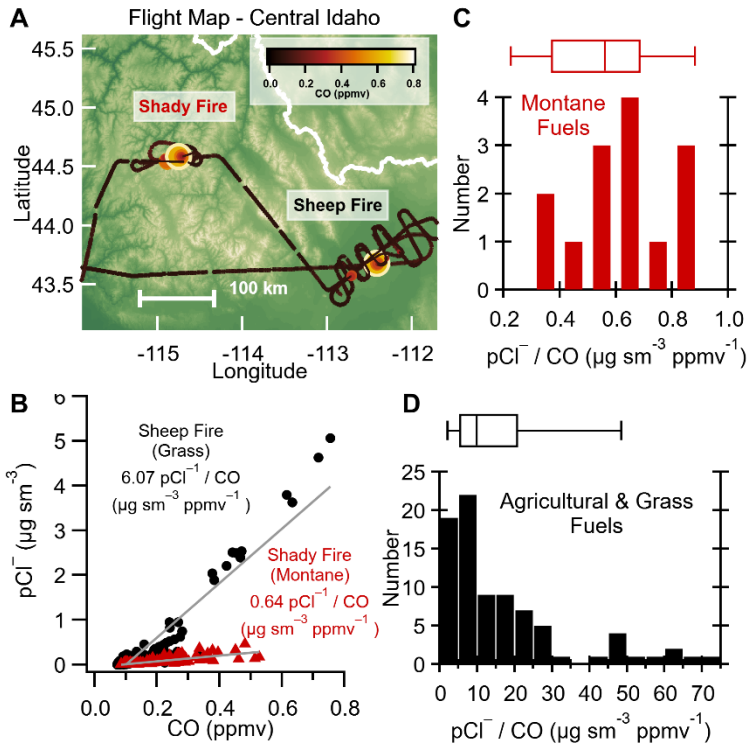


**Figure S5.** (A): flight map (terrain colored by elevation) with the flight path (colored and sized by CO mixing ratio) of the DC-8 sampling the Shady fire plume (red, 17:45–18:15 MDT, including timber, tall grass, and logging debris fuels) and the Sheep fire plume (black, 16:15–16:30 MDT, including sage-grass, juniper, and sagebrush fuels). (B) aircraft observations of  $\text{pCl}^-$  correlated with the CO mixing ratio of the Shady (red,  $R^2 = 0.62$ ) and Sheep (black,  $R^2 = 0.87$ ) fire plumes. (C) histogram with box and whisker plot of normalized excess mixing ratios of  $\text{pCl}^-$  for montane fueled smoke observations taken by the DC-8 and the Twin Otter aircraft in FIREX-AQ. (D) Similar to panel C but for grass and agricultural fuels. Box plots show 10<sup>th</sup>, 25<sup>th</sup>, 50<sup>th</sup>, 75<sup>th</sup>, and 90<sup>th</sup> percentiles. The median NEMR for wildland fuels is  $0.6 \mu\text{g sm}^{-3} \text{ ppmv}^{-1}$  and the average  $\pm 1-\sigma$  is  $0.6 \pm 0.3 \mu\text{g sm}^{-3} \text{ ppmv}^{-1}$ . The median for agricultural fuels is  $9.9 \mu\text{g sm}^{-3} \text{ ppmv}^{-1}$  and the average  $\pm 1-\sigma$  is  $16.6 \pm 17.1 \mu\text{g sm}^{-3} \text{ ppmv}^{-1}$ .

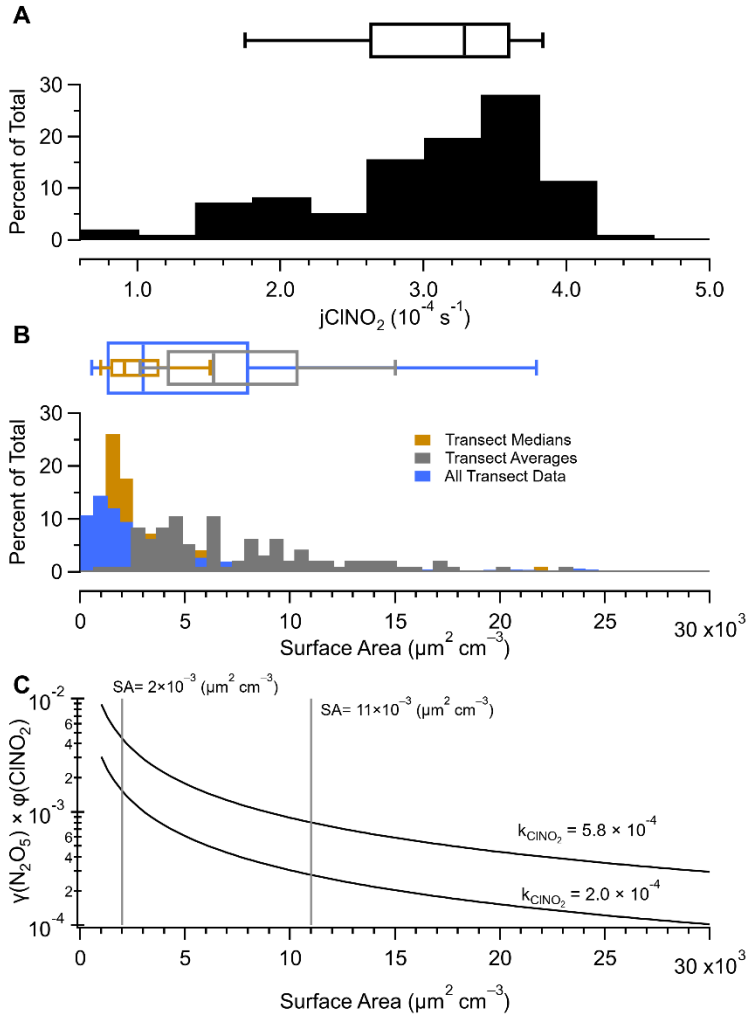


**Figure S6.** (A) Histogram of observed photolysis rates of  $\text{ClNO}_2$  ( $j\text{ClNO}_2$ ) for calculated NEMR in Figure 3A. (B) Histograms of the aerosol surface area in the agricultural-fueled fires sampled by the DC-8 during FIREX-AQ. The transect medians (grey) and averages (brown) represent a median or average of single transects. This is compared to all smoke data (blue), which shows all smoke data. Box and whiskers show results for the 10<sup>th</sup>, 25<sup>th</sup>, 50<sup>th</sup>, 75<sup>th</sup>, and 90<sup>th</sup> percentiles. In (A) and (B) box and whiskers show results for the 10<sup>th</sup>, 25<sup>th</sup>, 50<sup>th</sup>, 75<sup>th</sup>, and 90<sup>th</sup> percentiles. (C) A sensitivity analysis of  $\gamma(\text{N}_2\text{O}_5) \times \varphi(\text{ClNO}_2)$  as a function of aerosol surface area. The region between grey vertical lines represents our best estimate range of  $\gamma(\text{N}_2\text{O}_5) \times \varphi(\text{ClNO}_2)$  based on a range of aerosol surface area (SA) and the observed  $k\text{ClNO}_2$  in Figure 3A.

North Hills July 29 Model Comparison

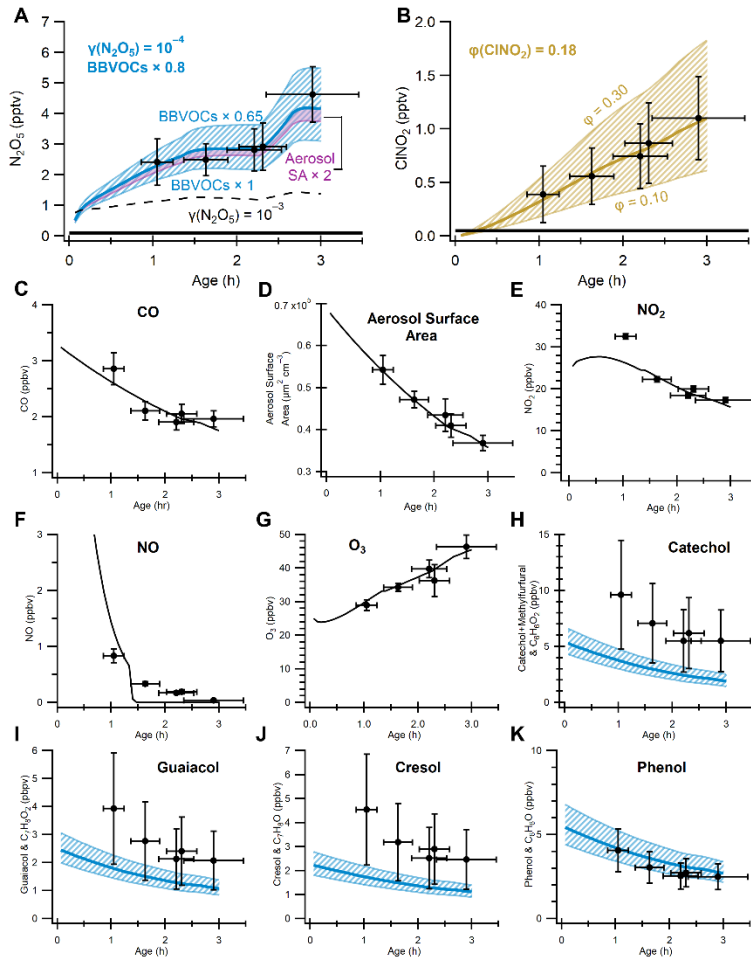


**Figure S7.** Comparison of box model results to observations for the North Hills Fire on July 29. Observations are shown as black markers while model results are shown as solid lines. Vertical error bars include instrument uncertainty and  $1-\sigma$  variability (added in quadrature: the square root of the sum of squares) of the average of the transect center observations (observations aligned with the top 5% of CO). The blue shading in H–K corresponds to model results shown in A.

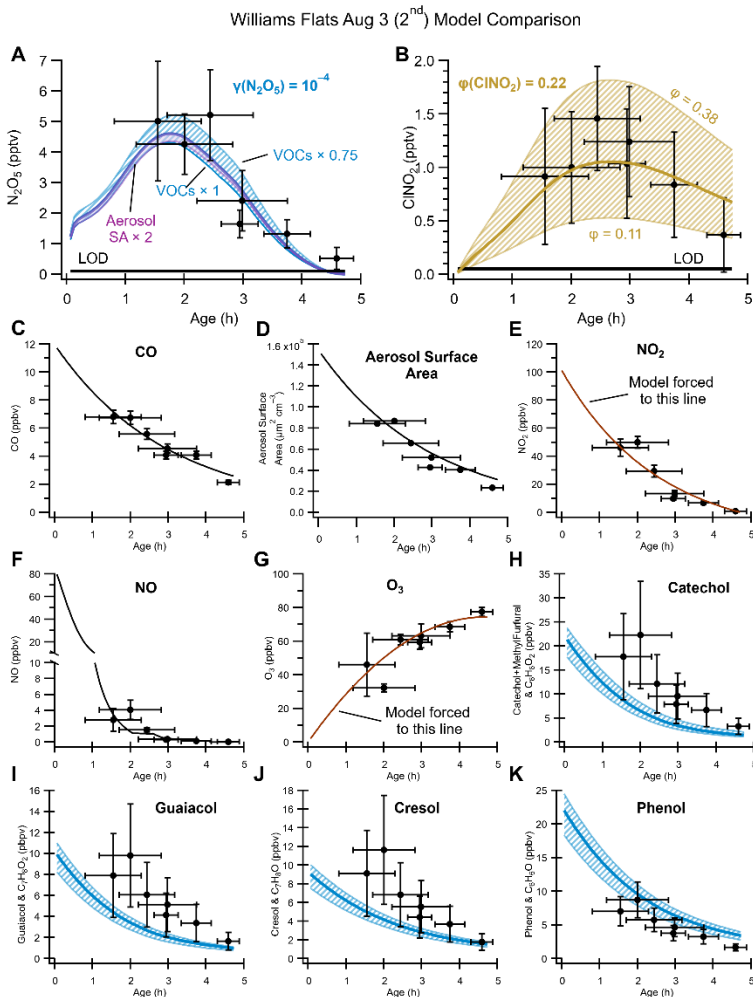


**Figure S8.** Comparison of box model results to observations for the Williams Flats fire on Aug 3 (2<sup>nd</sup> sampling). Observations are shown as black markers while model results are shown as solid lines. Vertical error bars include instrument uncertainty and 1- $\sigma$  variability (added in quadrature: the square root of the sum of squares ) of the average of the transect center observations (observations aligned with the top 5% of CO). The blue shading in H–K corresponds to model results shown in A. In this model, red lines indicate when a compound was forced to a guiding line as it was unable to be reproduced by the model for reasons discussed in Decker et al.(2)

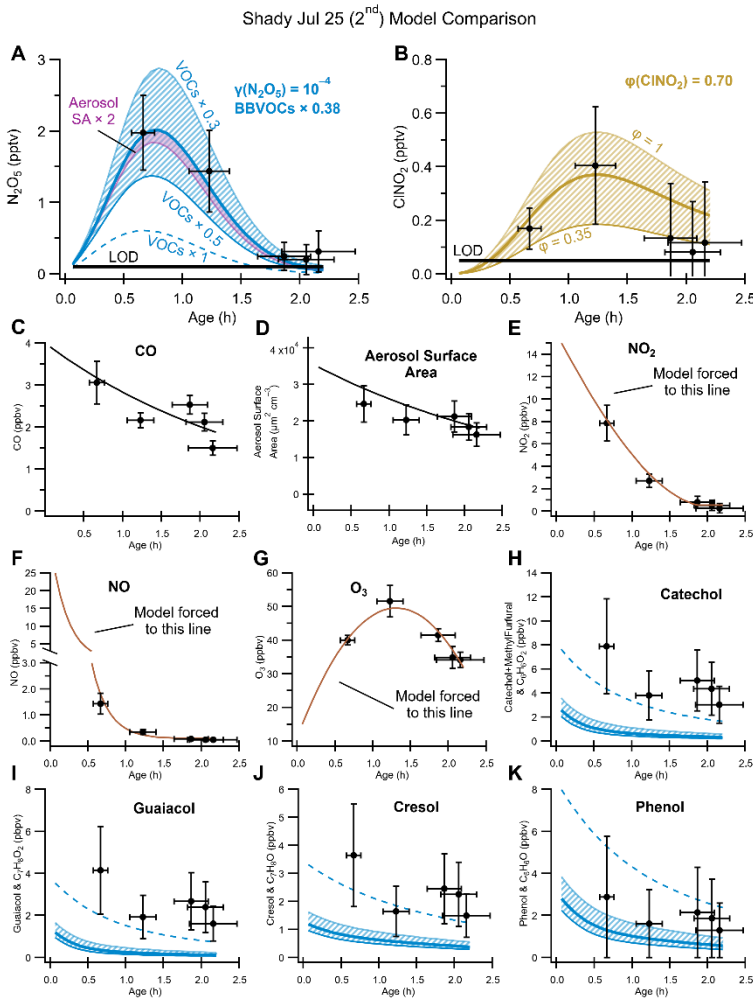


**Figure S9.** Comparison of box model results to observations for the Shady fire on July 25 (2<sup>nd</sup> sampling). Observations are shown as black markers while model results are shown as solid lines. Vertical error bars include instrument uncertainty and 1- $\sigma$  variability (added in quadrature: the square root of the sum of squares ) of the average of the transect center observations (observations aligned with the top 5% of CO). The blue shading in H–K corresponds to model results shown in A. In this model, red lines indicate when a compound was forced to a guiding line as it was unable to be reproduced by the model for reasons discussed in Decker et al.(2)

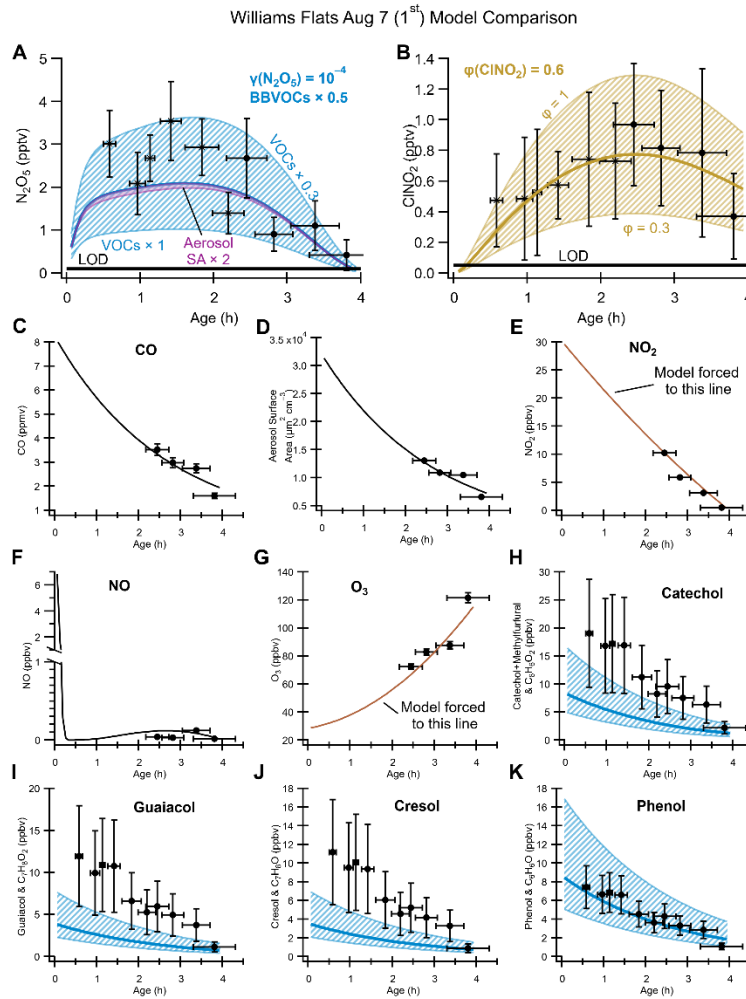


**Figure S10.** Comparison of box model results to observations for the Williams Flats fire on Aug 7 (1<sup>st</sup> sampling). Observations are shown as black markers while model results are shown as solid lines. Vertical error bars include instrument uncertainty and 1- $\sigma$  variability (added in quadrature: the square root of the sum of squares ) of the average of the transect center observations (observations aligned with the top 5% of CO). The blue shading in H–K corresponds to model results shown in A. In this model, red lines indicate when a compound was forced to a guiding line as it was unable to be reproduced by the model for reasons discussed in Decker et al.(2)

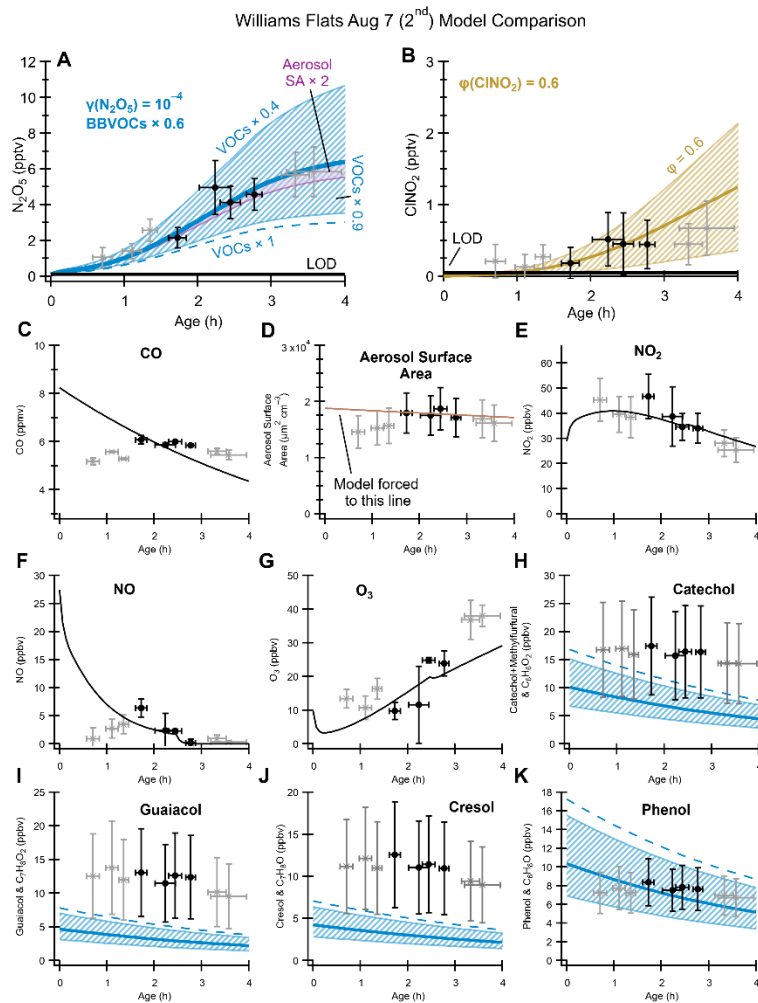


**Figure S11.** Comparison of box model results to observations for the Williams Flats fire on Aug 7 (2<sup>nd</sup> sampling). Observations are shown as markers while model results are shown as solid lines. Grey markers indicate observation excluded from the model for reasons discussed in Decker et al.(2) Vertical error bars include instrument uncertainty and 1- $\sigma$  variability (added in quadrature: the square root of the sum of squares ) of the average of the transect center observations (observations aligned with the top 5% of CO). The blue shading in H–K corresponds to model results corresponding shown in A. In this model, red lines indicate when a compound was forced to a guiding line as it was unable to be reproduced by the model for reasons discussed in Decker et al.(2)

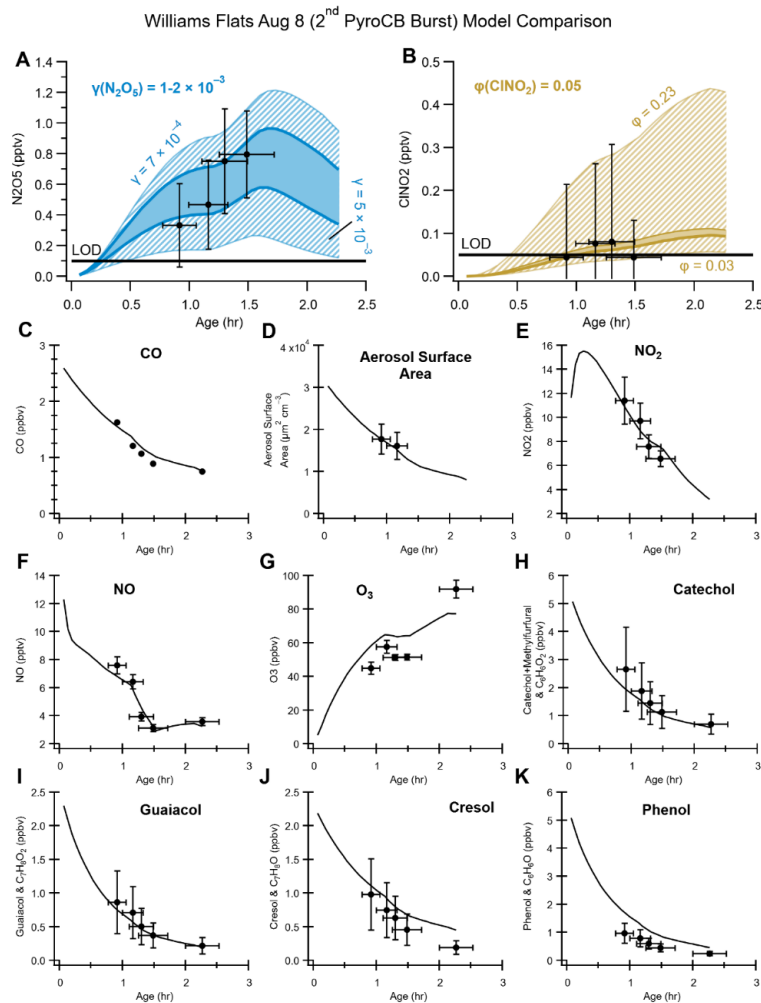


**Figure S12.** Comparison of box model results to observations for the Williams Flats fire on Aug 8 (2<sup>nd</sup> PyroCB burst). Error bars include instrument error with 1- $\sigma$  uncertainty from the average of the transect center in added in quadrature (the square root of the sum of squares) observations as well as plume age uncertainty.

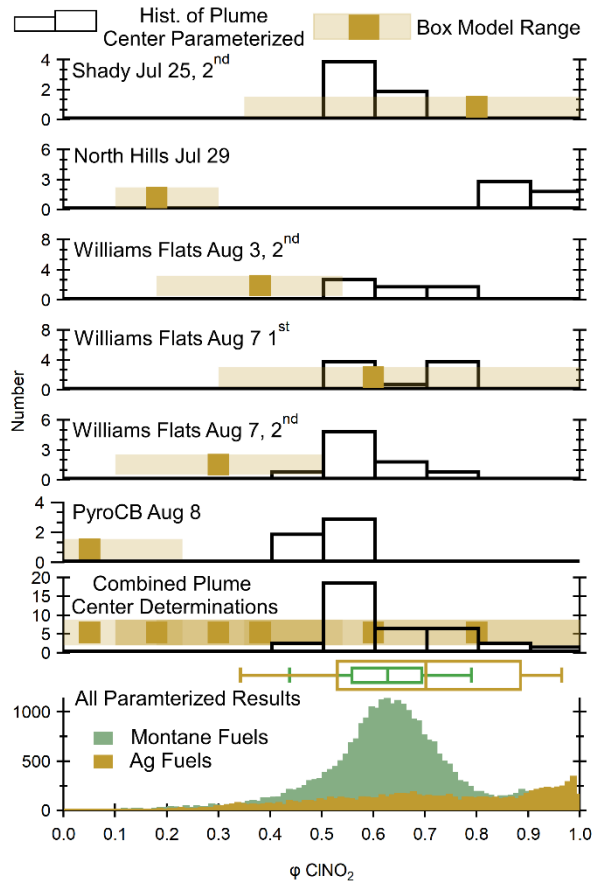


**Figure S13.** Comparison of the box model derived  $\phi(\text{ClNO}_2)$  for five montane plumes and the PyroCB event compared with parameterized  $\phi(\text{ClNO}_2)$ . Box model derived values are shown as the gold horizontal bars. Parameterized  $\phi(\text{ClNO}_2)$  is shown in the histograms (vertical bars) for the transect center observations used in the box model (hollow bars) and for all observations from FIREX-AQ (solid bars). Box and whiskers show results for the 10<sup>th</sup>, 25<sup>th</sup>, 50<sup>th</sup>, 75<sup>th</sup>, and 90<sup>th</sup> percentiles.

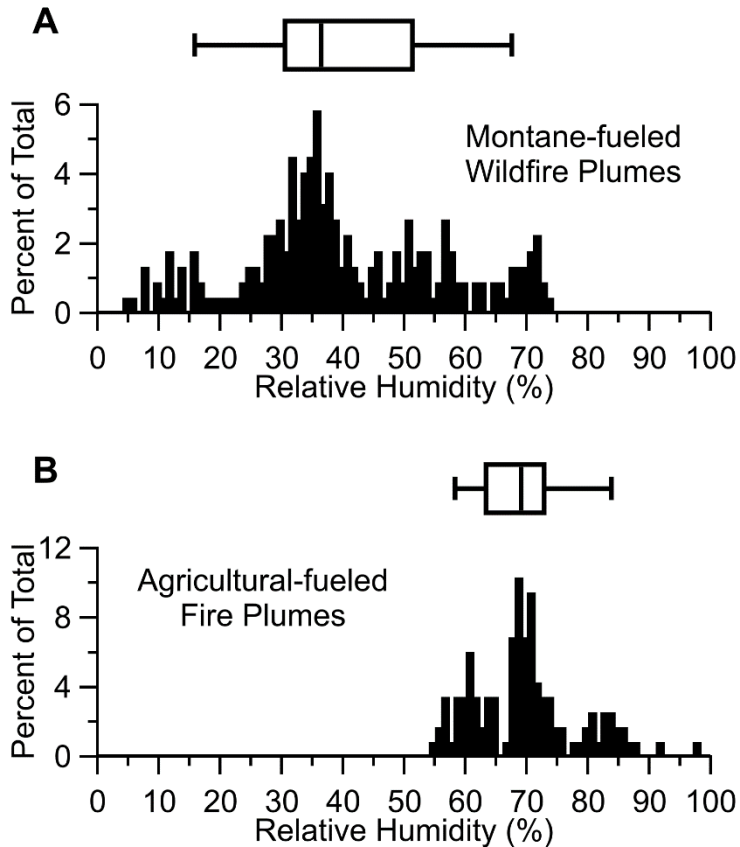


**Figure S14.** (A) and (B) show histograms of plume transect averaged relative humidity (RH). Each plume transect is averaged and combined as a histogram. For Montane-fueled wildfire plumes the average RH is 40% and the median is 36%. For agricultural-fueled plumes the average is 70% and the median is 69%. Box and whiskers show results for the 10<sup>th</sup>, 25<sup>th</sup>, 50<sup>th</sup>, 75<sup>th</sup>, and 90<sup>th</sup> percentiles.

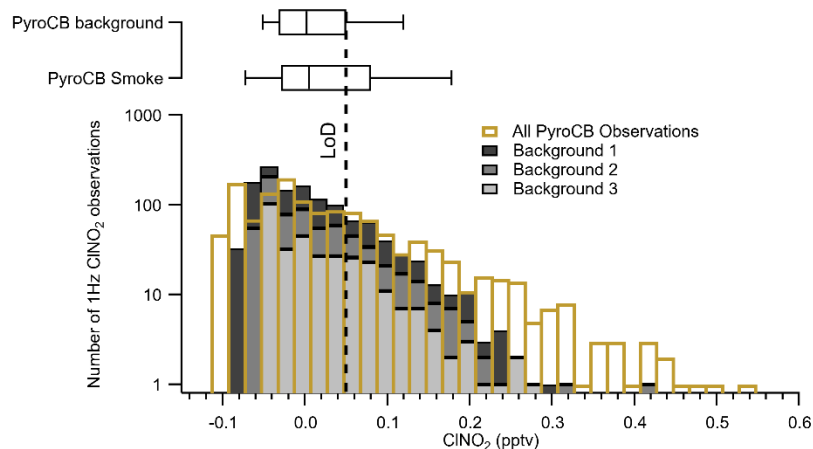


**Figure S15.** Histogram of  $\text{ClNO}_2$  observations from the NOAA I- CIMS on Aug 8 while sampling the PyroCB. The grey fill is stacked and indicates measurements taken from three background regions: one before the first measurement of PyroCB smoke, one after

the last measurement, and one in between two PyroCB transects. The transparent gold bars indicate measurements within the smoke. Box and whiskers show results for the 10<sup>th</sup>, 25<sup>th</sup>, 50<sup>th</sup>, 75<sup>th</sup>, and 90<sup>th</sup> percentiles. The median/average  $\pm \sigma$  for plume ClNO<sub>2</sub> mixing ratios is 0.01 / 0.03  $\pm$  0.10 pptv. The median/average  $\pm \sigma$  for background ClNO<sub>2</sub> mixing ratios is 0.00 / 0.02  $\pm$  0.06 pptv. The two averages are statistically different ( $p < 0.001$ ).

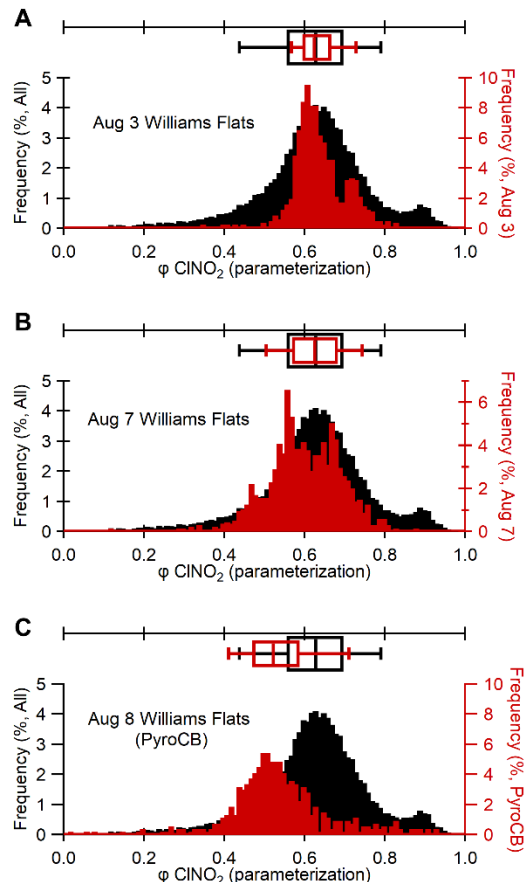


**Figure S16.** Comparison of parameterized  $\phi(\text{ClNO}_2)$  values for samplings of the Williams Flats fire smoke on three different days including the PyroCB on Aug 8. Results in black represent all observed wildfire smoke while observations in red show the Williams Flats fire sampled on Aug 3 (**A**) with a median of 0.62, on Aug 7 (**B**) with a median of 0.63, and on Aug 8 (PyroCB event, **C**) with a median of 0.52. Box and whiskers show results for the 10<sup>th</sup>, 25<sup>th</sup>, 50<sup>th</sup>, 75<sup>th</sup>, and 90<sup>th</sup> percentiles.

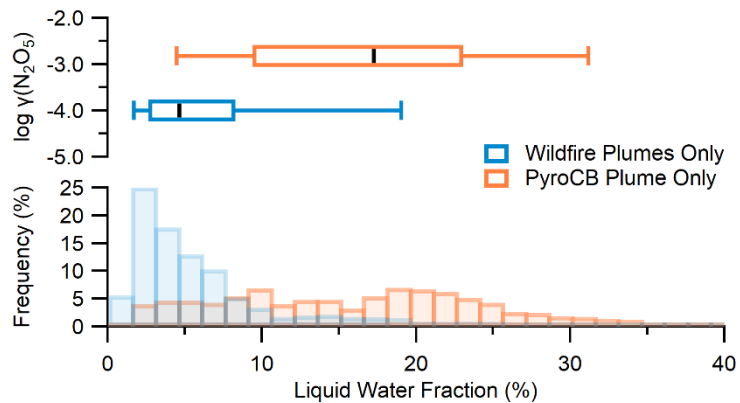


**Figure S17.** Comparison of liquid water fraction for all modeled wildfires except the PyroCB (blue) and only the PyroCB (orange). Liquid water fraction is defined as the liquid water content mass divided by the sum mass of the organic, ammonium, chloride, nitrate, sulfate, and liquid water). The box and whisker plots show the  $\gamma(N_2O_5)$  as a function of liquid water content with 10<sup>th</sup>, 25<sup>th</sup>, 50<sup>th</sup>, 75<sup>th</sup>, and 90<sup>th</sup> percentiles shown. The histograms show the frequency of observations as a function of liquid water fraction. The median liquid water fraction for the wildfire plumes was 5%. The median liquid water fraction for the PyroCB was 17%).

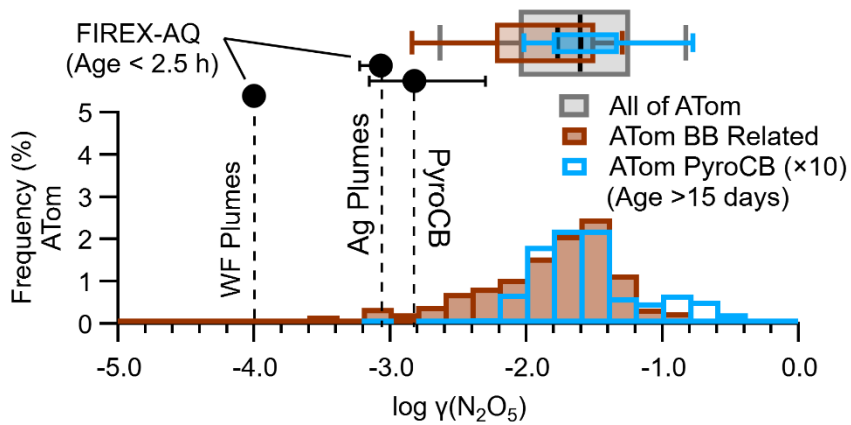


**Figure S18.** Comparison of the model-derived or fitted  $\gamma(N_2O_5)$  values from FIREX-AQ and ATom as shown in Figure 5A, but with the addition of a subset of data identified by Katich et al. (33) in ATom-3 to have PyroCB influence. Markers show FIREX-AQ results, and the histograms show ATom BB-related  $\gamma(N_2O_5)$  values. The box and whisker plots show the ATom BB-related (brown) (Methods), ATom-3 aerosol with PyroCB influence (33) (blue), and all of the ATom (grey) results from the UTLS.

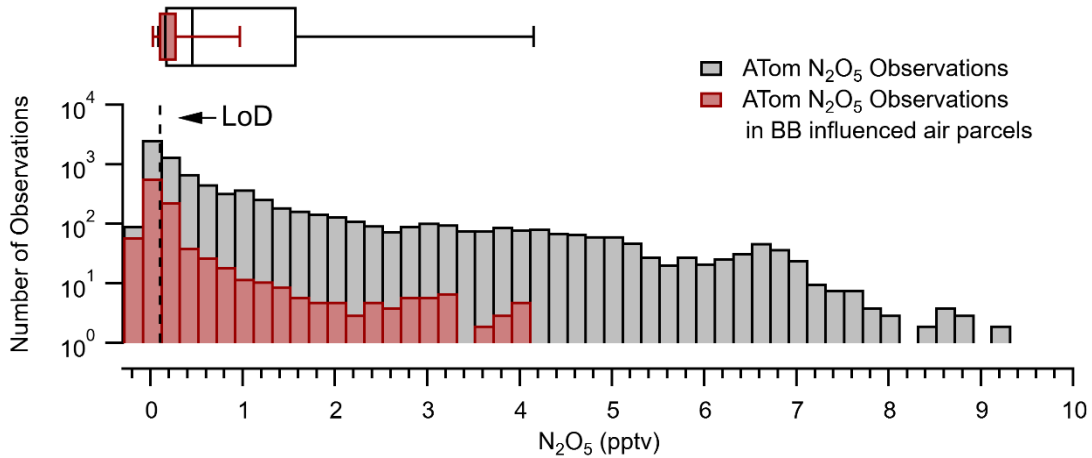


**Figure S19.** Observations of  $\text{N}_2\text{O}_5$  (pptv) from the NOAA I<sup>-</sup> CIMS aboard the NASA DC-8 during the ATom campaign. Grey bars indicate all observations while red bars indicate observations in BB influenced air. The median/average  $\pm \sigma$  for BB influenced  $\text{N}_2\text{O}_5$  mixing ratios during ATom is  $0.16 / 0.38 \pm 0.71$ . The median/average  $\pm \sigma$  for all  $\text{N}_2\text{O}_5$  mixing ratios during ATom is  $0.45 / 1.27 \pm 1.82$ .

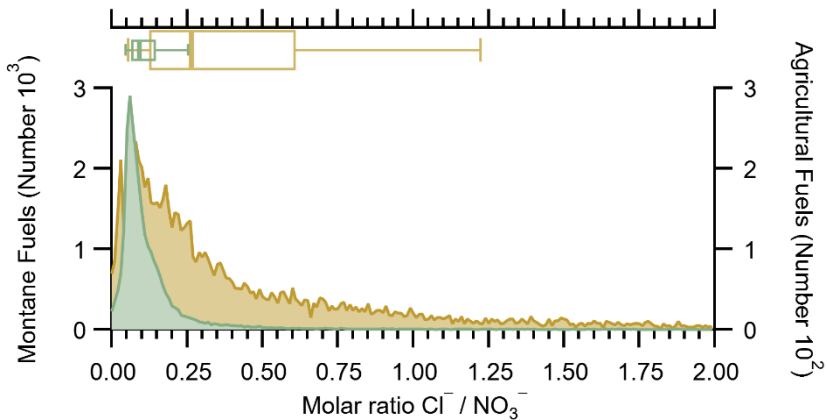


**Figure S20.** Histograms of the molar ratio of aerosol  $\text{Cl}^-$  to  $\text{NO}_3^-$  for montane fueled smoke (green) and agricultural-fueled smoke (brown). The montane-fueled smoke median/average  $\pm \sigma$  is  $0.1 / 0.1 \pm 0.2$  and the agricultural fueled smoke median/average  $\pm \sigma$  is  $0.3 / 0.4 \pm 0.4$ . Box plots show 10<sup>th</sup>, 25<sup>th</sup>, 50<sup>th</sup>, 75<sup>th</sup>, and 90<sup>th</sup> percentiles.

Measurements Used	Method	Platform	Campaign	Sample Frequency
CO	Picarro G2401-m, cavity ringdown spectrometer.	Twin Otter	FIREX-AQ	0.5 Hz
Non-refractory PM <sub>1</sub> chemical composition	ECCC aircraft High-resolution Aerosol Mass Spectrometer (HR-AMS)	Twin Otter	FIREX-AQ	1 Hz
CO	Tunable diode laser spectrometer	DC-8	FIREX-AQ	1 Hz
CO	Cavity enhanced spectrometer	DC-8	FIREX-AQ	1 Hz
NO <sub>2</sub> , NO <sub>y</sub> , and O <sub>3</sub>	NOAA chemiluminescence	DC-8	FIREX-AQ ATom	1 Hz
NO <sub>2</sub> , HONO	NOAA broadband Airborne Cavity Enhanced Spectrometer (ACES)	DC-8	FIREX-AQ	1 Hz
NO	NOAA laser induced fluorescence	DC-8	FIREX-AQ	1 Hz
C <sub>6</sub> H <sub>6</sub> O <sub>2</sub> , C <sub>6</sub> H <sub>6</sub> O, C <sub>7</sub> H <sub>8</sub> O, C <sub>7</sub> H <sub>8</sub> O <sub>2</sub> .	NOAA Proton Transfer Reaction Time of Flight Mass Spectrometer	DC-8	FIREX-AQ	1 Hz
C <sub>6</sub> H <sub>6</sub> O <sub>2</sub> , C <sub>6</sub> H <sub>6</sub> O, C <sub>7</sub> H <sub>8</sub> O, C <sub>7</sub> H <sub>8</sub> O <sub>2</sub> .	University of Innsbruck Proton Transfer Reaction Time of Flight Mass Spectrometer	DC-8	FIREX-AQ	1 Hz
HONO, N <sub>2</sub> O <sub>5</sub> , ClNO <sub>2</sub>	NOAA Iodide Time of Flight Chemical Ionization Mass Spectrometer (I <sup>-</sup> ToF CIMS)	DC-8	FIREX-AQ ATom (N <sub>2</sub> O <sub>5</sub> )	1 Hz
Aerosol Size Distribution and Derived Surface Area	Scanning mobility particle sizer (SMPS) Laser Aerosol Spectrometer (LAS)	DC-8	FIREX-AQ	60 sec 1 Hz
Non-refractory PM <sub>1</sub> chemical composition	CU aircraft High Resolution Aerosol Mass Spectrometer (HR-AMS)	DC-8	FIREX-AQ ATom	1 Hz
Photolysis rates	Charged-coupled device Actinic Flux Spectroradiometer (CAFS)	DC-8	FIREX-AQ ATom	1-5 Hz 1-3 Hz
bulk aerosol size distributions	Combination of techniques for dry diameters 2.7 nm – 4.8 μm	DC-8	ATom	1 Hz
Identification of cloud periods	Cloud, Aerosol, and Precipitation Spectrometer (CAPS)	DC-8	ATom	1 Hz
Identification of pyrogenic-influenced aerosol	Particle Analysis by Laser Mass Spectrometry (PALMS)	DC-8	ATom	1Hz

**Table S1.** Table of instrumentation used in this work.

	Transects used for the NEMR calculation	Transects rejected for the NEMR calculation
N <sub>2</sub> O <sub>5</sub> (Agricultural)	15	68
ClNO <sub>2</sub> (Agricultural)	90	29
N <sub>2</sub> O <sub>5</sub> (Montane)	95	104
ClNO <sub>2</sub> (Montane)	70	98

**Table S2.** A count of transects used or rejected for the calculation of N<sub>2</sub>O<sub>5</sub> or ClNO<sub>2</sub>. Roughly 37 % and 46 % of plume transects included N<sub>2</sub>O<sub>5</sub> and ClNO<sub>2</sub>, respectively, well in excess of the instrumental detection limits (LoD: N<sub>2</sub>O<sub>5</sub>=0.1 pptv and ClNO<sub>2</sub>=0.05 pptv at 1 Hz).

Fire name	State	Latitude	Longitude	Date sampled	Time sampled	Fuel
Shady Fire	Idaho	44.52	-115.02	July 24	17:45–18:15 MDT	Timber, Tall grass, and Logging debris
Sheep Fire	Idaho	43.56	-112.88	July 24	16:15–16:30 MDT	Sage-grass, Juniper, Grass, and Sagebrush
North Hills	Montana	46.75	-111.96	July 29	20:45–21:45 MDT	Managed Xeric, Understory, Sagebrush, Shrubland
Williams Flats	Washington	47.94	-118.62	Aug 03	17:30–19:30 PDT	Short grass, Ponderosa timber
				Aug 07	16:30–17:45 PDT & 18:00–19:30 PDT	
				Aug 08	17:45–19:15 PDT	

**Table S3.** List of wildfires referenced in the main text. A complete list of fires from FIREX-AQ is found in [Warneke *et al.*, 2023].

## References

- Ahern, A. T., L. Goldberger, L. Jahl, J. Thornton, and R. C. Sullivan (2018), Production of N<sub>2</sub>O<sub>5</sub> and ClNO<sub>2</sub> through Nocturnal Processing of Biomass-Burning Aerosol, *Environmental Science & Technology*, 52(2), 550-559, 10.1021/acs.est.7b04386.
- Akagi, S. K., R. J. Yokelson, C. Wiedinmyer, M. J. Alvarado, J. S. Reid, T. Karl, J. D. Crounse, and P. O. Wennberg (2011), Emission factors for open and domestic biomass burning for use in atmospheric models, *Atmos. Chem. Phys.*, 11(9), 4039-4072, 10.5194/acp-11-4039-2011.
- Bertram, T. H., J. A. Thornton, and T. P. Riedel (2009), An experimental technique for the direct measurement of N<sub>2</sub>O<sub>5</sub> reactivity on ambient particles, *Atmos. Meas. Tech.*, 2(2), 231-242.
- Bloss, C., V. Wagner, M. E. Jenkin, R. Volkamer, W. J. Bloss, J. D. Lee, D. E. Heard, K. Wirtz, M. Martin-Reviejo, G. Rea, J. C. Wenger, and M. J. Pilling (2005), Development of a detailed chemical mechanism (MCMv3.1) for the atmospheric oxidation of aromatic hydrocarbons, *Atmos. Chem. Phys.*, 5(3), 641-664, 10.5194/acp-5-641-2005.
- Brock, C. A., C. Williamson, A. Kupc, K. D. Froyd, F. Erdesz, N. Wagner, M. Richardson, J. P. Schwarz, R. S. Gao, J. M. Katich, P. Campuzano-Jost, B. A. Nault, J. C. Schroder, J. L. Jimenez, B. Weinzierl, M. Dollner, T. Bui, and D. M. Murphy (2019), Aerosol size distributions during the Atmospheric Tomography Mission (ATom): methods, uncertainties, and data products, *Atmos. Meas. Tech.*, 12(6), 3081-3099, 10.5194/amt-12-3081-2019.
- Decker, Z. C. J., M. A. Robinson, K. C. Barsanti, I. Bourgeois, M. M. Coggon, J. P. DiGangi, G. S. Diskin, F. M. Flocke, A. Franchin, C. D. Fredrickson, G. I. Gkatzelis, S. R. Hall, H. Halliday, C. D. Holmes, L. G. Huey, Y. R. Lee, J. Lindaas, A. M. Middlebrook, D. D. Montzka, R. Moore, J. A. Neuman, J. B. Nowak, B. B. Palm, J. Peischl, F. Piel, P. S. Rickly, A. W. Rollins, T. B. Ryerson, R. H. Schwantes, K. Sekimoto, L. Thornhill, J. A. Thornton, G. S. Tyndall, K. Ullmann, P. Van Rooy, P. R. Veres, C. Warneke, R. A. Washenfelder, A. J. Weinheimer, E. Wiggins, E. Winstead, A. Wisthaler, C. Womack, and S. S. Brown (2021), Nighttime and daytime dark oxidation chemistry in wildfire plumes: an observation and model analysis of FIREX-AQ aircraft data, *Atmos. Chem. Phys.*, 21(21), 16293-16317, 10.5194/acp-21-16293-2021.
- Fountoukis, C., and A. Nenes (2007), ISORROPIA II: a computationally efficient thermodynamic equilibrium model for K<sup>+</sup>-Ca<sup>2+</sup>-Mg<sup>2+</sup>-N H<sub>4</sub><sup>+</sup>-Na<sup>+</sup>-SO<sub>4</sub><sup>2-</sup>-Cl<sup>-</sup>-H<sub>2</sub>O aerosols, *Atmos. Chem. Phys.*, 7(17), 4639-4659, 10.5194/acp-7-4639-2007.
- Guo, H., L. Xu, A. Bougiatioti, K. M. Cerully, S. L. Capps, J. R. Hite Jr, A. G. Carlton, S. H. Lee, M. H. Bergin, N. L. Ng, A. Nenes, and R. J. Weber (2015), Fine-particle water and pH in the southeastern United States, *Atmos. Chem. Phys.*, 15(9), 5211-5228, 10.5194/acp-15-5211-2015.
- Guo, H., P. Campuzano-Jost, B. A. Nault, D. A. Day, J. C. Schroder, D. Kim, J. E. Dibb, M. Dollner, B. Weinzierl, and J. L. Jimenez (2021), The importance of size ranges

- in aerosol instrument intercomparisons: a case study for the Atmospheric Tomography Mission, *Atmos. Meas. Tech.*, 14(5), 3631-3655, 10.5194/amt-14-3631-2021.
- Koss, A. R., K. Sekimoto, J. B. Gilman, V. Selimovic, M. M. Coggon, K. J. Zarzana, B. Yuan, B. M. Lerner, S. S. Brown, J. L. Jimenez, J. Krechmer, J. M. Roberts, C. Warneke, R. J. Yokelson, and J. de Gouw (2018), Non-methane organic gas emissions from biomass burning: identification, quantification, and emission factors from PTR-ToF during the FIREX 2016 laboratory experiment, *Atmos. Chem. Phys.*, 18(5), 3299-3319, 10.5194/acp-18-3299-2018.
- Lao, M., L. R. Crilley, L. Salehpoor, T. C. Furlani, I. Bourgeois, J. A. Neuman, A. W. Rollins, P. R. Veres, R. A. Washenfelder, C. C. Womack, C. J. Young, and T. C. VandenBoer (2020), A portable, robust, stable, and tunable calibration source for gas-phase nitrous acid (HONO), *Atmos. Meas. Tech.*, 13(11), 5873-5890, 10.5194/amt-13-5873-2020.
- Lee, B. H., F. D. Lopez-Hilfiker, P. R. Veres, E. E. McDuffie, D. L. Fibiger, T. L. Sparks, C. J. Ebbin, J. R. Green, J. C. Schroder, P. Campuzano-Jost, S. Iyer, E. L. D'Ambro, S. Schobesberger, S. S. Brown, P. J. Wooldridge, R. C. Cohen, M. N. Fiddler, S. Bililign, J. L. Jimenez, T. Kurtén, A. J. Weinheimer, L. Jaegle, and J. A. Thornton (2018), Flight Deployment of a High-Resolution Time-of-Flight Chemical Ionization Mass Spectrometer: Observations of Reactive Halogen and Nitrogen Oxide Species, *Journal of Geophysical Research: Atmospheres*, 123(14), 7670-7686, <https://doi.org/10.1029/2017JD028082>.
- Liggio, J., S.-M. Li, K. Hayden, Y. M. Taha, C. Stroud, A. Darlington, B. D. Drollette, M. Gordon, P. Lee, P. Liu, A. Leithead, S. G. Moussa, D. Wang, J. O'Brien, R. L. Mittermeier, J. R. Brook, G. Lu, R. M. Staebler, Y. Han, T. W. Tokarek, H. D. Osthoff, P. A. Makar, J. Zhang, D. L. Plata, and D. R. Gentner (2016), Oil sands operations as a large source of secondary organic aerosols, *Nature, advance online publication*, 10.1038/nature17646  
<http://www.nature.com/nature/journal/vaop/ncurrent/abs/nature17646.html#supplementary-information>.
- Liu, X., Y. Zhang, L. G. Huey, R. J. Yokelson, Y. Wang, J. L. Jimenez, P. Campuzano-Jost, A. J. Beyersdorf, D. R. Blake, Y. Choi, J. M. St. Clair, J. D. Crounse, D. A. Day, G. S. Diskin, A. Fried, S. R. Hall, T. F. Hanisco, L. E. King, S. Meinardi, T. Mikoviny, B. B. Palm, J. Peischl, A. E. Perring, I. B. Pollack, T. B. Ryerson, G. Sachse, J. P. Schwarz, I. J. Simpson, D. J. Tanner, K. L. Thornhill, K. Ullmann, R. J. Weber, P. O. Wennberg, A. Wisthaler, G. M. Wolfe, and L. D. Ziembra (2016), Agricultural fires in the southeastern U.S. during SEAC4RS: Emissions of trace gases and particles and evolution of ozone, reactive nitrogen, and organic aerosol, *Journal of Geophysical Research: Atmospheres*, 121(12), 7383-7414, 10.1002/2016JD025040.
- May, A. A., G. R. McMeeking, T. Lee, J. W. Taylor, J. S. Craven, I. Burling, A. P. Sullivan, S. Akagi, J. L. Collett Jr, M. Flynn, H. Coe, S. P. Urbanski, J. H. Seinfeld, R. J. Yokelson, and S. M. Kreidenweis (2014), Aerosol emissions from prescribed fires in the United States: A synthesis of laboratory and aircraft measurements, *Journal of Geophysical Research: Atmospheres*, 119(20), 11,826-811,849, <https://doi.org/10.1002/2014JD021848>.

- McDuffie, E., E., L. Fibiger Dorothy, P. Dubé William, F. Lopez-Hilfiker, H. Lee Ben, A. Thornton Joel, V. Shah, L. Jaeglé, H. Guo, J. Weber Rodney, J. Michael Reeves, J. Weinheimer Andrew, C. Schroder Jason, P. Campuzano-Jost, L. Jimenez Jose, E. Dibb Jack, P. Veres, C. Ebben, L. Sparks Tamara, J. Wooldridge Paul, C. Cohen Ronald, S. Hornbrook Rebecca, C. Apel Eric, T. Campos, R. Hall Samuel, K. Ullmann, and S. S. Brown (2018a), Heterogeneous N<sub>2</sub>O<sub>5</sub> Uptake During Winter: Aircraft Measurements During the 2015 WINTER Campaign and Critical Evaluation of Current Parameterizations, *Journal of Geophysical Research: Atmospheres*, 123(8), 4345-4372, 10.1002/2018JD028336.
- McDuffie, E. E., D. L. Fibiger, W. P. Dubé, F. Lopez Hilfiker, B. H. Lee, L. Jaeglé, H. Guo, R. J. Weber, J. M. Reeves, A. J. Weinheimer, J. C. Schroder, P. Campuzano-Jost, J. L. Jimenez, J. E. Dibb, P. Veres, C. Ebben, T. L. Sparks, P. J. Wooldridge, R. C. Cohen, T. Campos, S. R. Hall, K. Ullmann, J. M. Roberts, J. A. Thornton, and S. S. Brown (2018b), ClNO<sub>2</sub> Yields From Aircraft Measurements During the 2015 WINTER Campaign and Critical Evaluation of the Current Parameterization, *Journal of Geophysical Research: Atmospheres*, 123(22), 12,994-913,015, 10.1029/2018JD029358.
- Müller, M., T. Mikoviny, S. Feil, S. Haidacher, G. Hanel, E. Hartungen, A. Jordan, L. Märk, P. Mutschlechner, R. Schottkowsky, P. Sulzer, J. H. Crawford, and A. Wisthaler (2014), A compact PTR-ToF-MS instrument for airborne measurements of volatile organic compounds at high spatiotemporal resolution, *Atmos. Meas. Tech.*, 7(11), 3763-3772, 10.5194/amt-7-3763-2014.
- Neuman, J. A., M. Trainer, S. S. Brown, K. E. Min, J. B. Nowak, D. D. Parrish, J. Peischl, I. B. Pollack, J. M. Roberts, T. B. Ryerson, and P. R. Veres (2016), HONO emission and production determined from airborne measurements over the Southeast U.S, *Journal of Geophysical Research: Atmospheres*, 121(15), 9237-9250, 10.1002/2016JD025197.
- Rickards, A. M. J., R. E. H. Miles, J. F. Davies, F. H. Marshall, and J. P. Reid (2013), Measurements of the Sensitivity of Aerosol Hygroscopicity and the  $\kappa$  Parameter to the O/C Ratio, *The Journal of Physical Chemistry A*, 117(51), 14120-14131, 10.1021/jp407991n.
- Roberts, J. M., H. D. Osthoff, S. S. Brown, and A. R. Ravishankara (2009), Laboratory studies of products of N<sub>2</sub>O<sub>5</sub> uptake on Cl<sup>-</sup> containing substrates, *Geophys. Res. Lett.*, 36, L20808, doi:10.1029/2009GL040448.
- Schill, G. P., K. D. Froyd, H. Bian, A. Kupc, C. Williamson, C. A. Brock, E. Ray, R. S. Hornbrook, A. J. Hills, E. C. Apel, M. Chin, P. R. Colarco, and D. M. Murphy (2020), Widespread biomass burning smoke throughout the remote troposphere, *Nature Geoscience*, 13(6), 422-427, 10.1038/s41561-020-0586-1.
- Solomon, S., K. Stone, P. Yu, D. M. Murphy, D. Kinnison, A. R. Ravishankara, and P. Wang (2023), Chlorine activation and enhanced ozone depletion induced by wildfire aerosol, *Nature*, 615(7951), 259-264, 10.1038/s41586-022-05683-0.
- Thaler, R. D., L. H. Mielke, and H. D. Osthoff (2011), Quantification of Nitryl Chloride at Part Per Trillion Mixing Ratios by Thermal Dissociation Cavity Ring-Down Spectroscopy, *Analytical Chemistry*, 83(7), 2761-2766, 10.1021/ac200055z.
- Thompson, C. R., S. C. Wofsy, M. J. Prather, P. A. Newman, T. F. Hanisco, T. B. Ryerson, D. W. Fahey, E. C. Apel, C. A. Brock, W. H. Brune, K. Froyd, J. M.

- Katich, J. M. Nicely, J. Peischl, E. Ray, P. R. Veres, S. Wang, H. M. Allen, E. Asher, H. Bian, D. Blake, I. Bourgeois, J. Budney, T. P. Bui, A. Butler, P. Campuzano-Jost, C. Chang, M. Chin, R. Commane, G. Correa, J. D. Crounse, B. Daube, J. E. Dibb, J. P. DiGangi, G. S. Diskin, M. Dollner, J. W. Elkins, A. M. Fiore, C. M. Flynn, H. Guo, S. R. Hall, R. A. Hannun, A. Hills, E. J. Hintsa, A. Hodzic, R. S. Hornbrook, L. G. Huey, J. L. Jimenez, R. F. Keeling, M. J. Kim, A. Kupc, F. Lacey, L. R. Lait, J.-F. Lamarque, J. Liu, K. McKain, S. Meinardi, D. O. Miller, S. A. Montzka, F. L. Moore, E. J. Morgan, D. M. Murphy, L. T. Murray, B. A. Nault, J. A. Neuman, L. Nguyen, Y. Gonzalez, A. Rollins, K. Rosenlof, M. Sargent, G. Schill, J. P. Schwarz, J. M. S. Clair, S. D. Steenrod, B. B. Stephens, S. E. Strahan, S. A. Strode, C. Sweeney, A. B. Thamess, K. Ullmann, N. Wagner, R. Weber, B. Weinzierl, P. O. Wennberg, C. J. Williamson, G. M. Wolfe, and L. Zeng (2022), The NASA Atmospheric Tomography (ATom) Mission: Imaging the Chemistry of the Global Atmosphere, *Bulletin of the American Meteorological Society*, 103(3), E761-E790, 10.1175/BAMS-D-20-0315.1.
- Veres, P. R., J. A. Neuman, T. H. Bertram, E. Assaf, G. M. Wolfe, C. J. Williamson, B. Weinzierl, S. Tilmes, C. R. Thompson, A. B. Thamess, J. C. Schroder, A. Saiz-Lopez, A. W. Rollins, J. M. Roberts, D. Price, J. Peischl, B. A. Nault, K. H. Møller, D. O. Miller, S. Meinardi, Q. Li, J.-F. Lamarque, A. Kupc, H. G. Kjaergaard, D. Kinnison, J. L. Jimenez, C. M. Jernigan, R. S. Hornbrook, A. Hills, M. Dollner, D. A. Day, C. A. Cuevas, P. Campuzano-Jost, J. Burkholder, T. P. Bui, W. H. Brune, S. S. Brown, C. A. Brock, I. Bourgeois, D. R. Blake, E. C. Apel, and T. B. Ryerson (2020), Global airborne sampling reveals a previously unobserved dimethyl sulfide oxidation mechanism in the marine atmosphere, *Proceedings of the National Academy of Sciences*, 117(9), 4505, 10.1073/pnas.1919344117.
- Wagner, N. L., W. P. Dubé, R. A. Washenfelder, C. J. Young, I. B. Pollack, T. B. Ryerson, and S. S. Brown (2011), Diode laser-based cavity ring-down instrument for NO<sub>3</sub>, N<sub>2</sub>O<sub>5</sub>, NO, NO<sub>2</sub> and O<sub>3</sub> from aircraft, *Atmos. Meas. Tech.*, 4, 1227-1240.
- Warneke, C., J. P. Schwarz, J. Dibb, O. Kalashnikova, G. Frost, J. Al-Saad, S. S. Brown, W. A. Brewer, A. Soja, F. C. Seidel, R. A. Washenfelder, E. B. Wiggins, R. H. Moore, B. E. Anderson, C. Jordan, T. I. Yacovitch, S. C. Herndon, S. Liu, T. Kuwayama, D. Jaffe, N. Johnston, V. Selimovic, R. Yokelson, D. M. Giles, B. N. Holben, P. Goloub, I. Popovici, M. Trainer, A. Kumar, R. B. Pierce, D. Fahey, J. Roberts, E. M. Gargulinski, D. A. Peterson, X. Ye, L. H. Thapa, P. E. Saide, C. H. Fite, C. D. Holmes, S. Wang, M. M. Coggon, Z. C. J. Decker, C. E. Stockwell, L. Xu, G. Gkatzelis, K. Aikin, B. Lefer, J. Kaspari, D. Griffin, L. Zeng, R. Weber, M. Hastings, J. Chai, G. M. Wolfe, T. F. Hanisco, J. Liao, P. Campuzano Jost, H. Guo, J. L. Jimenez, J. Crawford, and F.-A. Q. S. T. The (2023), Fire Influence on Regional to Global Environments and Air Quality (FIREX-AQ), *Journal of Geophysical Research: Atmospheres*, 128(2), e2022JD037758, <https://doi.org/10.1029/2022JD037758>.
- Wofsy, S. C., S. Afshar, H. M. Allen, E. C. Apel, E. C. Asher, B. Barletta, J. Bent, H. Bian, B. C. Biggs, D. R. Blake, N. Blake, I. Bourgeois, C. A. Brock, W. H. Brune, J. W. Budney, T. P. Bui, A. Butler, P. Campuzano-Jost, C. S. Chang, M. Chin, R. Commane, G. Correa, J. D. Crounse, P. D. Cullis, B. C. Daube, D. A. Day, J. M.

- Dean-Day, J. E. Dibb, J. P. DiGangi, G. S. Diskin, M. Dollner, J. W. Elkins, F. Erdesz, A. M. Fiore, C. M. Flynn, K. D. Froyd, D. W. Gesler, S. R. Hall, T. F. Hanisco, R. A. Hannun, A. J. Hills, E. J. Hintsa, A. Hoffman, R. S. Hornbrook, L. G. Huey, S. Hughes, J. L. Jimenez, B. J. Johnson, J. M. Katich, R. F. Keeling, M. J. Kim, A. Kupc, L. R. Lait, J.-F. Lamarque, J. Liu, K. McKain, R. J. McLaughlin, S. Meinardi, D. O. Miller, S. A. Montzka, F. L. Moore, E. J. Morgan, D. M. Murphy, L. T. Murray, B. A. Nault, J. A. Neuman, P. A. Newman, J. M. Nicely, X. Pan, W. Paplawsky, J. Peischl, M. J. Prather, D. J. Price, E. A. Ray, J. M. Reeves, M. Richardson, A. W. Rollins, K. H. Rosenlof, T. B. Ryerson, E. Scheuer, G. P. Schill, J. C. Schroder, J. P. Schwarz, J. M. St.Clair, S. D. Steenrod, B. B. Stephens, S. A. Strode, C. Sweeney, D. Tanner, A. P. Teng, A. B. Thames, C. R. Thompson, K. Ullmann, P. R. Veres, N. Vieznor, N. L. Wagner, A. Watt, R. Weber, B. Weinzierl, P. O. Wennberg, C. J. Williamson, J. C. Wilson, G. M. Wolfe, C. T. Woods, and L. H. Zeng (2018), ATom: Merged Atmospheric Chemistry, Trace Gases, and Aerosols, in *ORNL DAAC*, edited, Oak Ridge, Tennessee, USA.
- Wolfe, G. M., M. R. Marvin, S. J. Roberts, K. R. Travis, and J. Liao (2016), The Framework for 0-D Atmospheric Modeling (F0AM) v3.1, *Geosci. Model Dev.*, 9(9), 3309-3319, 10.5194/gmd-9-3309-2016.